VU Research Portal

Unravelling the chromosome

Meijering, Anna Elisabeth Christina

2021

document version
Publisher's PDF, also known as Version of record

citation for published version (APA)
Meijering, A. E. C. (2021). *Unravelling the chromosome: An optical tweezers approach to study the structure of human mitotic chromosomes*. Gildeprint.

Unravelling the chromosome

An optical tweezers approach to study
the structure of human mitotic chromosomes

This thesis was reviewed by:

prof.dr. Gijsje Koenderink   TU Delft
Delft, The Netherlands

prof.dr. Fred Mackintosh   Vrije Universiteit
Amsterdam, The Netherlands

prof. dr. John Marko   Northwestern University
Evanston, USA

prof.dr. Bela Mulder   AMOLF
Amsterdam, The Netherlands

prof.dr. Benjamin Rowland   Netherlands Cancer Institute
Amsterdam, The Netherlands

Cover by Maria Romanova
Printed by Gildeprint

The research presented in this thesis was conducted in the department of Physics and Astronomy and the LaserLaB at the Vrije Universiteit Amsterdam.

VRIJE UNIVERSITEIT

Unravelling the chromosome

An optical tweezers approach to study the structure of human mitotic chromosomes

ACADEMISCH PROEFSCHRIFT

ter verkrijging van de graad Doctor aan
de Vrije Universiteit Amsterdam,
op gezag van de rector magnificus
prof.dr. V. Subramaniam,
in het openbaar te verdedigen
ten overstaan van de promotiecommissie
van de Faculteit der Bètawetenschappen
op woensdag 28 april 2021 om 15.45 uur
in de aula van de universiteit,
De Boelelaan 1105

door

Anna Elisabeth Christina Meijering
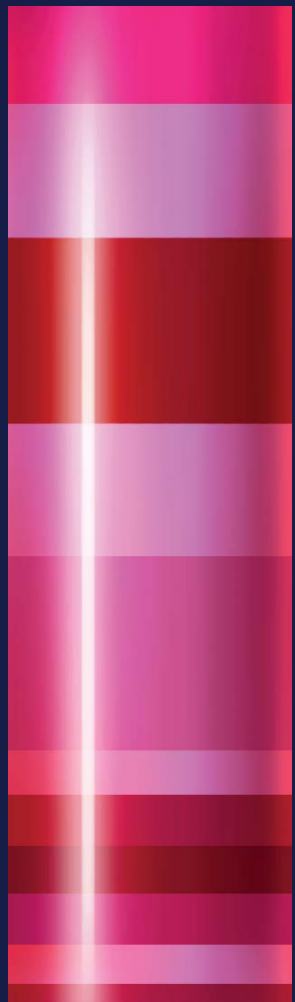
geboren te Amsterdam

promotoren: prof.dr.ir. G.J.L.Wuite
              prof.dr.ir. E.J.G. Peterman

Table of contents

General introduction

If you were asked to put a very thin thread, as long as the circumference of earth, inside a container the size of a basketball, and to do it in such a way that you can disentangle it when you take it out; how would you do that?

Anyone who once pulled their earphones out of their pocket, knows that this will be a daunting task. The thread will inevitably form knots and intertwines and it will take a tremendous effort to unravel these. Yet, this is the challenge that almost every cell in our body has to face on a regular basis. Human cells contain around one meter of DNA that is packaged inside the micrometer sized nucleus of the cell. Once in a while the cells that make up our body divide, thereby creating two new daughter cells that both contain a copy of the DNA from the mother cell. To this end, the DNA has to be duplicated and subsequently segregated without entanglements of the DNA molecules. If this process fails, chances are that the cell dies. Intuitively, one would expect that the DNA has to be compacted in a highly controlled fashion in order to overcome these challenges. It is, however, still largely unknown whether or not such a highly ordered architecture is indeed produced by cells and, if so, how this architecture would be achieved.

The research described in this thesis was motivated to gain a better understanding of the architecture that governs DNA integrity during cell division. To understand the relevance of this research, this chapter will introduce the underlying biological concepts for the broader audience and contain a brief explanation of the choice of our experimental approach.

1.1   Introducing chromosomes

1.1.1   "Omnis cellula e cellula"

In 1665 Robert Hooke published the work Micrographia, where he collected a series of hand-drawn illustrations of observations he made with his microscope[1]. Here, for the first time, a description was given of plant tissue containing regular cavities that he gave the name cells after their resemblance of the cells from a honeycomb (Figure 1.1a). We now know that cells form the building blocks of live and that they exist in a wide variety of shapes and sizes. Generally, eukaryotic cells, like the ones in our body, consist of several

components including a cell membrane that provides the boundary between the cell and its environment, the cytoplasm containing several cellular organelles and a nucleus that contains the DNA. Every cell is derived from a previously existing cell through the process of cell division ("Omnis cellula e cellula" – Robert Virchow [2]). In order to stay alive, grow and reproduce, the cell has to do a lot of work, which is primarily carried out by the work horses of the cell: proteins. The presence or absence of specific proteins in a cell determines how the cell will develop and, on a larger scale, what the organism will look like. Which proteins a cell should produce is encoded in the DNA.
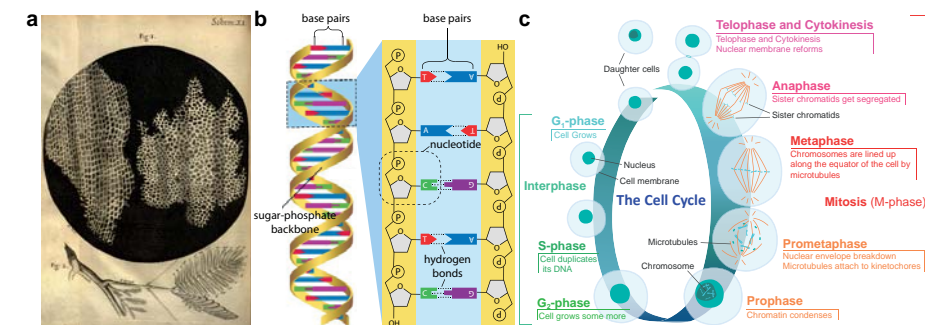
Figure 1.1: a) Drawing of the cork tissue that Robert Hooke observed with his microscope and called "cells" after their resemblence with the cells of a honeycomb. Figure from ref. [1]. b) Schematic representation of the structure of dsDNA with an inset showing base pairing interactions between the four nucleotides that make up the DNA. Figure adapted from ref. [6]. c) Schematic overview of the eukaryotic cell cycle with an emphasis on mitosis and the processes that regard mitotic chromosome formation and segregation. Figure adapted from ref. [7].

1.1.2   The double helix

Although the foundation of cell biology was established with Schwann's tenets of cell theory in the mid-nineteenth century [3], for a considerably long time it remained a mystery how information was passed on from one cell (or organism) to another. The existence of an information carrier was commonly accepted, and backed up by the observation from, among others, Gregor Mendel that parental traits are inherited in a discrete manner – in contrast to the idea of inheriting a smooth blend from both parents. But it took until

1953 before the structure of DNA (deoxyribonucleic acid) was discovered by James Watson and Francis Crick upon laying eyes on X-ray diffraction images from Rosalind Franklin[4].

The molecular structure of DNA intrinsically answers the question how a cell can divide into two daughter cells without loss of information. Double-stranded (ds)DNA consists of two long chains of repeating subunits called nucleotides which are wound around one another in a helical conformation (Fig. 1c). Adenine (A), Thymine (T), Guanine (G) and Cytosine (C) are the four types of nucleotide variants that when laced up together with their sugar-phosphate backbone, form a series of letters that contains the genetic information of the DNA. The nucleotides from one DNA strand prefer to bind pairwise via hydrogen bonding to nucleotides on the other strand (A to T and G to C) thereby forming so-called base pairs (bp)[5]. Once the sequence of nucleotides in one chain is known, the complementary strand can readily be deciphered (Figure 1.1c). This principle reveals the possibility to copy genetic information and pass it on onto the daughter cells: by opening up the double helix each of the two chains can act as a template to create two new complementary chains.

But when we talk about DNA as information carrier, what exactly do we mean? The human genome consists of around 3 billion base pairs. In comparison, the bible contains around 3 million letters, a thousand times less than the DNA in every cell in our body. The sequence of letters in the DNA can be thought of as a very large collection of recipes that describe specific proteins. In analogy to the letters of a book, words in the DNA are formed by groups of three nucleotides. These groups of three nucleotides, each encode for one so called amino acid. In total, there are twenty different amino acids to be found in the human body. When laced up together, the amino acids form complex three-dimensional structures that we call proteins. In this way, the order of amino acids determines the shape and function of the protein. Thus, changes in the nucleotide sequence of the DNA can lead to a change in the proteins that a cell produces and, on a larger scale, to the properties of that specific organism.

1.1.3 Mitosis

One of the most fascinating things that I have personally witnessed was looking through a microscope to the process of mitosis (or cell division),

where a cell splits in half, thereby giving rise to two new daughter cells. While the cell appears to be in a relatively quiet and peaceful state when it is in interphase, as soon as it starts to round up for mitosis dramatic changes in the cell's morphology can be observed. In the time frame of around two hours, the cell transitions through a series of complex phases with the ultimate goal of entirely constricting the cell into two parts that both contain a complete and intact copy of the DNA (Figure 1.1b).

The total amount of DNA in a human cell is divided into 46 smaller pieces, which we call chromosomes. Prior to mitosis, the DNA of each chromosome gets almost entirely replicated, except for a small piece where the two copies remain attached. This region is called the centromeric region and can be recognized by a set of very specific proteins that only reside there. While the chromosomes are in a spaghetti-like conformation during most of the cell cycle, at the onset of mitosis the chromosomes start to get compacted and with light microscopy it can be observed that they become further and further individualized (prophase) (Figure 1.1b). During the next step of mitosis, the nuclear envelope gets removed (nuclear envelope breakdown, NEB) and thread-like structures called microtubules attach to the kinetochores that lie next to the centromeric regions of the chromosomes and start to pull on them (prometaphase). Due to the opposing forces that the microtubules exert on the chromosomes, the chromosomes align in the equator of the cell (metaphase). The proper attachment and subsequent alignment of the chromosomes forms an essential checkpoint, also known as the spindle attachment checkpoint (SAC), that signals to the cell that it can start to release the two copies of the chromosomes from one another by cleavage of the proteins that are holding them together. During anaphase the two daughter chromosomes are pulled by the microtubules to the two opposite ends of the cell. Finally, during telophase two new nuclear envelopes start to form around the separated daughter chromosomes. At the same time the cell is ready to divide into two new daughter cells by the process of cytokinesis.
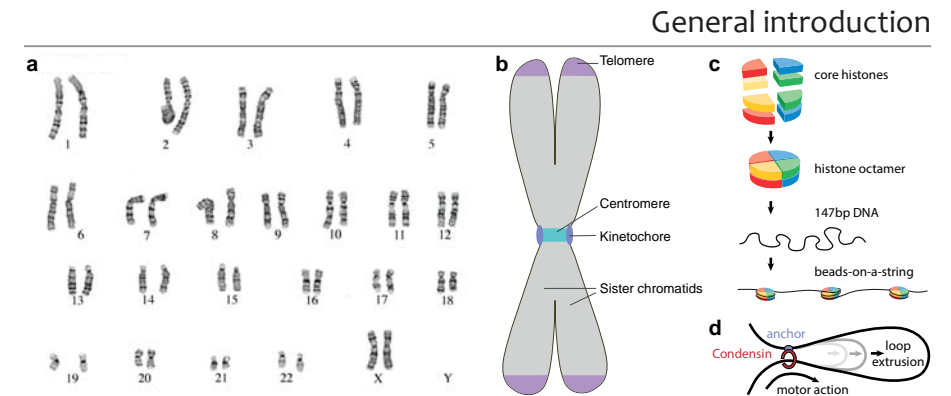
1.2 Chromosomes

As mentioned before, the human genome consists of 46 chromosomes; one half of them we receive from our mother and the other half from our father. This results in two sets of 22 similar chromosomes and two sex chromo-

somes that determine someone's biological gender (XX for a female and XY for a male)[8] (Figure 1.2a). When depicted in a karyotype as in Fig. 2a, chromosomes are always shown in their condensed mitotic shape. The longest chromosome contains around 250 Mbp, around a factor five more than the shortest chromosome (50 Mbp). The dark and light banding pattern is chromosome specific and arise from staining with a dye[9]. Moreover, the chromosomes show a characteristic X-shape, that arises from the two copies of the DNA that are still attached to one another in the centromeric region and is shown schematically in Figure 1.2b. The centromere can be recognized both by the DNA that contains a repetitive sequence unique to this region and by specific proteins (e.g. the nucleosomes CENP-A and CENP-B) that are only present in this region (see also subheading 1.2.1 Nucleosomes)[10]. On both sides of the centromere, the kinetochore is found, which is the region where microtubules attach during mitosis to segregate the two DNA copies (sister chromatids). At the end of the four arms of the chromosome the telomeres are located. The function of the telomeres is to protect the ends of the DNA molecules from damage and, just like the centromere, it can be recognized by specific DNA sequences and a unique set of proteins that only binds to this region of the DNA[11].

One can hardly imagine how the cell is able to organize the DNA in such a predictable shape as that of the mitotic chromosome and how it can resolve the vast amount of entanglements resulting from replication without knowledge of macro-dimensions. Although there are many open questions, we do know that several proteins play a key role in this process of compaction and organization.

1.2.1 Nucleosomes

The first step in compaction of DNA is performed by nucleosomes. There is a large variety of these cylindrically shaped protein complexes found in the cell, but the most common once consists of an octamer of the core histones (H2A, H2B, H3 and H4), that wrap a piece of 147 bp DNA around it with about two turn[12] (Figure 1.2c). The nucleosome-free pieces of DNA, the linker DNA, of 10-80 bp connect neighboring nucleosomes. This relatively loose structure is called beads-on-a-string configuration and reduces the end-to-end length of the DNA around six fold[13]. Moreover, nucleosomes have a tendency to

Figure 1.2: a) Karyotype of the human genome (female) showing the characteristic banding patterns that are used to classify the chromosomes. Figure from ref. 19. b) The mitotic chromosome has a typical X-shape that arises from the two DNA copies that form two sister chromatids and that are still connected to each other in the centromeric region. c) Nucleosomes consist of an octamer of histones together forming a cylindrical structure around which DNA wraps in almost two turns. Under specific experimental conditions it is observed that nucleosomes can interact with each other forming more complex and compact structures such as the 30-nm fiber. d) The ring-shaped protein complex Condensin binds to DNA and uses its motor activity to extrude loops of increasing size. Figure adapted from ref. 20.

stack onto one another, which under some specific experimental circumstances can result in the formation of compact fibers, like the famous but highly debated 30 nm fiber that results in a compaction of the DNA up to 50-fold[12]. The existence of such fibers in mitotic chromosomes could however never be confirmed[14,15]. On the other hand, it has been shown that post-translational modifications of histone tails can contribute to the compaction of mitotic chromosomes[16–18]. Although nucleosomes are extremely abundant on the DNA – a human cells contains around 30 million copies[8] – and can compact DNA to a first degree, they do not provide enough compaction nor organization to explain how the chromosome obtains its mitotic X-shape (see Models for chromosome compaction).

1.2.2 Condensin I and II

The Condensins belong to another family of multi-subunit protein complexes that have been shown to fulfil critical functions for mitotic chromosome structure. Two different types of condensins, Condensin I and Condensin II, are found in the human body. Rapid depletion of either of them has been

shown to result in serious defects in mitotic chromosome individualization and architecture [21]. It has been proposed that their ring-shaped structure in combination with motor activity is used to bind to DNA and subsequently extrude a loop through the ring. Recently in vitro experiments captured this loop-extrusion activity on bare DNA (Figure 1.2d) [20]. At the same time, polymer simulations predict that loop-extruders could explain the individualization and formation of a rod-shaped chromosome [22]. In this simulation the loop-extruding complexes end up along a central axis of the rod-shaped polymer structure. This is in good agreement with the observation from fluorescence and electron microscopy studies that Condensins are primarily located on a narrow central axis along the chromatids [15,23] and even forming a helical pattern [24,25]. Together these observations have led to the picture of condensins forming a central scaffold along the chromosome arms with protruding loops of DNA that extend outward of the central scaffold.

1.2.3 Topoisomerase IIα

Replication, compaction and segregation of the DNA inevitably leads to DNA entanglements. These entanglements can hinder further compaction of the chromosome and even become detrimental to the DNA's integrity when they are not resolved before or quickly after chromatid segregation. Topoisomerase IIα (TOP2A) is a specialized protein that has the ability to bind two DNA strands and pass them along each other by breaking and annealing the backbone of one of the DNA molecules [26]. This intricate process of resolving DNA entanglements has been shown to be crucial for mitotic chromosome condensation [27,28] and its presence is required for the in vitro assembly of chromosomes [29]. Just like Condensins, TOP2A is present along the central axis of the chromatids [15,23–25] and is the most abundant protein in the mitotic chromosomes by mass [30,31].

However, it is not clear what structural role TOP2A fulfils once the mitotic chromosome structure has been established. There has been some debate about the necessity of TOP2A for the maintenance of the chromosomal structure. In a recent study, rapid depletion of TOP2A transformed compacted chromosomes to elongated and thinned shapes [32]. However, when the protein was inhibited using anti-cancer agents, thereby locking the TOP2A in its closed DNA bound form, the chromosome did not show such a

transformation, suggesting that TOP2A fulfils a structural role for the mitotic chromosome by binding to DNA in a clamped conformation.

1.2.4 Models for chromosome structure

A variety of models that describe chromosome structure can be found in literature, which underlines the importance to find other means to investigate their architecture. The classical textbook image of a chromosome depicts the hierarchal fold, where sequential winding of nucleosome fibers into increasingly large chromatin fibers finally results in the mitotic X-shape (Figure 1.3a) [8]. This model has known much popularity, especially after the in vitro assembly of the 30-nm fiber [33]. However, evidence of such large-scale
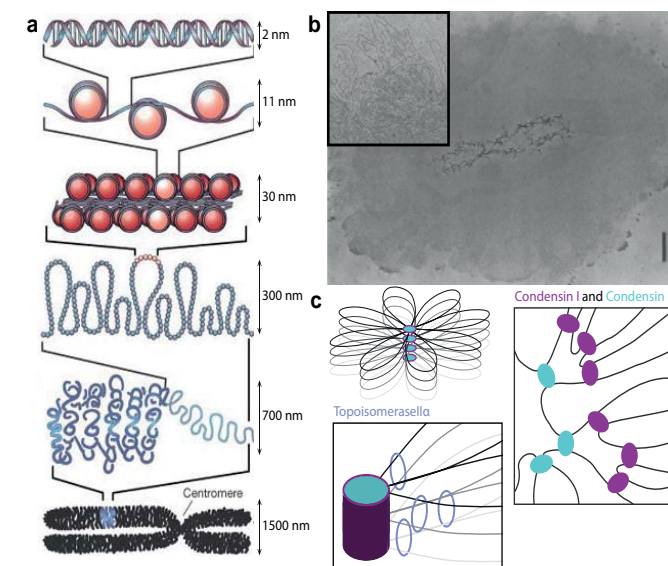
Figure 1.3: Models for chromosome compaction. a) Classical text book image of chromosome compaction showing how chromatin gets compacted by sequential winding into increasingly large fibers and coils. Figure adapted from ref. 12. b) Electron-microscope image of a histone-depleted chromosomes shows a central X-shaped scaffold with a halo of loops. Inset shows a zoom of those loops. Figure adapted from ref. 36. c) In the radial loop model, a central scaffold of big loops (400-450 kbp) are formed by Condensin II complexes and smaller nested loops (70-80 kbp) by Condensin I. TOP2A might fulfil a structural role to cross link consecutive layers of loops that are formed by Condensin proteins, thereby maintaining longitudinal chromosome compaction. Figure adapted from refs. 32&34.

folded structures like the 30-nm fiber in vivo are lacking [14,15] and the model poses questions regarding how fibers folding onto themselves can lead to the robust cylindrically shaped chromosome.

More recently, the chromatin loop model has gained much popularity, especially by compelling evidence from new computational, fluorescence, single-molecule and genome interaction studies [20,22,23,34,35]. This model depicts the chromosome as consisting of a central proteinaceous scaffold with chromatin loops emanating from the center. It was first proposed in 1977 by the observation that after histone depletion, chromosomes maintain a relatively densely packed X-shaped scaffold surrounded by a halo of DNA loops (Figure 1.3b) [36]. The discovery of loop extruding motors from the SMC family (Condensin I and II in humans) and the helical regularity in the mitotic chromosome as was inferred from data using a crosslinking technique called Hi-C, has resulted in a consistent model [34,37]. In this model Condensin II proteins extrude big loops of chromatin (400-450 kbp) thereby forming a central scaffold, after which Condensin I proteins reduce the size of these loops by formation of nested loops (70-80 kbp)(Figure 1.3c). It has been proposed that neighboring layers of nested loops are connected to other proteins such as TOP2A to provide further compaction along the length of the chromosome [32](Figure 1.3c).

However, fluorescence microscopy studies indicate that the central scaffold is a rather discontinuous arrangement of protein complexes with an alternating pattern [24] and possibly forming a double axis [25]. This observation is backed up by micropipette aspiration studies, where Condensin I and II staining shows an irregular pattern without evident helicity [38]. These, and other observations, have resulted in alternative models like the chromatin network and thin sheet model, that are not necessarily contradictive to the central scaffold model, but rather provide alternatives for the carrier of the mechanical load in the chromosome structure. In order to obtain a complete picture of the chromosome structure, several outstanding questions need to be answered: What are the molecular details of the central scaffold? Is the structure of the scaffold homogeneous along its length? And if not, which other structural elements provide the mechanical elasticity that is observed for mitotic chromosomes? Does TOP2A also provide a structural role for the scaffold or is it only essential for the formation of the cylindrical chromosome structure?

1.3 Chromosome mechanics

1.3.1 Why studying chromosome mechanics?

The motivation to study chromosome mechanics is three-fold. First of all, studying the global mechanical response of chromosomes to forces can help to unveil the internal architecture of the chromosomes. Combining mechanical experiments with theoretical models has proven to be a powerful tool to gain insights into the molecular details of the object of interest. For example, with such an approach a molecular model of DNA stretching has been developed [39] and the dynamic cross linking of actin networks was determined [40]. Comparison of the chromosome's elastic response upon external forces with predictions from theoretical models can give insights into the hierarchical architecture of the chromosome.

Moreover, mechanical experiments on mitotic chromosomes isolated from human cells allow for the investigation of the role of specific proteins in governing chromosomal architecture. By interference with drugs or compounds that act on specific proteins or by depletion of these proteins the effect on chromosome mechanics can be probed directly. Thus, the second motivation for this thesis is to gain a better understanding not only of the global chromosomal architecture, but also of the role of specific proteins in the formation and maintenance of this architecture.

Finally, cell division is an intrinsically mechanical process. Chromosomes are dramatically compacted and exposed to forces from microtubules that pull on them. As a consequence, the chromosomes bend and extend during anaphase of mitosis. Estimates for the forces involved are much larger (hundreds of piconewton [41]) than the force that single molecules can exert (piconewton range [42]). But it is currently unclear how such high forces are being produced. Estimates of the forces that are involved and knowing the mechanical response of the chromosomes to them, can help understand the process of cell division.
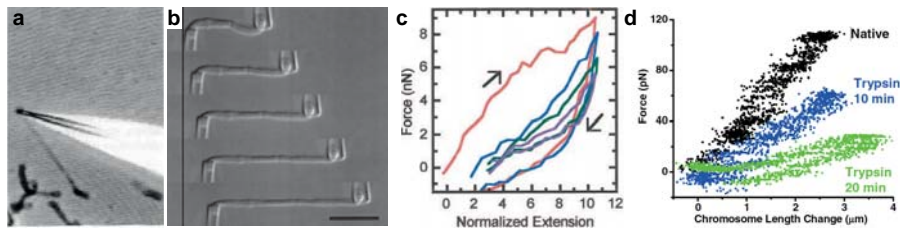
Figure 1.4: a) Chromosomes adhered to a glass surface could be extended using a micropipette. Figure from ref. 43. b) Newt chromosomes were aspirated in-between two micropipettes and could be stretched several times their native length. Figure adapted from ref. 46 . c) Force-extension curves of newt chromosomes show that irreversible stretching is induced when forces above around 1 nN are applied. Figure adapted from ref. 45. d) After prolonged exposure to trypsin human chromosomes strongly soften, but do not disintegrate. Figure adapted from ref. 47.

1.3.2   Previous studies on chromosome mechanics

In pioneering work of Claussen et al. chromosomes that were partially adhered to a glass surface showed a remarkable extensibility (Figure 1.4a) [43]. In a follow-up paper they found that the bands of the G-banding pattern, actually consisted of several bands when the chromosome got stretched [44]. In the same year, Houchmandzadeh et al. developed an assay where newt chromosomes were aspirated to calibrated micro pipettes by application of a small under pressure [45]. With the same approach, it was shown that chromosomes exhibit a reversible elasticity up to forces as high as a nanonewton, after which they get irreversibly deformed (Figure 1.4bc) [46]. Moreover, using a strategy to damage either DNA or proteins (using restriction enzymes or trypsin)(Figure 1.4d), Sun et al. found that human chromosome elasticity is best described by a polymer network where the proteins act as cross linkers [47].

These examples show that the investigation of chromosome mechanics can yield unexpected and valuable insights into the structure of the chromosome that would not have been accessible with more passive approaches. These studies however, all rely on the same technique and up till now there has not been an independent way to validate or challenge these findings. Moreover, some improvements on this technique can be envisioned in terms of control over the sample, force resolution and attachment strategy. These

realizations have motivated us to develop a new methodology in order to study chromosome mechanics.

1.4   Using light to probe the nanoscale

Studying chromosome mechanics is challenging since it puts stringent requirements on the technique of choice. Most importantly, it requires the possibility to manipulate a chromosome isolated from a cell, while recording the force response with high accuracy. Ideally, a technique is used that allows for changing the environment of the chromosome in order to investigate its response to external stimuli. And finally, it would be extremely beneficial to use a technique that is compatible with imaging techniques like fluorescence microscopy. Optical tweezers are ideally suited to fulfill these requirements.

1.4.1   Optical tweezers

The invention of the optical trap in the 1980's by Arthur Ashkin [48,49] and the subsequent increase of variations and improvements on the basic concept of optical tweezers has evolved into one of the most powerful tools in the field of biophysics and was in 2018 awarded with the Nobel prize. This technique relies on the property of light to carry momentum. On a macroscopic scale we hardly ever see the effect of the forces that are applied by light particles, but on the microscopic scale these forces are in the same order as the forces that play a role within cells. To exploit this property of light to investigate biomolecular systems, the coherent light from a laser source is used to create a very tight focus of the Gaussian laser beam. A microscopic particle, for example a polystyrene bead with a diameter of a few micrometers, will refract the laser light due to the higher refractive index than the medium that is surrounding it [49]. This refraction will induce a net momentum change of the laser light that has to be counteracted by a momentum change of the particle itself according to Newton's third law of motion (Figure 1.5ab). As a result, upon a deviation of the microsphere from the center of the laser focus and the consequent deflection of the laser beam, the microsphere will feel a restoring force towards the center of the laser focus. As such, the
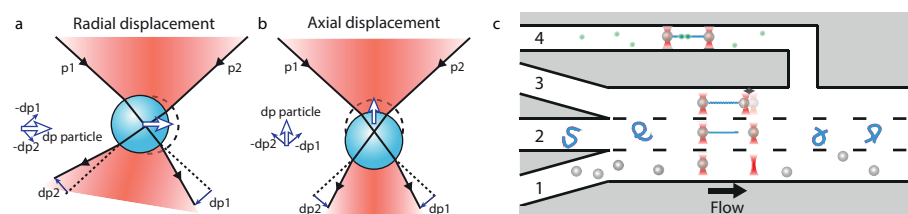
Figure 1.5: An optical potential well is created by a tightly focused Gaussian beam. Any displacement of a microsphere from the center of the trap either radial (a) or axial (b) results in a momentum change on the light beam that will cause a restoring force on the microsphere towards the centre of the trap. c) Optical tweezers can be combined with microfluidic flow cells. Thanks to this combination optical traps can rapidly be moved between different parallel flow channels. For example, microspheres can be trapped in channel 1, upon which DNA can be tethered in between the microspheres in channel 2, force experiments can be performed in a buffer of choice in channel 3, or the interaction of DNA with fluorescent probes can be monitored in channel 4.

tight laser focus creates a potential well for small particles, which we call an optical trap.

This entirely optical technique thus allows for the stable capture and movement of small objects inside a solution. By the creation of two optical traps, biomolecules such as DNA can be attached via (non-covalent) chemical bonds in between two optically trapped microspheres. By moving the two optical traps apart with a spatial resolution in the order of nanometers, the biomolecule gets stretched. The restoring force on the microspheres results in a displacement of the bead from the center of the optical trap and consequently in a deflection of the laser beam. The deflection of the outgoing laser beam is measured by projecting it on a position sensitive diode. By recording the power spectrum of bead oscillations inside the optical trap, the trap stiffness can be calibrated, and force can typically be measured with piconewton resolution [50]. Hence, optical tweezers can be used to manipulate biomolecules while at the same time measure their force response.

Apart from the high spatial and force resolution that can be achieved using optical tweezers, they provide at least three more advantageous aspects when studying biomolecules. First, the biomolecules can be studied in solution without a mechanical connection with the outside world. This renders the technique extremely stable with respect to noise and drift from the setup. Second, the ability to measure the molecule in solution, also

allows for combining it with microfluidic flow cells (Figure 1.5c). Thanks to the small dimensions of the channels in such a flow cell (tens to hundreds of micrometer), a laminar flow is obtained where mixture of parallel lanes due to turbulence is negligible [51]. Therefore, the combination of optical tweezers with such a flow cell allows for quick exchange of the surrounding solution simply by moving the traps from one parallel flow lane to another (Figure 1.5c). Finally, since optical tweezers are an entirely optical technique, combining it with imaging techniques is relatively straightforward.

1.4.2   Fluorescence microscopy

Since biomolecules are typically much smaller than the wavelength of visible light (a DNA molecule is around 2 nm wide, compared to 400-750 nm for the wavelengths in the visible spectrum), it is generally not possible to see them with normal light microscopy [52]. Instead, fluorescence microscopy is a widely used technique to visualize such small structures. Fluorescence is a quantum mechanical effect that relies on the absorption of a photon by a fluorophore and the subsequent emission of another photon with a slightly longer wavelength (Stokes shift). By shining light with a specific excitation wavelength on a sample containing fluorophores that are for example attached to proteins or DNA, the emission light can be separated from the excitation light based on wavelength thanks to the Stokes shift. By projecting the emission light onto a camera chip, an image of the sample is obtained.

Since most biomolecules are not fluorescent by themselves, they are often labeled with fluorophores to visualize them. Although this renders them visible with fluorescence microscopy, the bright spot on the camera chip resulting from a single fluorophore that emits light (point spread function, PSF), will have a width in the order of the wavelength of light, which is typically still much wider than the size of the biomolecule itself. If one would like to know the position of the biomolecule, it can pose a problem when they are so close together that their PSFs start to overlap. The minimal distance that these fluorophores must have to still distinguish them $d=\lambda/2NA$, is referred to as the diffraction limit, where λ is the wavelength of light and NA is the numerical aperture of the objective lens, typically a value close to 1.

In the last few decades several approaches to beat the diffraction limit have been developed, together referred to as super-resolution microscopy. One of those super-resolution microscopy techniques that has been

employed in this thesis is localization microscopy [53,54]. The idea behind this approach is that one cannot discriminate two fluorophores that are close together and emitting at the same time, but one is able to distinguish them if they would be visible at different times. The individual fluorophores can be localized with a precision that is dependent on the number of photons they emit. This has resulted in resolutions on the order of nanometers, indeed of similar dimension as biomolecules themselves.

1.5   Outline of this thesis

This thesis is dedicated to the development of a method to optically manipulate mitotic chromosomes. Here, I present a brief outline of this thesis:

Chapter 2 reviews the advances that have been made in the combination of optical tweezers and fluorescence microscopy for single-molecule investigations. An overview is provided on the different trap configurations (single-, dual- or quadruple trapping) that have been employed and for which type of assays they have been used. Finally, the chapter presents a few of the studies that combine these techniques to highlight the experimental potential of optical tweezers for single-molecule research.

Chapter 3 presents a step-by-step guideline to design and build a multi-color wide-field fluorescence microscopy module onto an existing optical tweezers setup. First, a description of a quadruple-trap optical tweezers setup is provided, which is used as a starting point to design the fluorescence module. This is followed by a detailed discussion of design considerations and a protocol to build the fluorescence module. The chapter also includes the description of a unique feature that allows for three-dimensional imaging of the sample without having to move the sample itself. These technical advances will greatly enhance the imaging capabilities of, among others, optically manipulated chromosomes.

In **Chapter 4** a methodology is presented that allows for the visualization of DNA binding proteins without the need to fluorescently label them. The method uses intermittently binding intercalators to stain bare DNA, but not protein-bound DNA sections. As such an image is retrieved where

protein bound regions appear darker than DNA regions without proteins. With diffraction-limited wide-field microscopy a time resolution of 190 ms is achieved. On the other hand, we show that we can visualize unlabeled protein patches as small as 180 nm by a strategy of localization microscopy where individual intercalator binding events are imaged and localized to obtain a super-resolution image of the protein bound DNA. The tools developed in this chapter are used in Chapter 5 and 6 for the visualization of chromosomes.

Chapter 5 presents a methodology to study human mitotic chromosomes using optical tweezers. To this end, chromosomes are site-specifically biotinylated, isolated from human cells and attached to microspheres via their telomeres. Subsequent stretching of the chromosomes using force-extension and oscillatory experiments reveal an extremely robust strain-stiffening response that is generic for all chromosomes measured. Interference with chromosome structure, using salt expansion or topoisomerase IIα depletion show a shift in the strain-stiffening response, which indicates that this behavior is a reflection of the network's structure. Therefore, we propose a model that explains the observed strain-stiffening behavior by the successive stiffening of serial elements in the chromosome's architecture.

Chapter 6 provides an outlook on the various research opportunities that will be facilitated by the work presented in this thesis. Preliminary data on some non-finished projects will be presented. The chapter will conclude with a discussion of potential directions of future research.

References

1.   Hooke, R. Micrographia. (1665).
2.   Virchow, R. Die cellularpathologie in ihrer begrundung auf physiologische und pathologische gewebelehre. (1859).
3.   Schwann, T. Mikroskopische untersuchungen uber die uebereinstimmung in der struktur und dem wachsthum der thiere und pflanzen. (1839).
4.   Crick, F. & Watson, J. Molecular structure of nucleic acids. Nature 171, 737–738 (1953).
5.   Watson, J. & Crick, F. Genetical implications of the structure of deoxyribonucleic acid. Nature 171, 964–967 (1953).
6.   https://global.britannica.com/science/DNA.
7.   https://commons.wikimedia.org/wiki/File:Animal_cell_cycle-en.svg.
8.   Alberts, B. Molecular Biology of the Cell. (2007).

1

9.   Speicher, M. R. & Carter, N. P. The new cytogenetics: Blurring the boundaries with molecular biology. Nat. Rev. Genet. 6, 782–792 (2005).

10. Sullivan, B. A., Blower, M. D. & Karpen, G. H. Determining centromere identity: Cyclical stories and forking paths. Nat. Rev. Genet. 2, 584–596 (2001).

11. Shay, J. W. & Wright, W. E. Telomeres and telomerase: three decades of progress. Nat. Rev. Genet. 20, 299–309 (2019).

12. Felsenfeld, G. & Groudine, M. Controlling the double helix. Nature 421, 448–453 (2003).

13. Batty, P. & Gerlich, D. W. Mitotic Chromosome Mechanics: How Cells Segregate Their Genome. Trends Cell Biol. 29, 717–726 (2019).

14. Ou, H. D. et al. ChromEMT: Visualizing 3D chromatin structure and compaction in interphase and mitotic cells. Science (80-.). 357, (2017).

15. Maeshima, K., Eltsov, M. & Laemmli, U. K. Chromosome structure: Improved immunolabeling for electron microscopy. Chromosoma 114, 365–375 (2005).

16. Wang, F. & Higgins, J. M. G. Histone modications and mitosis: Countermarks, landmarks, and bookmarks. Trends Cell Biol. 23, 175–184 (2013).

17. Oomen, M. E. & Dekker, J. Epigenetic characteristics of the mitotic chromosome in 1D and 3D. Crit. Rev. Biochem. Mol. Biol. 52, 185–204 (2017).

18. Biggs, R., Liu, P. Z., Stephens, A. D. & Marko, J. F. Effects of altering histone posttranslational modifications on mitotic chromosome structure and mechanics. Mol. Biol. Cell 30, 820–827 (2019).

19. http://worms.zoology.wisc.edu/zooweb/Phelps/ZWK99004k.jpeg.

20. Ganji, M. et al. Real-time imaging of DNA loop extrusion by condensin. Science (80-.). 360, 102–105 (2018).

21. Samejima, K. et al. Functional analysis after rapid degradation of condensins and 3D-EM reveals chromatin volume is uncoupled from chromosome architecture in mitosis. J. Cell Sci. 131, (2018).

22. Goloborodko, A., Imakaev, M. V., Marko, J. F. & Mirny, L. Compaction and segregation of sister chromatids via active loop extrusion. Elife 5, 1–16 (2016).

23. Kireeva, N., Lakonishok, M., Kireev, I., Hirano, T. & Belmont, A. S. Visualization of early chromosome condensation: A hierarchical folding, axial glue model of chromosome structure. J. Cell Biol. 166, 775–785 (2004).

24. Maeshima, K. & Laemmli, U. K. A Two-step scaffolding model for mitotic chromosome assembly. Dev. Cell 4, 467–480 (2003).

25. Poonperm, R. et al. Chromosome Scaffold is a Double-Stranded Assembly of Scaffold Proteins. Sci. Rep. 5, 1–3 (2015).

26. Roca, J. & Wang, J. C. DNA transport by a type II DNA topoisomerase: Evidence in favor of a two-gate mechanism. Cell 77, 609–616 (1994).

27. Samejima, K. et al. Mitotic chromosomes are compacted laterally by KIF4 and condensin and axially by topoisomerase IIα. J. Cell Biol. 199, 755–770 (2012).

28. Farr, C. J., Antoniou-Kourounioti, M., Mimmack, M. L., Volkov, A. & Porter, A. C. G. The α isoform of topoisomerase II is required for hypercompaction of mitotic chromosomes in human cells. Nucleic Acids Res. 42, 4414–4426 (2014).

29. Shintomi, K., Takahashi, T. S. & Hirano, T. Reconstitution of mitotic chromatids with a minimum set of purified factors. Nat. Cell Biol. 17, 1014–1023 (2015).

30. Earnshaw, W. C., Halligan, B., Cooke, C. A., Heck, M. M. S. & Liu, L. F. Topoisomerase II is a structural component of mitotic chromosome scaffolds. J. Cell Biol. 100, 1706–1715 (1985).

31. Ohta, S. et al. The Protein Composition of Mitotic Chromosomes Determined Using Multiclassifier Combinatorial Proteomics. Cell 142, 810–821 (2010).

32. Nielsen, C. F., Zhang, T., Barisic, M., Kalitsis, P. & Hudson, D. F. Topoisomerase IIa is essential for maintenance of mitotic chromosome structure. Proc. Natl. Acad. Sci. U. S. A. 117, (2020).

33. Finch, J. & Klug, A. Solenoidal Model for Superstructure in Chromatin. Proc. Natl. Acad. Sci. 73, 1897–1901 (1976).

34. Gibcus, J. H. et al. A pathway for mitotic chromosome formation. Science (80-.). 359, (2018).

35. Walther, N. et al. A quantitative map of human Condensins provides new insights into mitotic chromosome architecture. J. Cell Biol. 217, 2309–2328 (2018).

36. Paulson, J. R. & Laemmli, U. K. The structure of histone-depleted metaphase chromosomes. Cell 12, 817–828 (1977).

37. Terakawa, T. et al. The condensin complex is a mechanochemical motor that translocates along DNA. Science (80-.). 358, 672–676 (2017).

38. Sun, M., Biggs, R., Hornick, J. & Marko, J. F. Condensin controls mitotic chromosome stiffness and stability without forming a structurally contiguous scaffold. Chromosom. Res. 26, 277–295 (2018).

39. Marko, J. F. & Siggia, E. D. Stretching DNA. Macromolecules 28, 8759–8770 (1995).

40. Broedersz, C. P. et al. Cross-link-governed dynamics of biopolymer networks. Phys. Rev. Lett. 105, 2–5 (2010).

41. Nicklas, R. B. Measurements of the force produced by the mitotic spindle in anaphase. J. Cell Biol. 97, 542–548 (1983).

42. Neuman, K. C. & Nagy, A. Single-molecule force spectroscopy: Optical tweezers, magnetic tweezers and atomic force microscopy. Nat. Methods 5, 491–505 (2008).

43. Claussen, U., Mazur, A. & Rubtsov, N. Chromosomes are highly elastic and can be stretched. Cytogenetics and Cell Genetics vol. 66 120–125 (1994).

44. Hliscs, R., Mühlig, P. & Claussen, U. The nature of G-bands analyzed by chromosome stretching. Cytogenetic and Genome Research vol. 79 162–166 (1997).

45. Houchmandzadeh, B., Marko, J. F., Chatenay, D. & Libchaber, A. Elasticity and structure of eukaryote chromosomes studied by micromanipulation and micropipette aspiration. J. Cell Biol. 139, 1–12 (1997).

46. Poirier, M., Eroglu, S., Chatenay, D. & Marko, J. F. Reversible and irreversible unfolding of mitotic newt chromosomes by applied force. Mol. Biol. Cell 11, 269–276 (2000).

47. Sun, M., Kawamura, R. & Marko, J. F. Micromechanics of human mitotic chromosomes. Phys. Biol. 8, (2011).

48. Ashkin, A., Dziedzic, J. & Yamane, T. Optical trapping and manipulation of single cells using infrared laser beams. Nature 330, 769–771 (1987).

49. Ashkin, A., Dziedzic, J. M., Bjorkholm, J. E. & Chu, S. Observation of a single-beam gradient force optical trap for dielectric particles. Opt. Angular Momentum 11, 196–198 (1986).

50. Neuman, K. C. & Block, S. M. Optical trapping. Rev. Sci. Instrum. 75, 2787–2809 (2004).

51. Leal, L. G. Laminar flow and convective transport processes. (1992).

52. Helmholtz, H. On the limits of optical capacity of the microscope. Mon. Microsc. J. 16, 15–39 (1876).

53. Betzig, E. et al. Imaging Intracellular Fluorescent Proteins at Nanometer Resolution. Science (80-.). 313, (2006).

54. Schoen, I., Ries, J., Klotzsch, E., Ewers, H. & Vogel, V. Binding-activated localization microscopy of DNA structures. Nano Lett. 11, 4008–4011 (2011).

Recent advances in biological single-molecule applications of optical tweezers and fluorescence microscopy

2.1   Abstract

Over the past two decades, single-molecule techniques have evolved into powerful tools to study many fundamental biological processes. The combination of optical tweezers with fluorescence microscopy and microfluidics provides a powerful single-molecule manipulation and visualization technique that has found widespread application in biology. In this combined approach, the spatial (~nm) and temporal (~ms) resolution, as well as the force scale (~pN) accessible to optical tweezers is complemented with the power of fluorescence microscopy, which provides information of the local presence, identity, spatial dynamics, and conformational dynamics of single biomolecules. Together, these techniques allow comprehensive studies of, among others, molecular motors, protein–protein and protein–DNA interactions, biomolecular conformational changes, and mechano-transduction pathways. In this chapter, recent applications of fluorescence microscopy in combination with optical trapping are discussed. After an introductory section, we provide a description of instrumentation together with the current capabilities and limitations of the approaches. Next, we summarize recent studies that applied this combination of techniques in biological systems and highlight some representative biological assays to mark the exquisite opportunities that optical tweezers combined with fluorescence microscopy provide.

2.2   Introduction

The exploration of single-molecule systems and their interactions with each other in terms of mechanical forces has substantially benefitted from recent advances in the now well-established field of optical tweezers. The very high sensitivity (pN, nm, kBT) and the wide temporal resolution (s to ms) of optical tweezers can be used to non-invasively measure the mechanics of single molecules and their interactions with other molecules. It has been about three decades since Arthur Ashkin presented the first application of optical tweezers in biology[1], and since then optical tweezers have become one of the most widely used single-molecule tools in biology. What makes the use of optical tweezers even more compelling is its compatibility with various types of light microscopy, such as bright-field, differential-interference-contrast, phase-contrast and fluorescence microscopy. Not surprisingly, optical trapping was soon combined with fluorescence microscopy as a method for visualizing single molecules. In the first combination study, a long piece of DNA was labelled with ethidium bromide and stretched between two beads held in two optical traps[2]. The relaxation of the DNA upon release of one bead could be followed by simply watching the movements of the fluorescently labelled DNA.

In the last two decades, a variety of fluorescence techniques have been successfully combined with optical tweezers. Epi-illuminated wide-field and total internal reflection (TIRF) fluorescence microscopy, being the most straightforward to implement, have been adopted first[3–7]. More recently, confocal fluorescence microscopy and stimulated emission depletion (STED) super-resolution microscopy have been integrated with optical tweezers[8–15]. Each of these visualization approaches has its own set of strengths and weaknesses for the analysis of protein dynamics.

Addition of fluorescence microscopy enables direct visualization of individual proteins on biomolecules such as DNA, resulting in information on the presence of DNA–protein complexes, even when they do not induce a detectable change in the signals measured with optical tweezers. Moreover, fluorescence microscopy allows counting the number of proteins bound to the DNA. In addition, dynamic processes like diffusion, translocation and binding kinetics of proteins can be directly monitored using fluorescence imaging. Förster resonance energy transfer (FRET) allows distance measure-

ments on the nanometer scale and can be used to study the conformational dynamics of DNA–protein complexes.

Simultaneous application of optical tweezers and fluorescence microscopy reaches further than the single-molecule field of biophysics. In recent years, optical tweezers have been applied more and more *in vivo*. Several research groups have used optical tweezers to hold cells at a fixed position, which was a major breakthrough in single-cell studies, allowing spatial fixing without surface interactions in a sealed device and controlled environment, while enabling continuous observation using advanced imaging techniques[16,17]. The application of combined optical tweezers and fluorescence microscopy has also been extended to investigate cell-scaffold adhesion[18], immunological studies and phagocytosis[19], permeability as well as molecular partitioning associated with phase transitions in vesicles and lipid bilayers[20–22], the influence of membrane proteins[23,24], and membrane-cytoskeleton interactions[25].

In this chapter, we will focus on the broad collection of *in vitro* single-molecule assays that have been demonstrated in recent years. We will also discuss several examples of *in vivo* research providing an impression of the advances in this field as well, albeit without going into detail. We will start with providing a description of the fluorescence and microfluidics techniques that have been combined successfully with optical tweezers. We will put emphasis on the advantages and disadvantages of these combinations, which could serve as guidelines for choosing the most appropriate method when designing an experiment. We will also provide an overview of commercial instruments. Next a collection of recent studies that have combined optical tweezers with fluorescence microscopy will be presented, categorized according to the optical trapping configuration and the fluorescence microscopy technique used. We will discuss examples drawn from across the single-molecule literature, ranging from DNA enzymes, microtubule-protein interactions, DNA/protein conformational dynamics, DNA mechanics, DNA intercalators, lipid-membrane fusion, bacterial motility, and ultimately several FRET studies on nucleosomes and DNA helicases. We aim to highlight the excellent opportunities that the combination of optical tweezers and fluorescence microscopy provides for studying the mechanical properties of DNA (length, flexibility and elasticity), the kinetics and mechanochemistry of motor proteins, and properties of DNA intercalators.
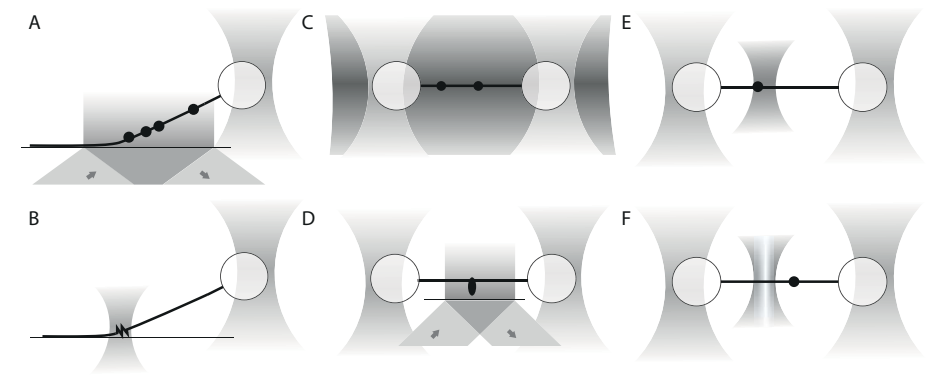
Figure 2.1: Concurrent optical trapping and fluorescence microscopy. (A) Combination of TIRF fluorescence microscopy with single-trap optical tweezers, where one end of the DNA-protein complex is tethered to an optically trapped microsphere and the other to a surface. Black-thick line: DNA molecule; Black circles: proteins. (B) Combination of confocal fluorescence microscopy with single-trap optical tweezers with one end of the DNA is tethered to an optically trapped microsphere and the other to a surface. (C) Wide-field microscopy combined with dual-trap optical tweezers where both microspheres are being held in two separate optical traps. (D) TIRF microscopy combined with dual-trap optical tweezers with both microspheres being held in two separate traps. The suspended filament (black line) can interact with a single-molecule motor protein (black oval) which is bound to the surface of a pedestal formed on a coverslip. (E) Combination of confocal fluorescence microscopy with dual-trap optical tweezers, where both microspheres are being held in two separate optical traps. (F) Combination of STED fluorescence microscopy with dual-trap optical tweezers with both microspheres being held in two separate optical traps.

2.3   Instrumentation

The combination of optical tweezers and fluorescence microscopy provides a versatile platform that opens up a range of opportunities to gain insight into complex biomolecular transactions. Optical tweezers can hold and move microscopic dielectric particles thanks to transfer of momentum from photons to the object. When forces act on the object, it is pulled out of the laser focus, which results in a deflection of the laser beam that can be detected by a position-sensitive detector. For imaging purposes, a single optical trap can be used to hold objects (Figure 2.1 A-B). However, in order to both visualize and record the tension on a biomolecule a second anchor is required, which can be provided by a surface or by a second optical trap. In an optical trapping system it is relatively simple to implement a second optical

trapping beam by splitting the trapping light based on polarization (Figure 2.1 C-F). In the last two decades, optical trapping has been widely employed in different configurations and excellent reviews have been written on the technical aspects of its implementation[26–28].

The simultaneous application of optical tweezers and fluorescence microscopy poses several additional technical challenges. For example, the light intensities used for the two techniques differ orders of magnitude, which requires efficient separation of trapping and fluorescence light. Moreover, the combination of optical tweezers and fluorescence microscopy is further complicated by optical-trap-induced photobleaching of fluorophores. Despite these challenges a variety of fluorescence-microscopy techniques has been successfully combined with optical tweezers (Figure 2.1 A-F). We categorize the most recent articles combining optical tweezers and fluorescence microscopy in Table 2.1, according to the optical-trap configuration and the fluorescence-microscopy technique employed. In this section we will discuss the strengths and technical difficulties of combining specific fluorescence microscopy techniques with an optical tweezers system.

Epi-illuminated wide-field fluorescence microscopy is the simplest fluorescence microscopy technique that has been combined with optical tweezers (Figure 2.1 C). It allows for direct visualization of a whole field of view. Moreover, modern EMCCD or sCMOS cameras with improved signal-to-noise-ratios can image single molecules with a temporal resolution in the order of milliseconds[29]. Illumination of the sample with a relatively wide, parallel light beam often results in high background fluorescence. This limits the concentration of fluorophores in solution at which it is still possible to detect single fluorophores to about 1nM[29].

Total internal reflection fluorescence (TIRF) microscopy significantly reduces the background fluorescent signal. The reflection of the excitation beam on the sample-cover glass interface causes an evanescent field of excitation light that decays exponentially away from the interface, with a typical depth of only a few hundred nanometers inside the sample volume. This substantially reduces background fluorescence, but at the same time requires the experiments to be carried out close to the surface. TIRF is therefore often combined with a trapping configuration where the biomolecule is tethered between a surface and an optically trapped bead or in between two beads that are brought close to a pedestal in the flow chamber (Figure

2.1 A,D). A disadvantage of the surface-tethered configuration is that the biomolecule is not homogeneously illuminated due to the angle it makes with the interface. Furthermore, measuring close to a surface can sometimes interfere with the biological processes under investigation. Alignment of this fluorescence microscopy technique is only slightly more challenging than an epi wide-field fluorescence microscope and good commercial implementations in inverted microscopes exist.

Confocal fluorescence microscopy has the advantage that background fluorescence can be substantially reduced by spatial filtering of the fluorescence signal using a pinhole, reducing the out-of-focus fluorescence background. In this way, single-molecules can be detected in a solution containing about 100nM fluorophores. This technique, however, requires much more precise alignment and is therefore substantially more challenging to combine with optical tweezers. Visualizing the whole sample requires scanning, since fluorescence is only detected in a very small volume of the sample. Without implementing scanning, confocal fluorescence microscopy has been applied mostly to measure Förster resonance energy transfer (FRET) from a single molecule at a fixed position (Figure 2.1 B,E). Such FRET measurements have a sub-nanometer spatial resolution[8] and are therefore very suitable to measure conformational changes of biomolecules.

Scanning confocal fluorescence microscopy (also including stimulated emission depletion (STED) microscopy) has also been combined with optical tweezers. Scanning the confocal spot over the sample is required to generate an image of part of the sample, which prevents continuous visualization of the whole sample. When detecting single molecules, this scanning approach is typically slower than using camera-based wide-field fluorescence approaches. To overcome this problem, Heller et al. developed a one dimensional scanning approach, where the two optical traps are being used to linearize the biomolecule (in this case DNA), such that only one-dimensional scanning is necessary[15]. Implementation of one-dimensional STED allowed for a five-fold enhancement of the diffraction-limited spatial resolution (to ~50 nm). This higher spatial resolution allows STED to measure at higher fluorophore concentrations, both in solution and on the DNA itself. A drawback of the 1D-STED approach are the high laser intensities required to generate stimulated emission, substantially increasing photobleaching.
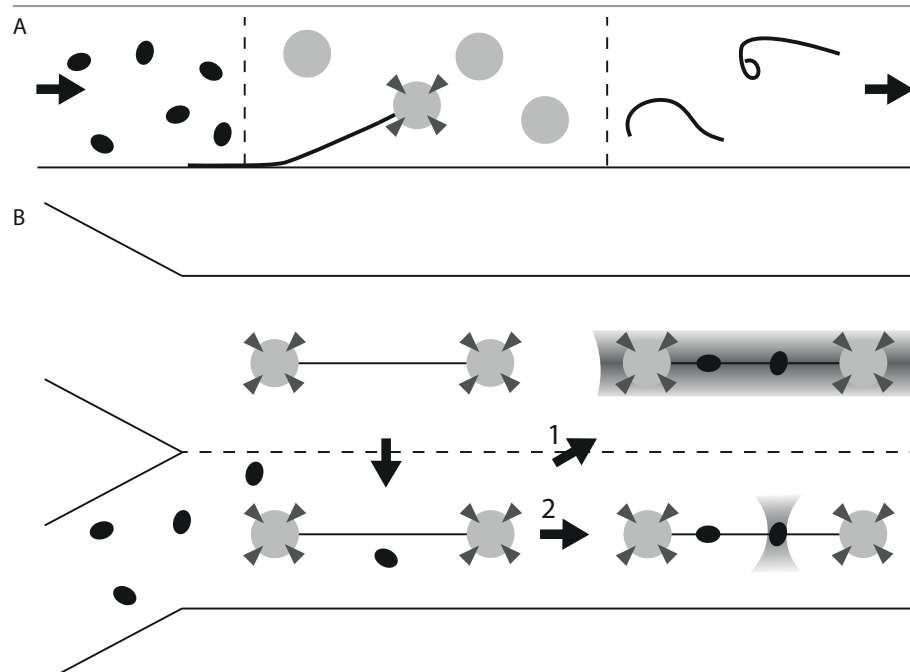
Figure 2.2: Illustration of different geometries of microfluidic chips used in optical tweezers. (A) Sequential delivery of buffers into the micro-channel. This configuration allows for the construction of complex structures such as biomolecule attachment to a surface with one end and subsequently attachment to a bead with the other end. Arrows indicate the direction of flow. (B) Insertion of buffers in a parallel fashion. This geometry allows for rapid switching of buffer composition by moving the traps to another laminar "lane". This configuration enables imaging both in the same lane with labelled entities still present (arrow 1), or in a different lane where no fluorophores are present in the solution (arrow 2).

Smart and creative application of microfluidic chips that contain micrometer-to-millimeter-sized channels have also led to a wealth of new experimental possibilities. Two main experimental schemes can be distinguished (Figure 2.2). In the first approach, buffers are inserted into the micro-channels in a sequential manner (Figure 2.2 A), which allows to construct complex structures such as biomolecules that are attached with one end to a surface and, subsequently, with the other to a bead. In the second approach, buffers are inserted in a flow cell side-by-side without barriers in between (Figure 2.2 B). Because the flow is laminar, mixing of buffer flows does not occur. This implementation of microfluidic chips is particularly powerful in optical tweezers configurations without surface tethers, since it allows rapid switching of the buffer composition simply by moving the trap(s) to another laminar

"lane". This rapid switching can, for example, be exploited to suppress high background-fluorescence signals by imaging in a flow channel containing no fluorophores, after incubating in another channel containing the fluorophore.

The unique power provided by these sophisticated single-molecule instruments, makes studying biological processes almost straightforward. It can, however, be daunting to decide which technique or equipment to use and to know how to deal with technical complexities and maintenance of the instruments. Access to commercial alternatives will undoubtedly make this powerful and versatile combination of techniques accessible to a broad range of researchers in biophysics, biochemistry, drug discovery, toxicology and many other fields. One of the few instruments combining both optical tweezers and fluorescence microscopy techniques and being commercially available is the JPK Nano Tracker™. The optical tweezers system from JPK instruments is designed around a standard inverted microscope and can be combined with various fluorescent techniques. More recently, LUMICKS introduced the C-Trap™. This instrument combines optical tweezers, confocal fluorescence microscopy or STED nanoscopy and an advanced microfluidics system in a fully integrated configuration. With the development of commercial fluorescence techniques, it is to be expected that single-molecule methods will find wider application in the life and biomedical sciences, providing access to a novel way of studying biomolecular processes in a quantitative way.

2.4   Applications
In the following we will discuss applications of different combinations of optical tweezers and fluorescence microscopy and highlight their capabilities and key practical aspects.

2.4.1   Single optical trap
One of the main optical trapping geometries used to study biomolecular interactions is single-trap optical tweezers. Over the past two decades, several studies have employed different configurations of fluorescence microscopy combined with a single-trap geometry, which has yielded valuable knowledge about biomolecular transactions (Table 2.1). Here, we will first describe

	Single trap			Dual trap		Miscellaneous
	1 trap (hold)	1 trap + flow	1 trap + surface	2 traps	2 traps + surface	
Wide-field	• Erikson et al., 2006; • Pang et al., 2014; • Rasmussen et al., 2008	✓ Bianco et al., 2001; ✓ Bianco et al., 2007; ✓ Galletto et al., 2006; ✓ Handa et al., 2005; • Hilario et al., 2009; • Pezza et al., 2010; • van Mameren et al., 2009	• Akiyoshi et al., 2010; • Ali et al., 2004; • Dong et al., 2010; • Ferrer et al., 2008; • Fujita et al., 2012; • Funatsu et al., 1997; • Iwaki et al., 2006; • Iwaki et al., 2008; ✓ Kudalkar et al., 2015; ✓ Lee et al., 2013; • Lee et al., 2014; • Ngo et al., 2016; • Sarangapani et al., 2014; • Tarsa et al., 2007; ✓ Umbrit et al., 2014	✓ Arai et al., 1999; ✓ Bao et al., 2003; • Biebricher et al., 2013; ✓ Biebricher et al., 2015; ✓ Brouwer et al., 2015; ✓ Candelli et al., 2014; • Farge et al., 2012; • Farge et al., 2014; ✓ Gross et al., 2011; ✓ King et al., 2013; ✓ King et al., 2016; • Landry et al., 2009; ✓ Mears et al., 2014; ✓ Min et al., 2009; • Murade et al., 2009; ✓ Saito et al., 1994; • van den Broek et al., 2010; ✓ van Mameren et al., 2006; ✓ van Mameren et al., 2009; ✓ van Mameren et al., 2009	✓ Harada et al., 1999; ✓ Ishijima et al., 1998; ✓ Iwane et al., 2005; ✓ Komori et al., 2009; ✓ Tanaka et al., 1998; ✓ Tanaka et al., 2008; • Watanabe et al., 2003	• Erikson et al., 2010; • Inman et al., 2014; • Mirsaidov et al., 2008; • Sasuga et al., 2006; • Yogo et al., 2010
Confocal	• Benedix et al., 2010; • Benedix et al., 2011; • Kyrsting et al., 2011; • Leijnse et al., 2015; • Podlipec et al., 2015; • Tam et al., 2010		✓ Brenner et al., 2016; • Bornschlögl et al., 2013; • Grashoff et al., 2010; • Hohng et al., 2007; • Maffeo et al., 2014; • Ngo et al., 2015; • Zhou et al., 2011	✓ Comstock et al., 2015; ✓ Duesterberg et al., 2015; ✓ Suksombat et al., 2015; • Wolfson et al., 2015		
STED				✓ Heller et al., 2013		

Table 2.1: Summary of the most recent literature that describes various combinations of optical tweezers and fluorescence microscopy. The articles in each column of the table are organized according to their optical trap configuration (vertically) and the fluorescence microscopy (horizontally) techniques that is used. The articles within a cell of the table are organized alphabetically based on the last name of the first author. In this chapter, we specifically focus on those combinations that are highlighted with double-line borders. The tick marked articles are discussed in more detail, both the biological assay used as well as a short summary of the pros and cones of the used combination of techniques.

some of these studies in which a single trap was used in combination with flow stretching and wide-field microscopy. Next, we will focus on studies in which one end of the biomolecule was tethered to an optically-trapped microsphere and the other to a surface, while being visualized using wide-field and TIRF microscopy, a geometry that provides the simplest possible layout that facilitates force and displacement measurements. Finally, we will highlight how confocal microscopy in combination with the single-trap/surface geometry can advance our knowledge of DNA/ protein conformational dynamics by enabling FRET measurements.

DNA Enzymes

A tremendous amount of new insights in DNA repair enzymes has been obtained using a DNA attached from one side to an optically trapped bead and stretched by buffer flow (see Table 2.1). Handa et al. described a procedure to directly track DNA translocation by the *E. coli* RecBCD helicase enzyme[30]. To directly visualize a rapidly moving RecBCD molecule, a 40 nm streptavidin-coated fluorescent bead (nanoparticle) was attached to RecBCD that had been biotinylated *in vivo* at a unique site on RecD. The biotinylated DNA was separately bound to a streptavidin-coated polystyrene bead and then mixed with the RecBCD that had been tagged with the fluorescent bead. The bead-DNA-RecBCD-nanoparticle complex was captured by an optical trap and then moved to a second channel of a flow cell containing ATP to start translocation. The position of the nanoparticle relative to the microsphere in their experiments was determined from individual video frames and velocities were determined. This assay allowed determination of the fast moving rate of RecBCD (up to 1835 bp/s; 0.6 µm/s). Furthermore, the translocation rate of RecBCD was determined on a DNA containing two χ -loci, a recombination hotspot recognized by RecBCD, which was known to reduce translocation speed of RecBCD. Using this substrate, recBCD pauses were observed on specific locations, indicating that RecD did not dissociate but underwent conformational modification, upon interacting with a χ-locus. This approach can be generally applied to other rapidly translocating motor proteins on DNA.

Using a slightly different approach, Bianco et al.[31] visualized in real time the DNA network formation and cross-bridging activity of RAD54 oligomers,

a DNA-repair and recombination enzyme in eukaryotes. This was achieved by manipulating two fluorescently labelled (fluorescent dye YOYO-1) DNA–bead complexes trapped side-by-side, using two optical tweezers in a flow cell. Preformed RAD51-RAD54 nucleoprotein filaments and ATP were introduced by moving the two DNA tethers to a second channel, initiating pairing of the two DNA molecules. These measurements revealed that RAD54 oligomers possess a unique ability to cross bridge or bind double-stranded DNA molecules positioned in close proximity, stimulating the formation of DNA networks, and priming the DNA for rapid and efficient DNA-strand exchange by the recombinase RAD51.

Hilario et al.[32] also used a fluorescent RAD51 to directly visualize nucleation, assembly, and disassembly of individual nucleoprotein filaments. Using this approach, they revealed that the rate of RAD51-nucleoprotein growth increases with a third-order dependence on RAD51 concentration. They determined that a minimum of 2–3 monomers of RAD51 is required to form a stable nucleus, based on the RAD51-concentration dependence of nucleation.

**Interactions of proteins with microtubules**
Combinations of optical trapping with fluorescence microscopy have made important contributions to mitosis and meiosis fields[5,33], and in particular to how kinetochores – the molecular machines that drive chromosome separation - are attached to microtubules. To this end, a combination of the single-trap/surface geometry and TIRF microscopy was used by Umbreit et al.[34] to investigate how Dam1, one of the kinetochore subcomplexes, influences kinetochore–microtubule attachment. They quantified the residence time (5.3 ± 0.5 s) and diffusion (0.021 ± 0.001 mm²s⁻¹) of Dam1 complex on microtubules using TIRF microscopy. In addition, they determined the strength of microtubule attachments (7.4 ± 0.4 pN) using an optical trap-based rupture force assay, in which they decorated a polystyrene bead with the Dam1 and allowed it to interact with one side of a microtubule that was attached to the surface with the other side.

In a similar approach, Kudalkar et al.[35] aimed to understand force transmission throughout the kinetochore and to discern the precise role of two other kinetochore subcomplexes, MIND and Ndc80. They found that MIND

dramatically reduced the microtubule binding time of Ndc80 (Figure 2.3). In contrast, MIND alone did not interact with microtubules, even when added at high concentrations, indicating that MIND activates the microtubule-binding activity of the Ndc80 complex. By means of a rupture-force assay with a constant loading rate, the strength of the MIND–Ndc80 linkage was probed. By performing a dual-label TIRF experiment Kudalkar and coworkers demonstrated that MIND does not enhance Ndc80 oligomerization, but induces a conformational change in the Ndc80 complex, activating the microtubule-binding domains.

DNA helicases
The configuration of a single-trap optical tweezers and TIRF discussed above has also been used by Lee et al.[36] to study dynamics of the *E. coli* helicase/translocase, UvrD, on a long ssDNA substrate. They demonstrated UvrD binding to and translocation along ssDNA by tracking the position of individual UvrD fluorescent spots and determined the number of UvrD monomers from fluorescence intensity and counting the number of photobleaching
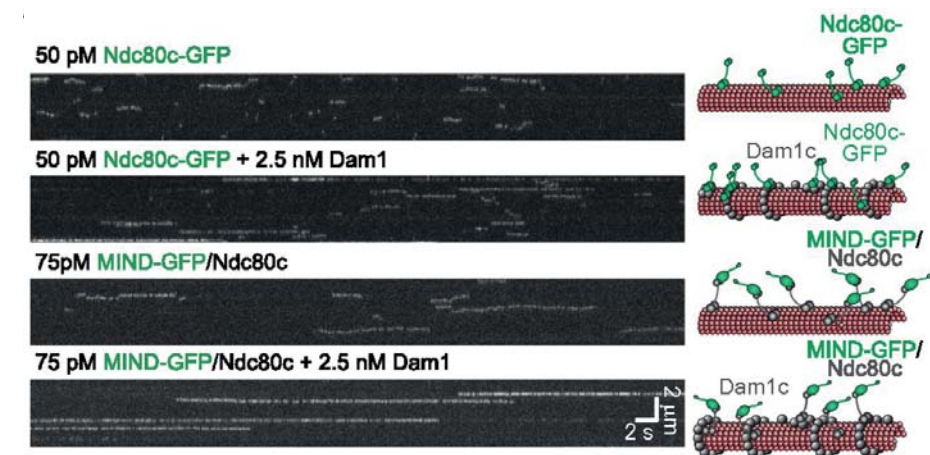
Figure 2.3: Effect of MIND subcomplex on microtubule binding time of Ndc80. Left: Representative TIRF kymographs of Ndc80c-GFP, Ndc80c-GFP plus Dam1c, MIND-GFP/Ndc80c, and MIND-GFP/Ndc80c plus Dam1c. Right: Diagrams denote each GFP tagged complex (ovals) and untagged (circles) complex binding to microtubules in kymograph on left. Adapted with permission from Kudalkar et al.[35], 2015.

steps. In addition, using the force measured from the optical tweezers they monitored the unwinding activity. They determined that the processivity of UvrD translocation along ssDNA is 1260 (±60) nt, with a velocity of 193 (±2) nts[-1]. UvrD monomer translocation stopped at a ssDNA/dsDNA junction, indicating that the translocating UvrD monomers do not make a transition to unwinding duplex DNA.

2.4.2 Dual-trap optical tweezers

The use of two optical traps has several advantages over the single optical trap configurations. First, since there is no need for surface tethering, measurements can be performed far from possibly interfering surfaces. Second, a microfluidic device can be used to rapidly change buffer conditions[37,38]. Third, since both traps can be positioned independently, the user has three dimensional control over the biomolecular construct that is trapped. Fourth, the dual-trap configuration also has advantages for imaging. Since the traps can be positioned horizontally with respect to the imaging plane, homogeneous illumination is more easily obtained. This makes it possible to perform epi-illuminated wide-field, TIRF, (scanning) confocal as well as STED experiments. These different configurations have been adopted widely (Table 2.1). Here we will focus on several applications the dual-trap optical tweezers approach in combinations with fluorescence microscopy.

DNA mechanics

The dual-trap configuration has been broadly adopted to study the mechanics of biomolecules tethered between two optically trapped beads. Arai et al. used this approach to tie knots in actin and DNA in a high viscosity medium that prevented polymers relaxations[6]. They were able to estimate knot diameters by comparing the fluorescence intensity of a knot with that of the unknotted polymer. In a similar assay, Bao et al. studied knot behavior in DNA[39]. They were able to tie several types of knots in the DNA and observed and quantified the diffusion of knots along the DNA.

Also other aspects of dsDNA mechanics have been studied extensively. In particular, force extension-behavior has been studied using optical tweezers alone[27,28,40,41], revealing that DNA acts as an entropic spring at forces below 2 pN, followed by an enthalpic regime where the DNA is extended.

At forces above 65 pN, DNA overstretches and only a small rise in force is required to extend the DNA to 1.7 times its length. The molecular nature of this overstretching transition had been fiercely debated. Combinations of fluorescence microscopy and optical tweezers have helped settling the debate, thanks to the local information provided by fluorescence microscopy[42,43].
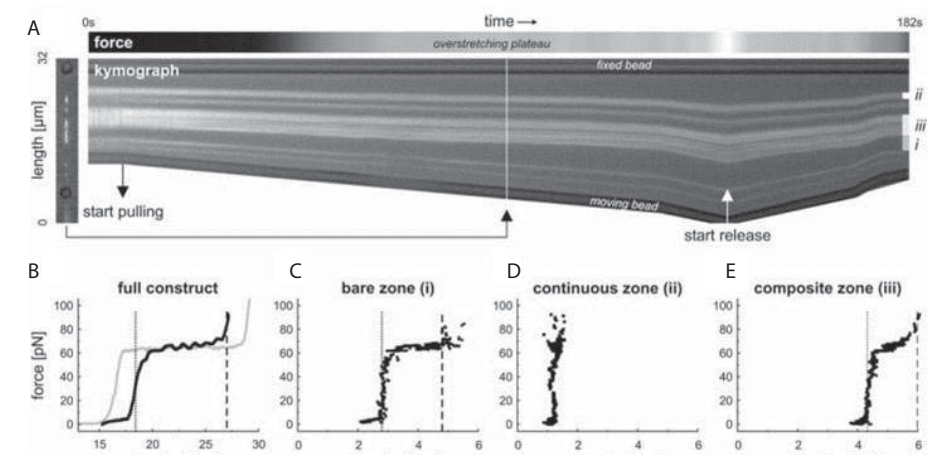
In particular, to study the local DNA configuration during overstretching, van Mameren et al. used dual-color epi-illuminated wide-field fluorescence microscopy to image intercalating dyes specific for dsDNA and ssDNA binding proteins for ssDNA[44]. The DNA construct was attached to the beads with the two opposite strands allowing the DNA to rotate freely with respect to the trapped beads. The intercalator-labelled fraction of the DNA, usually forming a single, continuous patch in the DNA, decreased linearly with extension. The remainder of the DNA was labelled by ssDNA binding protein, indicating that overstretching can be due to force-induced melting of the dsDNA, resulting in unpeeling of the DNA from the DNA ends. By applying a gentle flow perpendicular to the DNA, they could also observe the ssDNA being flow stretched, thereby confirming their hypothesis. In a follow-up study, King et al. performed experiments on torsionally unconstrained dsDNA without free ends, using fluorescent reporters for ssDNA and dsDNA[45]. Under high-salt conditions, during overstretching, part of the DNA was labelled by neither reporter, indicating that a third form of DNA, S-DNA, is involved. S-DNA is a DNA-conformation proposed before, in which base pairing is still intact but the helicity is largely lost. Under low-salt conditions, patches of the DNA (corresponding to regions with low AT content) could be stained by the ssDNA probe, indicating that local melting bubbles formed. These results directly show that the overstretching of dsDNA can have three different products, peeled ssDNA, ssDNA melting bubbles and S-DNA and that the ratio between these three depends on sequence, the presence or absence of free DNA ends and salt concentration. More recently, King et al. determined the mechanics of torsionally constrained dsDNA[42]. They found evidence for an additional, previously predicted DNA conformation, P-DNA, with the phosphate backbone facing inwards and the bases outwards, which is substantially overwound. From the fluorescence data, the percentage of DNA in the P-DNA form could be estimated to be 20-30% in good agreement with a previous prediction[46].
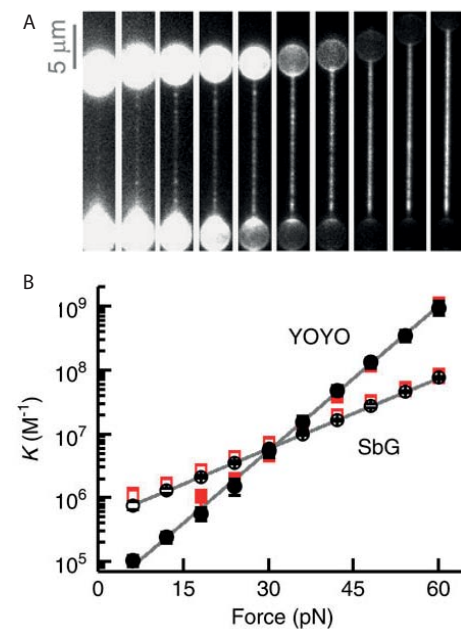
Figure 2.4: Force-dependent DNA intercalation of a mono- (SbG, open symbols) and a bis-intercalator (YOYO, solid symbols) at 1,000mM NaCl. (A) DNA elongation and representative fluorescence images as a function of tension. (B) Binding constant as a function of tension, calculated using elongation data. Adapted with permission from Biebricher et al., 2015[48].

2

Figure 2.5: Elastic properties of a single 48 kbp λ-dsDNA molecule partly coated with fluorescent RAD51. (A) Fluorescence image (left) of such an assembly, tethered between two streptavidin-coated polystyrene beads. Kymograph (right) generated from the successive frames of the movie recorded during extension of the construct. The corresponding force time trace is depicted in gray scales (top bar; white corresponds to 90 pN). (B) Force-extension curve corresponding to the construct in A. The gray trace shows a bare λ-DNA reference curve. (C–E) Force-extension curves of the bare zone (i), the continuous fluorescent zone (ii) and the composite fluorescent zone (iii) as indicated on the right of the kymograph. Adapted with permission from van Mameren et al., 2006[49].

DNA intercalators

DNA intercalators, which bind in-between adjacent base pairs of dsDNA are often used as a fluorescent marker for DNA visualization. It is, however, well known that intercalators perturb the structure and mechanical properties of DNA. To elucidate the effect of intercalators on DNA and to test under what conditions they can be used as DNA probes, Murade et al. and Biebricher et al. combined dual-trap optical tweezers and fluorescence microscopy[47,48]. Both studies showed that there is a linear correlation between DNA extension and total intercalator fluorescence intensity, indicating that intercalator binding increases with tension. Biebricher et al. quantified the dsDNA binding and unbinding kinetics of several intercalators[48]. A combination of force and fluorescence measurements allowed determination of intercalator coverage over an unprecedented four-orders-of-magnitude range. They showed that the force dependence of intercalator binding is mostly governed by the strongly force-dependent unbinding rate (Figure 2.4). The unbinding rate varies over seven orders of magnitude, depending on intercalator species, salt conditions and DNA tension. This detailed quantification of intercalator-binding and unbinding kinetics provides the insights needed

for researchers to select the optimal intercalator species and conditions for a given application.

DNA enzymes

Dual-trap optical tweezers also allow quantitative analysis of DNA-binding proteins. One such protein that has frequently been studied this way is RAD51, which forms ATP-dependent filaments on dsDNA and ssDNA. Van Mameren et al. used a combination of optical tweezers and fluorescence microscopy to study the mechanics and kinetics of RAD51 filament on dsDNA[49]. They showed that, in the absence of ATP hydrolysis, RAD51 forms immobile filaments that remain stably bound to DNA even at high forces. Moreover, the measurements allowed estimating the dsDNA length increase upon binding RAD51 to be 150%. Notably, the filaments of RAD51 on DNA are very rigid and could hardly be stretched when the DNA molecule is pulled (Figure 2.5).

Using a similar approach, Candelli et al. focused on RAD51-filament nucleation and growth on both dsDNA and ssDNA[50]. First, by counting the number of nuclei that formed in a given time they determined the nucleation rate, which increased with RAD51 concentration. From the fluorescence intensity of individual nuclei they determined the number of RAD51 monomers per nucleus and found a wide distribution of nucleus sizes. In addition, growth of filaments was studied with a single-molecule fluorescence recovery after photobleaching (FRAP) assay, in which nuclei were first completely photobleached, followed by incubation of the DNA in a RAD51 containing buffer. When a new fluorescent spot occurred at the same location as a previous, photobleached one, this was interpreted as a growth event. From such experiments the filament growth rate was determined. Remarkably, both nucleation and growth rates are force dependent for RAD51 binding to dsDNA, but not for binding to ssDNA.

Van Mameren et al. looked at the disassembly of RAD51 filaments from dsDNA[51]. Preformed RAD51-nucleoprotein filaments were rapidly brought from a non-hydrolyzing to an ATP-hydrolyzing condition by moving them to another channel in the flow cell. While holding the traps at a fixed distance,
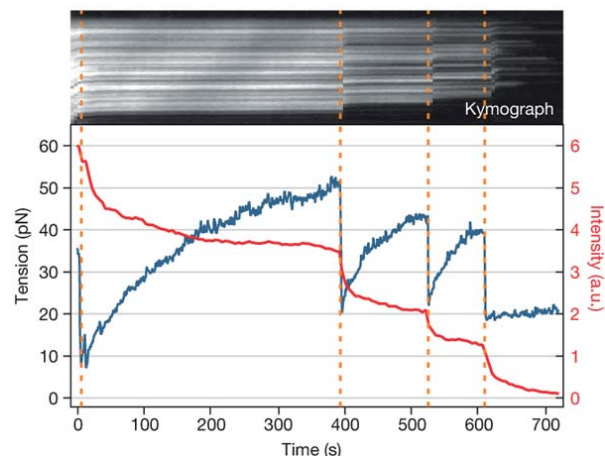
Figure 2.6: RAD51 disassembly rate is reversibly reduced by DNA tension. Top: Kymograph of a RAD51–dsDNAcomplex, held at fixed length. Bottom: Intensity trace (red, descending line from top left) and tension trace (blue, ascending line from bottom left) of a RAD51–dsDNAcomplex. Tension stalled disassembly is reinitiated by tension release (orange dashes). Adapted with permission from van Mameren et al., 2009[51].

tension was observed to increase, while the RAD51 fluorescence intensity decreased, consistent with RAD51 disassembling from the DNA (Figure 2.6). Remarkably, a sudden release of the tension resulted in an enhanced disassembly rate. This result was interpreted to indicate that not ATP hydrolysis is force dependent, but the actual detachment of a RAD51 monomer from the filament. Dissociation occurred in bursts interspersed with pauses comparable to the typical RAD51 catalyzed ATP hydrolysis time, providing support for a model in which RAD51 disassembly only takes place from filaments ends after ATP hydrolysis in the RAD51 monomer on the end.

Another DNA-binding protein that has been studied using optical tweezers and wide-field fluorescence microscopy is TFAM, a key protein in mitochondrial DNA transcription and compaction[52]. Fluorescence intensity measurements of dsDNA saturated with fluorescently labeled TFAM allowed determination of the footprint of the protein. The intensity of individual fluorescent spots observed at low TFAM concentrations indicated that TFAM binds as a monomer to dsDNA. These monomers diffused along the DNA and with single-molecule tracking the diffusion coefficient was determined. Force-extension measurements at different TFAM concentrations showed that TFAM binds to DNA in a cooperative way, decreasing the persistence
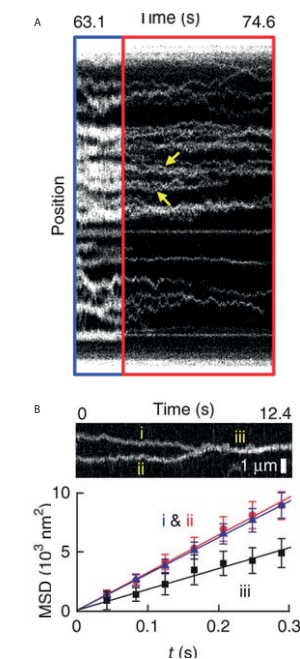
Figure 2.7: Imaging protein dynamics at high TFAM protein density, using STED high resolution microscopy. (A) Kymographs of TFAM–Atto 647N dynamics on λ DNA (F = 4 pN). Scale bars, 1 μm. the DNA is in reductive-oxidative system buffer, and at t = ~66 s, the STED beam is switched on at 6 mW (red borders; FWHM = 75 nm). Proteins that diffuse within diffraction-limited regions are indicated with arrows. (B) Top panel: a kymograph of a TFAM–Atto 647N oligomerization event. Bottom panel: the MSD analysis of trajectories i–iii as indicated in top panel (error bars: standard deviation; mean number of lines = 130). Adapted with permission from Heller et al., 2013[15].
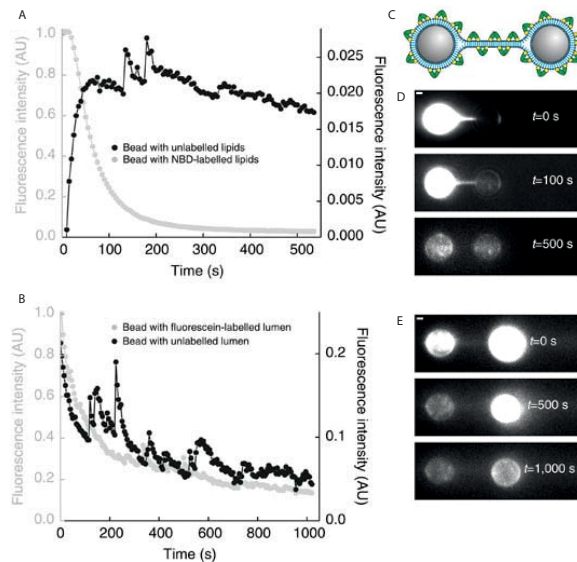
Figure 2.8: Investigation of lipid-protein interaction using dual-trap optical twee-zers combined with epi-illuminated wide-field fluorescence microscopy. (A) In the presence of fluorescent NBD-PE in a single membrane-coated bead, mem-brane-stalk formation was accompanied by a strong fluorescence increase in the unlabelled membrane and a concurrent decrease in the labelled membrane, indicative of either hemifusion or full membrane fusion. (B) To distinguish be-tween hemifusion and complete fusion, content mixing were tested by coating the beads with non-fluorescent PC/PS liposomes while one of the beads was loaded with fluorescein in the liposomal lumen. On a timescale of 1,000 s, fluo-rescence increase in the unlabelled bead or membrane stalk was not observed, indicative for hemifusion. (C) Schematic representation of the hemifused con-figuration with Doc2b bound to the membrane surface (D) Fluorescence images of bead pair in A at three different time points. Scale bar: 1 μm. (E) Fluorescence images of bead pair in B at three different time points. Scale bar: 1 μm. Adapted with permission from Brouwer et al., 2015[24].

length. In a follow-up study it was shown how compaction by TFAM blocks unwinding of duplex DNA resulting in inhibition of mitochondrial DNA tran-scription and replication[53].

To obtain even higher-resolution insights in TFAM diffusion and DNA binding, Heller et al. applied optical tweezers in combination with STED super-resolution microscopy[15]. The advantage of using STED was that TFAM could be studied at higher, more physiologically relevant, concentrations in solution and on the DNA. It was observed that TFAM monomers can cluster and form multimers, diffusing with a lower diffusion constant (Figure 2.7).

Lipid membrane fusion

Using a very different dual-trap optical tweezers assay, Brouwer et al. stud-ied lipid-protein interactions[24]. To this end, they coated the two trapped beads with lipid bilayers and repeatedly brought them together and separat-ed them. In the presence of Doc2b, a protein that is involved in SNARE-medi-ated membrane fusion during neurotransmitter-vesicle release, high rupture forces were observed. These high rupture forces indicated Doc2b-mediated membrane fusion. When the membranes were fused, fluorescently labelled lipids on one bead could diffuse to the other bead, while dyes in the lumen between membrane and bead did not, indicating that Doc2b mediates fusion of only outer leaflet of the lipid bilayer, known as hemifusion (Figure 2.8).

Cytoskeletal motor proteins

Dual-trap optical tweezers in combination with fluorescence microscopy has also been used to study the interaction of myosin motor proteins with filamentous actin. To this end, they attached myosin motors to a pedestal in their flow cell, while an actin filament was held between to optically trapped beads. Using this assay, interactions and force generation can be measured with the tweezers, while binding and release of fluorescent ATP analogues to the motor proteins can be followed with TIRF microscopy. With this ap-proach step sizes, processivity and ATPase activity of several myosin motors were characterized[54–59].

Bacterial motility

Min et al. and Mears et al. held a living bacterium fixed with two optical traps while flagellum position using fluorescence and cell-body displacement with the tweezers[60,61]. Fourier analysis of the cell-body displacements revealed two frequencies, one corresponding to rotation of the flagellum and the oth-er with the resulting rotation of the bacterium. The bacterial rotation signal contained indications of periods of constant, directional movement and tum-bling, consistent with two different kinds of appearances of the flagellum flu-orescence images[60]. Improvements in fluorescence imaging allowed Mears et al. to distinguish multiple flagella at the same time and determining their sense of rotation[61]. They demonstrated that only a single flagellum rotating clockwise was required to switch the bacterium into tumbling mode (Figure
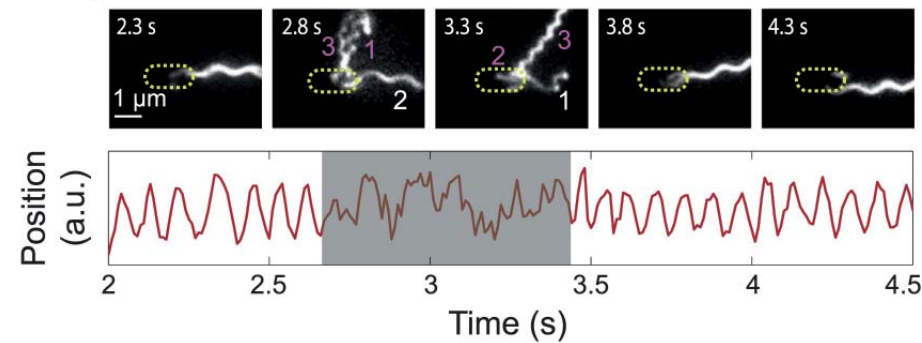
Figure 2.9: Assessment of bacterial motility. Top: Representative images from a trapped cell with three flagella. The approximate location of the unlabeled cell body is indicated by a dashed line. Flagella rotating CW (purple) and CCW (underlined-white) are numbered in frames in which they appear distinct. Bottom: corresponding cell-body rotation signal for the same cell as detected from deflections of the trapping laser. Tumbles (shaded area) were determined from the erratic cell-body rotation signal. Adapted with permission from Mears et al., 2014[61].

2.9). They also showed that flagella do not switch their sense of rotation independently (as was assumed before), but do that correlated, which has important implications for understanding bacterial motility and chemotaxis.

2.4.3   FRET studies with confocal fluorescence microscopy

Force measuring tools like atomic force microscopy or optical tweezers cannot detect small-scale conformational changes, unless a relatively strong force is applied. This limitation has been overcome by combining single-trap optical tweezers with FRET confocal microscopy, providing access to measurements of conformational dynamics. Hohng et al. used this approach to investigate the dynamics of Holiday Junction structures (HJ)[8]. A HJ is a four-stranded DNA structure that is an intermediate state during homologous recombination. The confocal beam was scanned to follow the motion of the molecule in response to the moving optical trap. By specifically labeling the HJ on different locations a 2D reaction landscape could be obtained, by probing the HJ dynamics in response to pulling forces in three different directions. In this way, global structural information could be obtained on transient species involved in HJ conformational changes.

The application of combined optical tweezers and FRET microscopy has been also extended to investigate DNA-protein interaction. For example,

Ngo et al.[62] employed single-trap optical tweezers and FRET microscopy to simultaneously manipulate an individual nucleosome under force and probe its local conformational changes. They anchored a DNA molecule with a nucleosome binding site with one end to a glass surface and with the other end to an optically trapped microsphere. The DNA contained FRET dye pairs at various locations. They found that the DNA, which is wrapped around the nucleosome, unwraps asymmetrically from a nucleosome: from one side unwrapping occurs at low forces (3–5 pN), while from the other side, substantially higher forces are required for unwrapping (12–15 pN). These results have important implications for chromosome remodelers, which move or expel nucleosomes from DNA.

In a different approach, Suksombat et al. studied the interaction of ssDNA binding protein, SSB with a short stretch (70 nucleotides) of ssDNA held between two optical traps with dsDNA handles[63]. Using a force clamp they observed step-wise length switches of the DNA tether, due to partial wrapping and unwrapping of the DNA around SSB (Figure 2.10). This switching
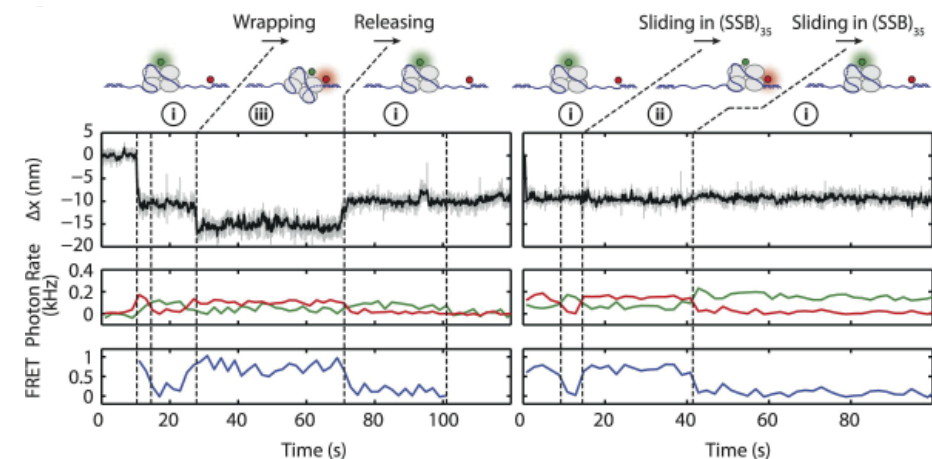
Figure 2.10: SSB binding modes and diffusion mechanism. Top: schematic of wrapping, releasing and sliding of fluorescently labelled SSB on ssDNA. Bottom: representative traces showing combined fluorescence and DNA extension measurements. Change in extension (top) and fluorescence (middle) of donor (SSBf) and acceptor (Cy5) are measured simultaneously. Together, FRET efficiency (bottom) and extension change (top) reveal the SSB wrapping states (i and ii, iii and iv) and their dynamics (ssDNA wrapping/releasing and sliding). Adapted with permission from Suksombat et al., 2015[63].

could also be observed using FRET between dyes on the DNA and SSB. They also observed changes in FRET efficiency uncorrelated to changes in DNA extension, indicative of SSB diffusing along the DNA.

With a similar assay, Comstock et al. studied UvrD helicase unwinding a DNA hairpin[12]. Changes in DNA extension revealed unwinding and rezipping of the DNA. Concomitant fluorescence measurements allowed discrimination of activity of UvrD monomers and dimers. For monomers frequent, repetitive switching between unwinding (of at most 20 bp) and rezipping were observed, while dimers processively unwound the DNA over lengths of 70 bp. FRET experiments showed that the conformation of the protein, open or closed, correlated to unwinding or rezipping activity.

Furthermore, the sub-nanometer sensitivity of FRET in measuring distances, together with piconewton force sensitivity of optical tweezers enables studies of mechanotransduction. With the help of this capability, Brenner et al. used this combination to determine how spider-silk flagelliform repeat peptides react to force[64]. They first showed that, at zero force, each peptide has a conformation stable on the time scale of one second to minutes. Next, they showed, by measuring FRET efficiency as a function of force, that the peptides behave as linear springs. This was unexpected since disordered proteins act as nonlinear springs. The results indicate that these peptides are highly compact and in an ordered, rod-like coil structure. Brenner et al. also used these peptides as intracellular force sensors, by integrating them in the focal-adhesion protein vinculin and measuring FRET using fluorescence lifetime imaging.

2.5   Conclusion

The state-of-the-art combination of optical tweezers with fluorescence microscopy and microfluidics techniques provides a valuable addition to the single-molecule toolkit. It has enabled scientists to study biological systems with previously unobtainable precision and clarity on a vast number of different biological interactions as illustrated in this chapter. Some of the most recent advancements such as STED microscopy promise to give rise to even more exciting new possibilities by pushing the experimental limits towards single-molecule experiments in conditions closer to the physiological reality. Moreover, the current state of maturity of the technology and the concurrent development of their application in biological assays, as is reviewed in this chapter, paves the road for broadening the application of this combined technique from the realm of fundamental research in a specialized biophysics laboratory to biochemical, biological and pharmaceutical laboratories. Finally, commercial solutions are becoming increasingly available, which makes this powerful combined approach accessible to a broad range of researchers from different backgrounds. When this technology spreads we expect to see more innovative and exciting single-molecule experiments which can revolutionize research in biophysics, biochemistry, drug discovery, toxicology and many other fields.

Disclosure
GW and EP are co-founders and have financial interested in LUMICKS B.V.

References

1. Ashkin, A., Dziedzic, J. & Yamane, T. Optical trapping and manipulation of single cells using infrared laser beams. Nature 330, 769–771 (1987).
2. Chu, S. Laser manipulation of atoms and particles. 861–866 (1991).
3. Bianco, P. R. et al. Processive translocation and DNA unwinding by individual RecBCD enzyme molecules. Nature 409, 374–378 (2001).
4. Funatsu, T. et al. Imaging and nano-manipulation of single biomolecules. Biophys. Chem. 68, 63–72 (1997).
5. Sarangapani, K. K. et al. Sister kinetochores are mechanically fused during meiosis I in yeast. Science (80-.). 346, (2014).
6. Arai, Y. et al. Tying a molecular knot with optical tweezers. Nature 399, 446–8 (1999).
7. Saito, K., Aoki, T. & Yanagida, T. Movement of Single Myosin Filaments and Myosin Step Size on an Actin Filament Suspended in Solution by a Laser Trap. Biophys. J. 66, 769–777 (1994).
8. Hohng, S. et al. Fluorescence-force spectroscopy maps two-dimensional reaction landscape of the holliday junction. Science (80-.). 318, 279–283 (2007).
9. Grashoff, C. et al. Measuring mechanical tension across vinculin reveals regulation of focal adhesion dynamics. Nature 466, 263–266 (2010).
10. Bornschlögl, T., Romero, S., Vestergaard, C. L. & Joanny, J. Filopodial retraction force is generated by cortical actin dynamics and controlled by reversible tethering at the tip. PNAS 110, 18928–18933 (2013).
11. Zhou, R. et al. SSB Functions as a Sliding Platform that Migrates on DNA via Reptation. Cell 146, 222–232 (2011).
12. Comstock, M. J. et al. Direct observation of structure-function relationship in a nucleic acid–processing enzyme. Science (80-.). 348, 352–354 (2015).
13. Duesterberg, V. K. et al. Observation of long-range tertiary interactions during ligand binding by the TPP riboswitch aptamer. Elife 1–17 (2015).
14. Wolfson, D. et al. Rapid 3D fluorescence imaging of individual optically trapped living immune cells. J. Biophotonics 8, 208–216 (2015).
15. Heller, I. et al. STED nanoscopy combined with optical tweezers reveals protein dynamics on densely covered DNA. Nat. Methods 10, 910–6 (2013).
16. Eriksson, E. et al. A microfluidic system in combination with optical tweezers for analyzing rapid and reversible cytological alterations in single cells upon environmental changes. Lab Chip 7, 71–76 (2007).
17. Pang, Y., Song, H., Kim, J. H., Ximiao, H. & Cheng, W. Optical Trapping of Individual Human Immunodeficiency Viruses in Culture Fluid Reveals Heterogeneity with Single-Molecule Resolution. Nat. Nanotechnol 9, 624–630 (2014).
18. Podlipec, R. & Strancar, J. Cell-scaffold adhesion dynamics measured in first seconds predicts cell growth on days scale - Optical tweezers study. ACS Appl. Mater. Interfaces 7, 6782–6791 (2015).
19. Tam, J. M. et al. Control and Manipulation of Pathogens with an Optical Trap for Live Cell Imaging of Intercellular Interactions. PLoS One 5, (2010).
20. Kyrsting, A., Bendix, P. M., Stamou, D. G. & Oddershede, L. B. Heat Profiling of Three-Dimensionally Optically Trapped Gold. 888–892 (2011).
21. Bendix, P. M. & Oddershede, L. B. Expanding the Optical Trapping Range of Lipid Vesicles to the. Nano Lett. 11, 5431–5437 (2011).
22. Bendix, P. M., Reihani, S. N. S. & Oddershede, L. B. Direct measurements of heating by electromagnetically trapped gold nanoparticles on supported lipid bilayers. ACS Nano 4, 2256–2262 (2010).
23. Prévost, C. et al. IRSp53 senses negative membrane curvature and phase separates along membrane tubules. Nat. Commun. 6, 8529 (2015).
24. Brouwer, I. et al. Direct quantitative detection of Doc2b-induced hemifusion in optically trapped membranes. Nat. Commun. 6, 1–8 (2015).
25. Leijnse, N., Oddershede, L. B. & Bendix, P. M. Helical buckling of actin inside filopodia generates traction. PNAS 112, 135–141 (2015).
26. Gross, P., Farge, G., Peterman, E. J. G. & Wuite, G. J. L. Combining Optical Tweezers, Single-Molecule Fluorescence Microscopy, and Microfluidics for Studies of DNA-Protein Interactions. Methods in Enzymology vol. 475 427–453 (Elsevier Inc., 2010).
27. Moffitt, J., Chemla, Y., Smith, S. & Bustamante, C. Recent advances in optical tweezers. Annu. Rev. Biochem. 77, 205–228 (2008).
28. Neuman, K. C. & Block, S. M. Optical trapping. Rev. Sci. Instrum. 75, 2787–2809 (2004).
29. Heller, I. et al. Mobility analysis of super-resolved proteins on optically stretched DNA: Comparing imaging techniques and parameters. ChemPhysChem 15, 727–733 (2014).
30. Handa, N., Bianco, P. R., Baskin, R. J. & Kowalczykowski, S. C. Direct Visualization of RecBCD Movement Reveals Cotranslocation of the RecD Motor after X Recognition. Mol. Cell 17, 745–750 (2005).
31. Bianco, P. R., Bradfield, J. J., Castanza, L. R. & Donnelly, A. N. Rad54 Oligomers Translocate and Cross-bridge Double-stranded DNA to Stimulate Synapsis. J. Mol. Biol. 374, 618–640 (2007).
32. Hilario, J., Amitani, I., Baskin, R. J. & Kowalczykowski, S. C. Direct imaging of human Rad51 nucleoprotein dynamics on individual DNA molecules. PNAS 106, 361–368 (2009).
33. Akiyoshi, B. et al. Tension directly stabilizes reconstituted kinetochore-microtubule attachments. Nature 468, 576–579 (2010).
34. Umbreit, N. T. et al. Kinetochores require oligomerization of Dam1 complex to maintain microtubule attachments against tension and promote biorientation. Nat. Commun. 5, (2014).
35. Kudalkar, E. M. et al. Regulation of outer kinetochore Ndc80 complex-based microtubule attachments by the central kinetochore Mis12 / MIND complex. PNAS 112, (2015).
36. Lee, K. S., Balci, H., Jia, H., Lohman, T. M. & Ha, T. Direct imaging of single UvrD helicase dynamics on long single-stranded DNA. Nat. Commun. 4, 1878 (2013).
37. Beebe, D. J., Mensing, G. a & Walker, G. M. Physics and applications of microfluidics in biology. Annu. Rev. Biomed. Eng. 4, 261–286 (2002).
38. Squires, T. M. Microfluidics Fluid physics at the nanoliter. Rev. Mod. Phys. 77, 977–1026 (2005).
39. Bao, X. R., Lee, H. J. & Quake, S. R. Behavior of Complex Knots in Single DNA Molecules. Phys. Rev. Lett. 91, 1–4 (2003).
40. Smith, S. B., Cui, Y. & Bustamante, C. Overstretching B-DNA: The Elastic Response of Individual Double-Stranded and Single-Stranded DNA Molecules. Science (80-.). 271, 795–799 (1996).
41. Gross, P. et al. Quantifying how DNA stretches, melts and changes twist under tension. Nat. Phys. 1–6 (2011) doi:10.1038/nphys2002.
42. King, G. A., Peterman, E. J. G. & Wuite, G. J. L. Unravelling the structural plasticity of stretched DNA under torsional constraint. Nat. Commun. 7, 1–7 (2016).
43. Le, S., Liu, R., Lim, C. T. & Yan, J. Uncovering mechanosensing mechanisms at the single protein level using magnetic tweezers. Methods 94, 13–18 (2016).
44. van Mameren, J. et al. Unraveling the structure of DNA during overstretching by using multicolor , single-molecule fluorescence imaging. PNAS 106, 18231–18236 (2009).
45. King, G. A., Gross, P., Bockelmann, U., Modesti, M. & Wuite, G. J. L. Revealing the competition between peeled ssDNA , melting bubbles , and S-DNA during DNA overstretching using fluorescence microscopy. PNAS 110, 3859–3864 (2013).

2

46. Léger, J. et al. Structural Transitions of a Twisted and Stretched DNA Molecule. Phys. Rev. Lett. 83, 1066–1069 (1999).

47. Murade, C. U., Subramaniam, V., Otto, C. & Bennink, M. L. Interaction of Oxazole Yellow Dyes with DNA Studied with Hybrid Optical Tweezers and Fluorescence Microscopy. Biophys. J. 97, 835–843 (2009).

48. Biebricher, A. S. et al. The impact of DNA intercalators on DNA and DNA-processing enzymes elucidated through force-dependent binding kinetics. Nat. Commun. 6, 1–12 (2015).

49. van Mameren, J. et al. Dissecting Elastic Heterogeneity along DNA Molecules Coated Partly with Rad51 Using Concurrent Fluorescence Microscopy and Optical Tweezers. Biophys. J. 91, L78–L80 (2006).

50. Candelli, A. et al. Visualization and quantification of nascent RAD51 filament formation at single-monomer resolution. PNAS 111, 15090–5 (2014).

51. van Mameren, J. et al. Counting RAD51 proteins disassembling from nucleoprotein filaments under tension. Nature 457, 745–748 (2009).

52. Farge, G. et al. Protein sliding and DNA denaturation are essential for DNA organization by human mitochondrial transcription factor A. Nat. Commun. (2012) doi:10.1038/ncomms2001.

53. Farge, G. et al. In vitro-reconstituted nucleoids can block mitochondrial DNA replication and transcription. Cell Rep. 8, 66–74 (2014).

54. Ishijima, A. et al. Simultaneous Observation of Individual ATPase and Mechanical Events by a Single Myosin Molecule during Interaction with Actin. Cell 92, 161–171 (1998).

55. Tanaka, H., Ishijima, A., Honda, M., Saito, K. & Yanagida, T. Orientation Dependence of Displacements by a Single One-Headed Myosin Relative to the Actin Filament. Biophys. J. 75, 1886–1894 (1998).

56. Watanabe, T. M. et al. A one-headed class V myosin molecule develops multiple large ($\approx$ 32-nm) steps successively. PNAS 101, 1–6 (2004).

57. Iwane, A. H., Tanaka, H., Morimoto, S., Ishijima, A. & Yanagida, T. The Neck Domain of Myosin II Primarily Regulates the Actomyosin Kinetics , not the Stepsize. J. Mol. Biol. 353, 213–221 (2005).

58. Tanaka, H., Homma, K., White, H. D., Yanagida, T. & Ikebe, M. Smooth muscle myosin phosphorylated at single head shows sustained mechanical activity. J. Biol. Chem. 283, 15611–15618 (2008).

59. Komori, T., Nishikawa, S., Ariga, T., Iwane, A. H. & Yanagida, T. Simultaneous Measurement of Nucleotide Occupancy and Mechanical Displacement in Myosin-V , a Processive Molecular Motor. Biophys. J. 96, L4–L6 (2009).

60. Min, T. L. et al. High-resolution, long-term characterization of bacterial motility using optical tweezers. Nat. Methods 6, 831–835 (2009).

61. Mears, P. J., Koirala, S., Rao, C. V, Golding, I. & Chemla, Y. R. Escherichia coli swimming is robust against variations in flagellar number. Elife 1–18 (2014) doi:10.7554/eLife.01916.

62. Ngo, T. T. M., Zhang, Q., Zhou, R., Yodh, J. G. & Ha, T. Asymmetric Unwrapping of Nucleosomes under Tension Directed by DNA Local Flexibility. Cell 160, 1135–1144 (2015).

63. Suksombat, S., Khafizov, R., Kozlov, A. G., Lohman, T. M. & Chemla, Y. R. Structural dynamics of E. Coli singlestranded DNA binding protein reveal DNA wrapping and unwrapping pathways. Elife 4, 1–23 (2015).

64. Brenner, M. D., Zhou, R., Conway, D. E., Lanzano, L. & Gratton, E. Spider Silk Peptide Is a Compact, Linear Nanospring Ideal for Intracellular Tension Sensing. Nano Lett. 16, 2096–2102 (2016).

65. Rasmussen, M. B., Oddershede, L. B. & Siegumfeldt, H. Optical Tweezers Cause Physiological Damage to Escherichia coli and Listeria Bacteria. Appl. Environ. Microbiol. 74, 2441–2446 (2008).

66. Galletto, R., Amitani, I., Baskin, R. J. & Kowalczykowski, S. C. Direct observation of individual RecA filaments assembling on single DNA molecules. Nature 443, 875–878 (2006).

67. Pezza, R. J., Camerini-otero, R. D. & Bianco, P. R. Hop2-Mnd1 Condenses DNA to Stimulate the Synapsis Phase of DNA Strand Exchange. Biophysj 99, 3763–3772 (2010).

68. van Den Broek, B. et al. Visualizing the Formation and Collapse of DNA Toroids. Biophysj 98, 1902–1910 (2010).

69. Ali, M. Y., Homma, K., Iwane, H., Adachi, K. & Itoh, H. Unconstrained Steps of Myosin VI Appear Longest among Known Molecular Motors. Biophys. J. 86, 3804–3810 (2004).

70. Dong, J., Castro, C. E., Boyce, M. C., Lang, M. J. & Lindquist, S. Optical trapping with high forces reveals unexpected behaviors of prion fibrils. Nat. Struct. Mol. Biol. 17, 1422–1430 (2010).

71. Ferrer, J. M., Fangyuan, D., Brau, R. R., Tarsa, P. B. & Lang, M. J. IOFF Generally Extends Fluorophore Longevity in the Presence of an Op- tical Trap. Curr. Pharm. Biotechnol. 502–507 (2010).

72. Iwaki, M., Hikikoshi, A., Ikebe, M. & Yanagida, T. Biased Brownian motion mechanism for processivity and directionality of single-headed myosin-VI. BioSystems 93, 39–47 (2008).

73. Iwaki, M., Tanaka, H., Iwane, H., Katayama, E. & Ikebe, M. Cargo-Binding Makes a Wild-Type Single-Headed Myosin-VI Move Processively. Biophys. J. 90, 3643–3652 (2006).

74. Lee, K. S. et al. Ultrafast Redistribution of E . coli SSB along Long Single-Stranded DNA via Intersegment Transfer. J. Mol. Biol. 426, 2413–2421 (2014).

75. Ngo, T. T. M. et al. Effects of cytosine modifications on DNA flexibility and nucleosome mechanical stability. Nat. Commun. 7, 1–9 (2016).

76. Sarangapani, K. K. et al. Supplementary Materials for. (2014)

77. Tarsa, P. B. et al. Detecting Force-Induced Molecular Transitions with Fluorescence Resonant Energy Transfer. Angew. Chemie 46, 1999–2001 (2007).

78. Biebricher, A. et al. Article PICH : A DNA Translocase Specially Adapted for Processing Anaphase Bridge DNA. Mol. Cell 51, 691–701 (2013).

79. Landry, M. P., Mccall, P. M., Qi, Z. & Chemla, Y. R. Characterization of Photoactivated Singlet Oxygen Damage in Single-Molecule Optical Trap Experiments. Biophysj 97, 2128–2136 (2009).

80. Harada, Y., Funatsu, T., Murakami, K., Nonoyama, Y. & Ishihara, A. Single-Molecule Imaging of RNA Polymerase-DNA Interactions in Real Time. Biophys. J. 76, 709–715 (1999).

81. Eriksson, E. et al. A microfluidic device for reversible environmental changes around single cells using optical tweezers for cell selection and positioning. Lab Chip 10, 617–625 (2010).

82. Inman, J. T. et al. DNA y structure: A versatile, multidimensional single molecule assay. Nano Lett. 14, 6475–6480 (2014).

83. Mirsaidov, U. et al. Live cell lithography : Using optical tweezers to create synthetic tissue. Lab Chip 8, 2174–2181 (2008).

84. Sasuga, Y. et al. Development of a microscopic platform for real-time monitoring of biomolecular interactions. Genome Res. 16, 132–139 (2006).

85. Yogo, K. et al. Direct Observation of Strand Passage by DNA- Topoisomerase and Its Limited Processivity. PLoS One 7, 1–7 (2012).

Implementation of 3D multi-color fluorescence microscopy in a quadruple trap optical tweezers system

Submitted for publication: A.E.C. Meijering*, J.A.M. Bakx*, T. Man, I. Heller, G.J.L. Wuite, E.J.G. Peterman
*These authors contributed equally

3.1 Abstract

Recent advances in the design and measurement capabilities of optical tweezers instruments, and especially the combination with multi-color fluorescence detection, have accommodated a dramatic increase in the versatility of optical trapping. Quadruple (Q)-trap optical tweezers are an excellent example of such an advance, by providing three-dimensional control over two constructs and thereby enabling for example DNA-DNA braiding. However, the implementation of fluorescence detection in such a Q-trapping system poses several challenges: i) since typical samples span a distance in the order of tens of micrometers, it requires imaging of a large field of view, ii) in order to capture fast molecular dynamics, fast imaging with single-molecule sensitivity is desired, iii) in order to study three-dimensional objects it could be needed to detect emission light at different axial heights while keeping the objective lens and thus the optically trapped microspheres in a fixed position. In this chapter, we describe design guidelines for a fluorescence imaging module on a Q-trap system that overcomes these challenges and provide a step-by-step description for construction and alignment of such a system. Finally, we present detailed instructions for proof-of-concept experiments that can be used to validate and highlight the instruments capabilities.

3.2 Introduction

The utilization of optical tweezers to probe single-molecule interactions has dramatically increased in the past decades. The variety of experiments that is currently performed covers a wide spectrum from studies of elementary structures like DNA, RNA, lipid membrane tethers or polypeptides to complex structures like whole cells[1]. At the same time, the complexity of the optical tweezers systems themselves – from a single trap to dual trap, implementation with microfluidics and combinations with different types of fluorescence imaging modules – has increased likewise, thereby accommodating for ever more sophisticated experiments[2].

While dual-trap optical tweezers are excellent for manipulation in a single dimension, more complex three-dimensional molecular architectures can now be manipulated and probed using quadruple trap optical tweezers systems (Q-trap). A Q-trap allows the user to move four traps in three dimensions, which permits, for example, manipulating, orienting and interacting two independent structures such as two DNA molecules. Moreover, the combination with fluorescence microscopy allows for direct visualization of interactions within and/or between the manipulated structure(s) and/or with their environment. This configuration allowed Brouwer et al. (2016) to study how the proteins XLF and XRCC4 hold together the blunt ends of two DNA molecules, thereby shedding light on the function of these enzymes in the process of non-homologous end joining[3]. In another study, the Q-trap configuration was used to study the ability to bridge two DNA molecules by the protein complex cohesin, which is known to play a role in prevention of premature chromosome segregation during cell division[4]. In a final example, King et al. (2018) developed a method to determine the local forces on the four arms of two interlinked double stranded (ds) DNA molecules using force-sensitive DNA intercalators[5]. In these assays, the ability to apply and monitor forces combined with direct visualization of fluorescently labeled probes, proved to be crucial to understand the system under scrutiny. Fluorescence microscopy in these cases provided information on substrate location and binding kinetics that was not accessible with force measurements alone.

This chapter expands on previous descriptions of how to build a Q-trap setup[6] by providing detailed instructions on the implementation of fluorescence microscopy in such system. The design of an imaging module in a

Q-trap yields several challenges that have to be overcome: First, the three-dimensional nature of Q-trapping-experiments requires that 3D volumes can be imaged while retaining the ability to capture fast molecular dynamics. Generally, two types of fluorescence imaging are combined with optical tweezers: confocal or wide-field fluorescence microscopy [1]. Confocal microscopy benefits from a reduced background fluorescence signal and can be combined with super-resolution imaging techniques like STED [7]. However, the need to scan the confocal focus over the field of view can make it slow, which might compromise the ability to study dynamic processes, especially when 3D scanning would be required. While wide-field fluorescence imaging does not benefit from the same reduction of out-of-focus fluorescence signal as confocal fluorescence does, it exhibits an advantageously fast imaging rate. Second, to study the interactions between several biomolecules it is advantageous to image multiple fluorescent substrates simultaneously with single-molecule resolution. This requires multi-color excitation and subsequent wavelength-based separation of emission light, before projecting it on separate regions of a camera chip. Finally, the ability to move the traps in 3D poses another challenge for the fluorescence detection. Since the sample is decoupled from the sample stage and the objective lens is used to keep the sample in a fixed position, the objective lens cannot be used to image different planes of the sample. Therefore, a solution has to be implemented that enables movement of the fluorescent imaging plane with respect to the sample, either by moving the axial trap position or by translation of the fluorescent detection plane. Since axial movement of the traps would induce extra noise, the latter solution is favored.

In this chapter we provide a detailed description on how to implement 3D multi-color wide-field fluorescence imaging in an existing Q-trap optical tweezers setup and we provide a step-by-step guide of two example experiments that can be used to validate and display these imaging capabilities and that can be used as a starting point for a plethora of more complex experiments that are not limited to studies of DNA-protein interactions.

3.3   Materials

3.3.1   Quadruple-trap optical tweezers

A wide variety of optical tweezers systems can be found among laboratories and excellent discussions of choices in system design have been written before [6,8]. Therefore, we will not provide detailed instructions on optical tweezers construction here, but rather briefly describe the custom-built quadruple-trap optical tweezers setup in our laboratory and highlight the important aspects that affect the design of the fluorescence microscopy implementation.

3.3.1.1   Optical trap steering- and force detection unit

1.   Microscope body (Nikon, model TE2000-u)
2.   60x Water immersion objective (Nikon, Plan apo VC NA1.2)
3.   Condenser top lens (Leica, P 1.40 OIL S1 11551004)
4.   1064 nm 20 W CW trapping laser (IPG Photonics, YLR-20-LP)
5.   980 nm 300 mW CW detection laser (CLD1015, TS1939643-PM980-XP Thorlabs)
6.   Closed loop piezo mirror, 10 mrad range (MadCityLabs, NanoMTA2X10) (see **Note 1** and **Note 3**)
7.   PSD (Silicon Sensor International AG, DL100-7PCBA3).

Like many custom-built optical tweezers setups, our system is designed around an inverted microscope body as depicted in Figure 3.1. The microscope is placed centrally on the optical table surrounded by four functional units of which two belong to the optical tweezers system. The trapping light is focused inside the flow chamber (FC) via a 60x water immersion objective lens (OL) and collected using an oil immersion condenser lens (CL). The microscope is fitted with two filter cube selection turrets of which the upper one is used to couple the trapping light into the objective and the lower one is used to couple in fluorescence excitation light.

In order to create four optical traps with independent position control, a single linearly polarized 1064 nm laser beam is split into four separate beams. This is achieved by first splitting the beam into two using a beam-splitter cube (PB1, Figure 3.1), and subsequently into four using another two
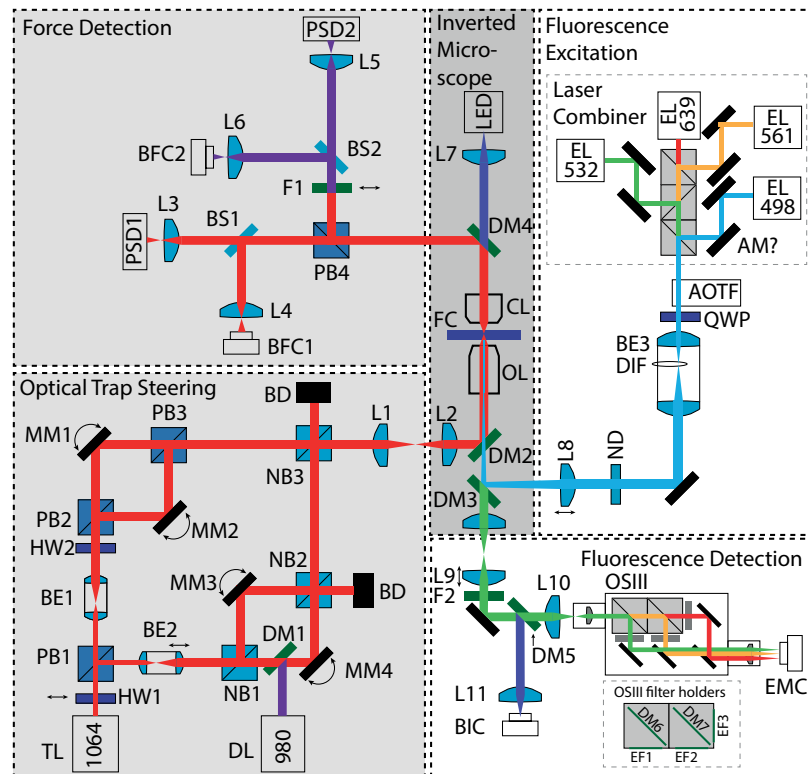
Figure 3.1: Schematic overview of a Quadruple trap optical tweezers instrument combined with multi-color wide field fluorescence. Four functional units are built around a commercial inverted microscope body: optical trap steering, force detection, fluorescence excitation and fluorescence detection. The optical trap steering is performed by creating four beams from the light of the trapping laser (TL) using polarizing beam splitters (PB1-3) and a non-polarizing beam splitter (NB1-3) cubes. Each trap is steered by its own motorized mirror (MM1-4) and the relative axial position of trap 3 and 4 with respect to trap 1 and 2 can be changed by displacement of beam expander BE2. The 980-nm detection laser (DL) is co-aligned with trap 4 to allow force detection on this trap based on wavelength. After passing through the objective lens (OL) and the condenser lens (CL) the trapping light of trap 1 is imaged on position sensitive diode PSD1 and back focal plane camera BFC1, while the detection laser light is imaged onto PSD2 and BFC2. A point source LED is used to illuminate the sample plane, which is imaged onto a bead imaging camera (BIC). Wide field fluorescence excitation is achieved by co-aligning the beams of four excitation lasers (EL498,532,561 and 639). An acousto-optic tunable filter (AOTF) is used to modulate the individual excitation intensities. In the focus of beam expander BE3, a diffuser (DIF) is placed to reduce speckle issues. The emission light is collected by the objective lens and passes through lens L9, which is mounted on a motorized stage and is used to select the imaging plane that will be projected onto the EMCCD camera (EMC). An Optosplit (OSIII) with dichroic mirrors (DM6 and 7) and emission filters (EF1-3) is used to separate the emission light based on wavelength and to project the different wavelengths on different areas of the camera. Other optics in the figure: BD beam dump, BS beam splitter, F filter, FC flow cell, ND neutral density filter, QWP quarter-wave plate. Figure is adapted from Heller et al. [6].

beam-splitter cubes (PB2 and NB1, Figure 3.1). Each of the four beams is reflected by a steering mirror (MM1-4, Figure 3.1) and are recombined into the same optical path using three beam-splitter cubes (PB3 and NB2 and 3, Figure 3.1). By using a combination of polarizing and non-polarizing beam-splitter cubes, the splitting of the source beam results in four separate beams of which one has a unique orthogonal polarization (trap 1, MM1, Figure 3.1) with respect to the other three (trap 2-4). This splitting scheme facilitates straightforward force detection on trap 1 due to its unique polarization. For force detection on one of the traps that lack a unique polarization, an additional low-power 980 nm laser beam is used that can be separated based on wavelength instead of on polarization. In our scheme, the 980 nm laser is co-aligned with trap 4 (DM1, Figure 3.1).

The use of two non-polarizing beam-splitter cubes (NB2 and NB3, Figure 3.1) in the steering unit of the optical tweezers system results in a significant loss of the original laser power. Therefore, our setup contains a relatively high power 20 W 1064 nm fiber laser, leading to maximally 1.7 W per optical trap when equally distributed. In order to control the relative power of the different beams, two half-wave plates (HW1 and HW2) are incorporated. Alternatively, by flipping the first half-wave plate (HW1) out of the path, all laser light can be directed to trap 1 and trap 2, transforming the setup to dual-trap optical tweezers configuration.

Two beam expanders (BE1 and BE2, Figure 3.1) are used to expand the beam, such that overfilling of the back aperture of the objective lens (OL, Figure 3.1) is achieved, which is required to achieve high trapping stiffness. One of the lenses of beam expander 2 is positioned on a linear translation stage. By moving the lens, small deviations of the beam's collimation will result in a change in the focal position of the optical trap. As such, moving the lens of the beam expander can be used to simultaneously move the position of trap 3 and 4 axially with respect to trap 1 and 2. This extra functionality enables complicated experimental procedures such as wrapping of DNA molecules around one another. When the optical traps are at different axial locations, the manipulated object(s) can no longer be imaged within a single focal plane. To nevertheless enable concurrent fluorescence imaging, the fluorescence module is designed with the capability to perform image acquisition in three dimensions. Finally, to enable lateral trap positioning, the steering mirrors (MM1-4) are imaged onto the back focal plane (or back pu-

pil) of the objective using a 1:1 telescope that consists of two identical lenses in a 4f configuration (L1-2, Figure 3.1).

The light beams of the trapping laser and the detection laser pass through the flow cell and condenser lens and are then split based on polarization using a polarizing beam-splitter cube (PB4), thereby isolating the laser light of trap 1 from the light of the other traps. In the other path, the laser light of the detection laser is separated from the trapping laser light using a band-pass filter (F1, Figure 3.1) to isolate the 980-nm light. The light of trap 1 and the 980-nm light of trap 4 are imaged onto two position sensitive diodes (PSD's) (PSD1 and 2, Figure 3.1) for force detection and onto two back focal plane cameras (BFC1-2, Figure 3.1), which can be used as diagnostic tools to determine e.g. the number of beads trapped and the presence of air bubbles in the oil of the condenser lens [9].

3.3.1.2 Microfluidics

The microfluidic system (uFlux, available from LUMICKS B.V.) provides control over the flow of up to six separate buffer solutions that are connected by tubing to a flow cell. Here, pressure-driven flow is controlled using a single pressure chamber and the flow of each buffer solution can be turned on or off using independent valves. All channels are combined into one outlet channel. The flow cell is placed on a moveable stage such that optically trapped objects can be transferred between parallel laminar buffer flows, which enables fast buffer exchange. A detailed description and illustration of the flow system has been published previously [10].

3.3.1.3 Custom-written LabVIEW software

Custom-written LabVIEW software is used to:

- Perform real-time bead tracking of microspheres (via LED wide-field imaging) using a template-matching algorithm resulting in a position and distance measurement up to a frequency of 150 Hz.
- Perform force calibration using the power spectrum of the bead displacements measured by the PSDs, enabling real-time force measurement up to a frequency of 50 kHz.
- Apply pressure to the pressurized air flow system in order to control the flow through the flow cell.
- Control the x and y-position of the flow-cell with respect to the traps in order to move in between several laminar flow channels.

- Move the traps in x, y and z-direction while monitoring bead position and force.

3.3.2 Epi fluorescence excitation

The fluorescence excitation is coupled into the microscope via the lower back entrance of the microscope body with a lens (L10, Figure 3.1), via the filter cube of the lower turret, focusing on the back focal plane of the objective. Depending on the combination of excitation wavelength different dichroic mirrors can be mounted in the lower turret of the microscope.

3.3.2.1 Laser combiner

- Cobolt 06-MLD 488 nm, 100 mW
- Cobolt 06-DPL 532 nm, 100 mW
- Cobolt 06-DPL 561 nm, 100 mW
- Cobolt 06-MLD 638 nm, 140 mW
- Dichroic mirrors to combine laser beams (LM01-503, LM01-552, LM01-613, Semrock) (see **Note 2**).
- Acousto-optic tunable filter (AOTF, A.A. Opto-Electronic) for color wavelength selection and power control (see **Note 3**).
- Neutral density (ND) filter wheel (see **Note 4**)
- Dichroic mirror inside microscope (Di03-R405/488/561/635 or Di03-R405/488/532/635 depending on the combination of lasers used, Semrock) for excitation light reflection and emission light transmission.

3.3.2.2 Beam expander and diffuser

- 10x beam expander (see **Note 5**)
- Rotating ground glass diffuser (Suss microoptics, system nr:24-00009) (see **Note 6**)

3.3.3 Fluorescence detection

- Short-pass filter to block trapping light: FF01-842/SP-25 (see **Note 7**)
- Relay lenses (see subheading 3.4.2.2 for a calculation of the focal length)
- Physik Instrumente Q-521.230 miniature linear stage
- Cairn Optosplit III
- Two filter sets for the Optosplit:
    Filter set for excitation with 488, 532 and 638 nm lasers

- FF538-FDi02 (Semrock)
- FF01-509/22-25 (Semrock)
- FF640-FDi02 (Semrock)
- FF01-575/59-25 (Semrock)
- FF01-680/42-25 (Semrock)

  Filter set for excitation with 488, 561 and 638 nm lasers
- FF560-FDi02 (Semrock)
- FF01-525/45-25 (Semrock)
- FF640-FDi02 (Semrock)
- FF01-600/52-25 (Semrock)
- FF01-698/70-25 (Semrock)
- Andor Ixon 897 Life EMCCD camera
- Software: µManager

3.3.4   Bright-field imaging
- Dichroic mirror to split LED light from emission light (FF484-FDi01, Semrock)
- Lens (see subheading 3.4.2.2 for a calculation of the focal length)
- CMOS camera (DCC1645C, Thorlabs)

3.3.5   Buffer solutions

3.3.5.1   Bleach cleaning solutions (see subheading 3.4.4.1)
- MilliQ water
- Bleach solution - 0.7 M NaClO
- Sodium thiosulfate solution - 10 mM $Na_2S_2O_3$

3.3.5.2   Solutions for passivation of the flow cell (see subheading 3.4.4.2) (see **Note 8**)
- Phosphate buffered Saline (PBS) (in tablets available from Invitrogen)
- 1% w/v Bovine serum albumin (BSA) (available from Sigma-Aldrich) in PBS
- 5% w/v Pluronic® F127 (available from Sigma-Aldrich) in PBS

3.3.5.3   Buffer solutions for the assays (see subheading 3.4.5 and 3.4.6)
- PBS

- Bead solution: Streptavidin coated polystyrene beads with a diameter of 1-5 µm (Spherotech) are diluted in PBS
- DNA solution: Lambda phage DNA constructs with biotinylated nucleotides on each end of the molecule are diluted to obtain tens of picomolar concentration in PBS [11].
- Intercalator YOYO-1 (YOYO, Invitrogen): 5 nM YOYO, 5% Pluronic® F127 in PBS.
- Intercalator SytoxOrange (SxO, Invitrogen): 20 nm SxO, 5% Pluronic® F127 in PBS.

3.4   Methods

3.4.1   Fluorescence excitation design and alignment
Multi-color wide-field fluorescence excitation is achieved by focusing several co-aligned laser beams on the back focal plane of the imaging objective, such that a collimated illumination beam for homogenous excitation is achieved in the sample plane. The design of the excitation path concerns three critical components: the laser source(s), the possible incorporation of an acousto-optic tunable filter (AOTF) and the (amount of) beam expansion. These three key elements together determine the homogeneity of the illumination intensity by the excitation beams, which is of importance for single-molecule sensitivity over the field of view. In the next sections, we give a detailed discussion of several aspects and considerations that underlie the design of the excitation path.

3.4.1.1   Choice of beam expansion
The collimated excitation beam has a Gaussian beam profile, which will result in an excitation intensity distribution that peaks in the center of the field of view and drops off toward the edges. To obtain an intensity distribution that is as homogeneous as desirable, (which benefits uncomplicated quantitative analysis of fluorescence intensity, see **Note 9**), the excitation beam diameter is typically expanded before it enters the microscope. However, such beam expansion goes hand in hand with a loss of excitation intensity, which may hamper the possibly of single-fluorophore detection. The choice of beam expansion is therefore a trade-off between (single-molecule) sensitivity and

homogeneous illumination over a wide field of view. The following calculation steps can be performed in order to determine the preferred beam expansion.

1. Determine the size of the construct that will be used for trapping experiments (L) (see **Note 10**).
2. Decide which factor difference in illumination intensity between the maximum and the edges of your object is acceptable (p) (see **Note 11**).
3. Calculate the desired beam diameter (D) at the illumination plane for a Gaussian beam profile by solving $\exp\left(\frac{-\frac{1}{8}L^2}{D_{imagingplane}^2}\right) = 1 - p$.
4. Calculate the beam diameter before the microscope with $D_{desired} = D_{imagingplane} \cdot \frac{f_x}{f_{obj}}$, where f_{obj} is the focal length of the objective and f_x the focal length of the lens that focuses the laser beams onto the objectives back focal plane.
5. Calculate the magnification that is necessary to obtain the desired beam diameter with $N_{desired} = D_{desired} / D_{laser}$ where D_{laser} is the beam diameter of the laser beam (see **Note 12**).

3.4.1.2 Choice of lasers

When choosing a laser for wide-field fluorescence microscopy purposes, three parameters are most important: the wavelength, the power and the possibility to modulate the laser amplitude.

1. Choosing the excitation wavelengths strongly depends on the dyes that have to be imaged (see **Note 13** and **14**). First, make an inventory of the most frequently used fluorescent probes and their peak absorption wavelengths before deciding which wavelength lasers to implement.
2. As already discussed in subheading 3.4.1.1, the choice of laser power in combination with beam expansion determines the effective maximal intensity that fluorophores will receive. In order to have single molecule resolution when imaging with frequency of 10Hz an intensity at the sample of 100 W/cm² should be sufficient. For our system, this would require a source of 50 mW without any losses of power. In practice, it is reasonable to assume a significant loss of laser power (~50%), especially when using an AOTF, so we choose to incorporate 100 mW laser sources.
3. The option of laser modulation provides the possibility to tune laser power directly via the laser in order to alternate between laser lines and to adjust the relative power of the lasers. However, these capabilities can also be achieved by incorporation of an acousto-optic tunable filter

(AOTF) or acousto-optic modulator (AOM) or by a combination of shutters and neutral density filters (see **Note 15**).

3.4.1.3 Alignment of fluorescence excitation path

1. Choose the height of your beam and mount all the optical elements centered around this height. Keep in mind the height of the microscope entrance (see **Note 16**).
2. Mount the excitation laser with the longest wavelength (638 nm) on the optical table.
3. Mount the dichroic mirror combination (DMC, Figure 3.1) (see **Note 2**) without altering the course of the 638 nm beam (see **Note 17**).
4. Align the laser along the holes in the optical table using two irises.
5. Mount the lower wavelength lasers (561 nm, 532 nm and 488 nm) on the table and use two adjustable mirrors per laser to overlap the beam paths with the 638 nm laser beam (see **Note 18**).
6. Mount the AOTF (see **Note 19**).
7. Remove the objective and place two irises with a spacer in between onto the objective mount (see **Note 20**).
8. Align the laser beams through the two irises by inserting the mirrors into the path and using the irises as reference point for beam-walking (see **Note 21**).
9. Insert two apertures into the path after the place where you will put the beam expander (BE3, Figure 3.1) (see **Note 22**).
10. Mount the quarter-wave plate (QWP, Figure 3.1) directly after the AOTF without altering the course of the laser beams (see **Note 23**).
11. Insert translational lens mounts for the beam expander (BE3, Figure 3.1) and align their centers along the beam path (see **Note 24**).
12. Insert the longer focal length lens of BE3 and use translation to align the center of the beam with the original path.
13. Insert the shorter focal length lens of BE3 and use translation to align the center of the beam with the original path and to obtain a collimated beam after the beam expander (see **Note 25**).
14. Optionally, insert neutral density filters without altering the course of the laser beams.
15. Insert the lens mount and the imaging lens (L8, Figure 3.1) on a translation stage at a position roughly the focal distance from the objective

3

and align its center using the irises that are still inserted on the objective mount.

16. Remove the irises from the objective mount and insert the objective.

17. Insert a flow-cell (FC, Figure 3.1) and the condenser lens (CL, Figure 3.1) and move the objective such that the imaging plane is at the middle of the flow cell (see **Note 26**).

18. Remove the flow cell and the condenser lens without moving the objective and place water and a coverslip (see **Note 27**) on top of the objective lens.

19. Move the imaging lens (L8, Figure 3.1) such that a collimated beam is realized (see **Note 28**).

20. Place the diffuser (DIF, Figure 3.1) inside the focus of the beam expander to reduce issues that have to do with laser speckle.

3.4.2 Fluorescence detection design and alignment

In the detection path, the LED light for bead imaging is separated from the fluorescence emission by a dichroic mirror (DM4). Next, in order to enable imaging of three different types of fluorophores simultaneously, an Optosplit is used to separate the emission light based on wavelength and to project these spectra on different regions of the chip of an EMCCD camera. First, we present guidelines for the design of the detection path (subheading 3.4.2.1 – 3.4.2.3), followed by a step-by-step instruction of the alignment and construction.

3.4.2.1 Choice of camera

A wide variety of cameras can be found for wide-field imaging purposes. Several aspects are important to keep in mind when choosing your camera for multi-color single-molecule imaging in combination with quadruple trap optical tweezers. Most importantly, different types of camera chips exist, with their own (dis)advantages. In order to detect and discern the very low signal intensities of single molecules, it is important to choose a camera chip that has a low level of read-out noise and a high quantum efficiency. We have chosen to use an EMCCD camera chip since to date, these chips remain superior to alternatives such as CCD or sCMOS in terms of read-out noise for very low light imaging [12]. However, if one aims to achieve high image acquisition rates over a large field of view (FOV), sCMOS cameras combine faster imag-

ing rates than EMCCD cameras. Moreover, sCMOS cameras have much lower noise levels than for example normal CCD camera chips and a larger field of view [13]. If low-light microscopy applications like single-molecule detection do not lie within the scope of one's research, sCMOS cameras can provide an excellent alternative for EMCCD cameras.

Another important aspect of the camera is the size of the camera chip, which, together with the desired pixel size and the number of colors that are to be imaged side-by-side on the chip, will determine the maximal FOV that can be imaged. We designed our system to image three different colors of emission light on separate regions of the camera chip using an Optosplit. This implies that in one of the dimensions the FOV can only cover one third of the camera chip (or more if less colors are imaged simultaneously). For the purpose of Q-trapping with two braided dsDNA molecules from lambda phage in crossed configuration the minimal desired dimension that needs to be imaged is around 12 μm x 12 μm. Projection of three colors above one another would lead to an image with total imaging dimension of 36 μm. The pixel size that is required to obtain Nyquist sampling of sub-diffraction objects or single emitters such as single-molecules is at most half the diffraction-limited resolution [14]. For our system, this implies that the pixel size should be in between 90-150 nm. For an image of 36 μm, this pixel size implies that the chip should span at least ~240 pixels such that a camera chip of 512 x 512 pixels suffices.

3.4.2.2 Calculation of imaging relay lenses (L9 and L10, Figure 3.1)

1. Decide which pixel size you would like to obtain (p). Typically, for diffraction limited single-molecule resolution pixel sizes between 90-150 nm are advised (see **Note 29**).

2. Calculate the magnification that is needed to obtain this pixel size using $N_{relay} = P/(p \cdot N_{obj} \cdot N_{mic} \cdot N_{OS})$ where P is the physical size of the pixels of the camera chip, N_{obj} is the magnification of the objective, N_{mic} is any additional magnification of the microscope (see **Note 30**), N_{OS} is the optional magnification of the Optosplit (see **Note 31**).

3. Choose your relay lenses such that their focal lengths result in the desired magnification according to $N_{relay} = f_{L9}/f_{L10}$ (see **Note 32**).

3.4.2.3 Choice of dichroic mirrors and filters

Selection of the dichroic mirrors and filters is of crucial importance for the quality of single-molecule multi-color fluorescence detection. Together with the excitation wavelengths and the imaged fluorescent probes, the dichroic mirrors and emission filters determine what percentage of fluorescence signal will be captured, and to what extent your signal-to-background ratio will suffer from leakage of the excitation light and bleed through of light from other probes. Here, we will provide a few guidelines that can help to select a suitable set of dichroic mirrors and filters. It can be helpful to use online tools, such as SearchLight from Semrock[15], or software to visualize the combined effect of your choices.

1. Choose dichroic mirrors with a very high flatness (suitable for laser, super-resolution or TIRF applications), which are designed to reflect laser light.
2. Ensure that the emission filters have an OD value above 6 at the excitation wavelengths in order to reduce the leakage of the more intense excitation wavelength into your detection path.
3. Expand the captured spectrum as much as possible by choosing broad band-pass filters.

3.4.2.4 Alignment of fluorescence detection path

1. Place an 842nm short-pass filter (or equivalent) with an OD above 6 for the trapping and detection laser wavelengths (F2, Figure 3.1) in the imaging path to block any reflected 1064 or 980nm laser light (see **Note 33**).
2. Make sure that the flow cell is mounted and that the condenser lens and objective lens are positioned such that a feature of the flow cell, such as a corner, is in focus (see **Note 27**).
3. Use the LED light to place lens L9 (Figure 3.1 such that a collimated beam is obtained. Place lens L9 on an axial translation mount in order to adjust the focus of your imaging plane (see subheading 3.4.3).
4. Mount the Optosplit without any filters (OSIII, Figure 3.1) and attach the EMCCD camera (EMC, Figure 3.1).
5. Launch µManager in order to view the EMCCD camera.
6. Rotate the camera until the rectangular aperture of the Optosplit is aligned with the image on the camera.

7. Place lens L10 (Figure 3.1) in the path and adjust its axial position such that a sharp image of the flow cell can be seen on the EMCCD camera (see **Note 34**).
8. Place a dichroic mirror (DM4) to separate the LED light from the emission light (see **Note 35**).
9. Mount the bead imaging camera (BIC, Figure 3.1) and open software to view the camera image.
10. Place lens L11 (Figure 3.1) and adjust its axial position such that a sharp image of the flow cell can be seen and if necessary,
11. If necessary, adjust the angle of dichroic mirror DM4 such that the FOV overlaps with the FOV on the EMCCD camera.
12. Place the filter holders inside the Optosplit and use the handles and knobs on the Optosplit to split and move the three images (see **Note 36**).

3.4.3 Design of Z-stack imaging module

In classical wide-field fluorescence microscopy, 3D imaging is typically accomplished by making a stack of 2D images at different heights (z-stack) in the sample. Whereas conventionally, the height in the sample can be controlled by varying the relative distance between the objective and the sample stage (either by stage scanning of objective scanning), in optical trapping this typically does not work: In optical tweezers experiments, the sample of interest is typically suspended in solution between microspheres that are held in the foci of the trapping laser beams. Moving the objective lens will thus also move the trapped microspheres and the tethered sample. As a result, conventional stage-scanning or objective scanning cannot be used to acquire a z-stack. Despite this complication, several reasons can be put forward why it is advantageous or even critical to be able to control the axial position of the imaging plane: i) the interplay between scattering force and gradient force in an optical trap causes an axial offset of the trapped object - and thus of the manipulated sample - that depends on the material and the size of the trapped object; ii) quadruple trap optical tweezers are designed to have the ability of moving the traps in the axial direction by varying the collimation of the trapping beam (in our case, by translating one lens of beam expander BE2, Figure 3.1; iii) optical tweezers experiments with objects such as cells that have a thickness well beyond the focal plane depth
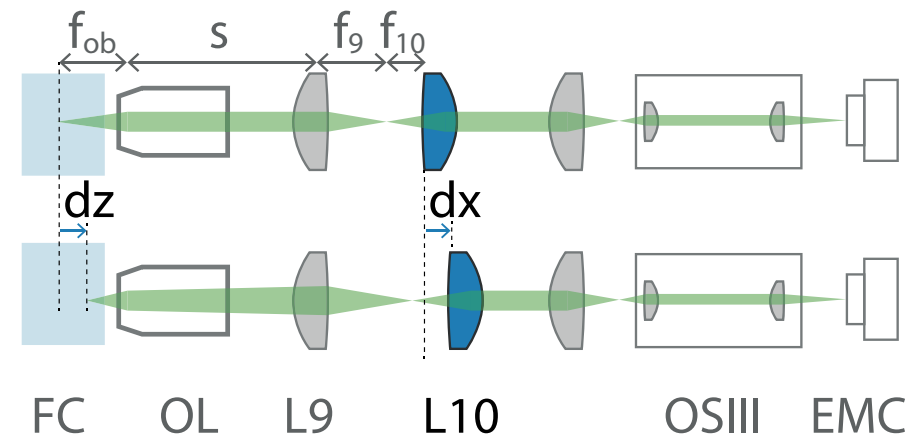
Figure 3.2: Schematic of optical elements to illustrate Z-stacking module. Upon moving lens L10 a distance dx, the imaging plane that is projected onto the camera (EMC) is moved with a distance dz inside the flow cell (FC) without moving the objective lens (OL).

that cannot be entirely imaged with a fixed focal plane; iv) to correct for chromatic aberrations.

Instead of moving the objective to change the position of the imaging plane, lens L10 can be moved (Figure 3.1 and Figure 3.2). A manual translation stage is sufficient when a fixed sample plane has to be imaged. However, if during the experiment the sample plane can change e.g. while using quadruple trap optical tweezers with complicated experimental schemes of DNA entanglement, or when 3D objects have to be imaged, it is advisable to implement a computer-controlled stage that can be connected to the imaging software in order to easily refocus or acquire a Z-stack.

When choosing the translation stage it is important to keep in mind the following aspects.

1. The total range and the minimal step size of the translation stage determine what maximal and minimal axial features of the sample can be imaged. The following expression can be used to calculate the required displacement of lens L10

$$dx = \frac{f_9{}^2 dz}{f_{ob}{}^2 + f_9\, dz - f_{ob}\, dz - s\, dz}$$

in order to visualize an imaging plane with a displacement (dz) with respect to the objective's focal plane f_{ob}, where f_{10} is the focal length of the microscope's tube lens and s the distance between the objective and the tube lens (Figure 3.2) (see **Note 37**).

2. The translational velocity of the stage determines how fast consecutive images of a Z-stack can be taken. When fast dynamics have to be captured, a fast stage is required.

3. The movement of translation stages can have either relative or absolute positioning (also referred to as open and closed loop), where the latter is generally more expensive. Absolute positioning provides the possibility to move the stage back and forth between certain predefined points with high accuracy. Therefore, absolute positioning will facilitate reproducibility of experiments.

Taking these considerations into account, we have incorporated a closed-loop linear stage with a total range of 22 mm, corresponding to a total range in the sample of just over 6 μm.

3.4.3.1 Z-stage alignment and implementation

1. While lens L10 is inside the detection path, image a feature inside the flow cell or sample of which the axial position can be reproducibly found.

2. Remove lens L10 and mount it on the motorized stage such that it has the same total height as it used to have before.

3. Reposition the motorized stage with lens L10 into the detection path such that the image on the camera is again sharp and at the same position.

4. Move the motorized stage to its extremities and adjust the rotation of the stage such that the defocused image on the camera doesn't change in lateral position and fix it on the optical table.

5. Connect the controller of the motorized stage with a computer and open the provided software for control over its position.

6. Instructions for implementation of driver software to control the stage movement in μManager can be found on the μManager website [16].

3.4.4 Assay preparation

In subheading 3.4.4 – 3.4.6, we will provide a step-by-step description of two experimental assays. The first assay is a dual trap experiment where multiple dsDNA molecules will be attached at several different heights between two beads forming a three-dimensional structure. This assay can be used to test and highlight the capabilities of three-dimensional fluorescence imaging. The second assay is a Q-trapping assay where two dsDNA molecules are attached in between two bead pairs and subsequently wrapped around one another (Figure 3.3). Imaging will be performed with two different dyes in order to test and exemplify the simultaneous multi-color fluorescence imaging. The results of the two assays are shown inFigure 3.4.

3.4.4.1 Bleach cleaning

1. Rinse the syringes with MilliQ water and remove all but 1 mL, subsequently flush at least 0.5 mL per channel through the system.
2. Remove all residual water and add 0.7 mL bleach solution to each syringe. Flush slowly through the flow system over a time period of 30 to 60 minutes.
3. Remove any bleach left in the syringes and rinse all with MilliQ water. Like in step 1, leave 1 mL MilliQ in the syringes and flush at least 0.5 mL per channel.
4. Remove all residual liquid from the syringes, add 1.5 mL sodium thiosulfate solution, and flush through all channels over a period of 5-10 minutes.
5. Empty the syringes and do a final rinse and flush with MilliQ water like in step 1 and 3.

3.4.4.2 Flow-cell passivation

1. Flush all channels of the flow cell with 0.5 mL PBS.
2. Remove residual PBS from all syringes.
3. Flush 0.5 mL BSA solution through al channels for 10 minutes
4. Turn down the flow through the channels by closing all the valves and leave for 30 minutes.
5. Repeat step 3 and 4 with Pluronic® solution.
6. Flush all channels with at least 0.5 mL of the buffer you will use during the experiments.

3.4.4.3 Starting a dual trap experiment

1. Make sure the piezo mirror controller is turned on (see **Note 38**).
2. Remove half wave plate HW1 (Figure 3.1) from the optical path.
3. Turn on shutter controllers and make sure all shutters are closed so no 1064 nm light is coming through the objective.
4. Turn on the PSDs.
5. Turn on the LED.
6. Start the software to control the optical traps and microfluidics.
7. Place immersion water on the objective and oil on the condenser of the microscope (see **Note 39**).
8. Focus in the middle of the flow cell, by adjusting the height of the objective.
9. Turn on the 1064 nm laser and open all shutters to let 1064 nm enter the objective.

3.4.4.4 Starting a quadruple trap experiment

1. Make sure the piezo mirror controller is turned on (see **Note 38**).
2. Insert half wave plate HW1 (Figure 3.1) in the optical path of the 1064 nm laser.
3. Follow steps 3-9 for starting the dual trap experiment as described in subheading 3.4.4.3.
4. Turn on the 980 nm laser.
5. Adjust the force detection path so the 980 nm laser is detected on the PSD2 (see **Note 40**).

3.4.4.5 Turning on fluorescence

1. Make sure the lasers are blocked before they enter the microscope. Begin with turning on all needed fluorescence lasers on full power and let them run for 30 minutes.
2. Turn on the diffuser and AOTF.
3. Start μManager
4. Set the imaging parameters as a starting point to: gain: 50, laser power: 100, exposure time: 1000 ms.
5. Insert the right filter cubes for your dyes in both the microscope and Optosplit
6. Block the emission channels that you are not using with the blocking filters of the Optosplit.

7. Turn on the camera.

3.4.5 3D imaging of multiple DNA molecules between two beads

3.4.5.1 Catching beads, DNA and force calibration

1. Start a dual trap experiment as described in subheading 3.4.4.3.
2. Turn on fluorescence as described in subheading 3.4.4.5.
3. Insert bead solution in syringe 1, DNA solution into syringe 2, PBS solution into syringe 3 and SxO intercalator into syringe 4.
4. Open valves and apply pressure to flush solutions into the flow cell (see **Note 41**).
5. Move traps towards channel 1, catch two beads and move to channel 3.
6. Close all the valves to turn off flow and calibrate the force by fitting a Lorentzian to the power spectrum of Brownian motion of bead 1 in the trap.
7. Reset the force to zero
8. Position the traps such that bead 2 is downstream of bead 1 and that they are separated by at least 20 μm.
9. Open valves again and apply pressure to flush solutions through the flow cell.
10. Move the traps to channel 2 containing the DNA solution.
11. Decrease the bead-to-bead distance to around 5 μm and leave the beads like that for half a minute
12. Slowly increase the bead-to-bead distance to 16 μm until an increase in the force is detected. If no increase in the force is detected go back to step 11.
13. Set the distance between the beads to 16 μm.
14. Move the beads to channel 3.
15. Close the valves to turn off the flow.
16. Make a force-extension curve to test whether more than one dsDNA construct is tethered in between the beads. To do so, set the bead-to-bead distance to 5 μm and slowly increase the distance while recording the force. A sharp increase of the force around the contour length of

16 μm is expected. If this increase in force continues well beyond 65 pN several DNA molecules are attached to the beads (see **Note 42**).

3.4.5.2 3D imaging of multiple DNA molecules between two beads

1. Prepare the experiment as described in subheading 3.4.5.1.
2. Move the beads to a bead-to-bead distance where a force of around 20 pN is applied to the beads.
3. Move the beads to channel 4 containing the intercalator SxO.
4. Take snapshot using μManager and adjust contrast to see if any fluorescence signal is detected between the two beads. If not increase the bead-to-bead distance a little bit and check again by taking a snap-shot, until a signal can be observed (see **Note 43** and **Note 44**).
5. Start imaging. Make sure the option Z-stack is selected with an appropriate range and step size (see **Note 45**). This should result in an image such as shown in Figure 3.4A.

3.4.5.3 Data analysis

Visualizing Z-stacks can be done using ImageJ. In order to project a 3D-image onto a single 2D image, a color-coded maximum intensity projection can be performed using the option *Hyperstacks > Temporal Color Code* (see Figure 3.4A). ImageJ also offers plugins to visualize 3D reconstructions that can for example be rotated.

3.4.6 Dual-color imaging of intercalator binding to dsDNA

3.4.6.1 Catching DNA between the bead pairs

1. Start a quadruple trap experiment as described in subheading 3.4.4.4.
2. Turn on fluorescence as described in subheading 3.4.4.5.
3. Insert bead solution in syringe 1, DNA solution into syringe 2, PBS solution into syringe 3, YOYO intercalator solution in syringe 4 and SxO intercalator solution into syringe 4.
4. Open valves and apply pressure to flush solutions into the flow cell (see **Note 41**)
5. Move traps towards channel 1, catch four beads and move to channel 3.
6. Close all the valves to turn off flow and calibrate the force by fitting a Lorentzian to the power spectrum of Brownian motion of bead 1 and 4 in the trap.

7. Reset the force to zero
8. Position the traps such that bead 2 is downstream of bead 1, and bead 3 is downstream of bead 4, and that they are separated by 20 µm.
9. Open valves again and apply pressure to flush solutions through the flow cell.
10. Move the traps to channel 2 containing the DNA solution.
11. Repeatedly decrease and increase the bead-to-bead distance of bead 1 and 2 by approaching to around 5 µm and withdrawing up till 20 µm until an increase in the force is detected. Set the bead-to-bead distance to 16 µm. Repeat this procedure for bead 3 and 4.
12. Move the beads to channel 3.
13. Close the valves to turn off the flow.
14. Make a force-extension curve to test whether a single dsDNA construct is tethered in between each of the bead pairs. To do so, set the bead-to-bead distance to 5 µm and slowly increase the distance up till a distance of 17 µm while recording the force. The force-extension curve should look similar to that of a single dsDNA as was described previously [17], with a sharp increase of the force around the contour length of 16 µm and the presence of a plateau in the force around 65 pN.

3.4.6.2 Wrapping the two DNA strand around one another

1. Catch four beads and attach DNA pairwise as described in subheading 3.4.6.1.
2. Move bead 3 and 4 upwards (seeFigure 3.3)
3. Position bead 3 and 4 such that the DNA is perpendicularly oriented with respect to the DNA between bead 1 and 2.
4. Move bead 3 and 4 downwards until they are below bead 1 and 2.
5. Move bead 3 back to its original position
6. Move bead 3 and 4 upwards until they are in the same plane as bead 1 and 2.

3.4.6.3 Dual-color imaging of intercalator binding to two dsDNA molecules

1. Catch four beads and DNA, and calibrate the force as described in subheading 3.4.6.1.
2. Wrap two dsDNA strands around one another as described in subheading 3.4.6.2.
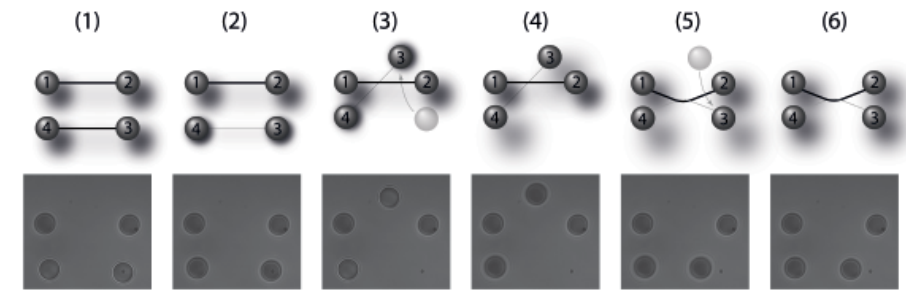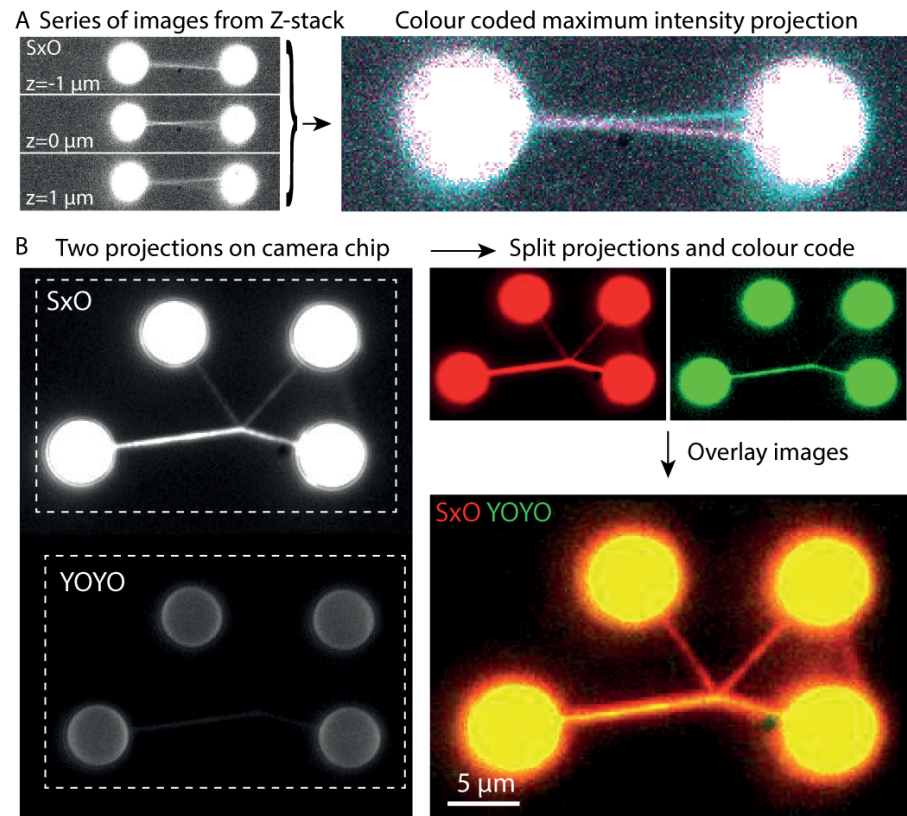
Figure 3.3: Schematic and corresponding BF images showing how the wrapped DNA conformation is accomplished. After catching two DNA strands between two bead pairs (1), one bead pair is brought downwards (2) and subsequently moved across the other DNA strand (3). After moving the bead pair upwards (4), and back over the other DNA strand (5) the bead pair can be moved back to its original position (6) resulting in two intertwined DNA strands.

3. Bring one of the strands on tension (>30 pN) while the other is relaxed and move inside channel 4 containing the intercalator YOYO.
4. After one minute of incubation, move to the buffer channel while keeping the tension on the YOYO stained strand.
5. Apply some tension (10-30 pN) on the originally relaxed DNA strand as well.
6. Move to channel 5 containing the intercalator SxO.
7. Start imaging using µManager by selecting simultaneous exposure to 488 nm and 532 nm excitation light. This should result in an image as shown in Figure 3.4B. Fine-tune exposure time and power to reduce photo nicking of the DNA (see **Note 44**). Change the relative intensity between the two DNA strands by changing the relative forces (see **Note 43**). Imaging should be finished within a minute since YOYO will gradually unbind the DNA (see **Note 46**).

3.4.6.4 Data analysis

Data analysis can be performed using software such as ImageJ, which provides options to select part of the raw image with a region of interest (ROI) (*Analyze > Tools > ROI Manager*) and to change relative contrast settings (*Image > Adjust > Brightness/Contrast*). Color coding can be performed by several options in ImageJ under the heading *Image > Color*, which also provides the possibility to make an overlay image (*Image > Color > Make Composite*) (Figure 3.4B).

A Series of images from Z-stack   Colour coded maximum intensity projection

B   Two projections on camera chip → Split projections and colour code

Overlay images

Figure 3.4: Overview of raw data examples and the data analysis steps resulting in the final image. A) Z stack images of SxO binding to several DNA strands between two beads and the corresponding color coded maximum intensity projection. B) One camera frame showing the two projections split based on emission wavelength that correspond to SxO (upper) and YOYO (lower) emission light. The two projections are separated, color coded and finally overlaid using analysis software such as ImageJ.

3.5   Notes

1. Together with the lenses used in the 4f configuration and the objective lens the range of the steering mirrors determines the maximum displacement of the optical traps. In order to have enough space to maneuver the traps around one another and to perform e.g. experiments on single stranded lambda phage DNA we have chosen for a large range steering mirror. For experiments with smaller DNA constructs this might not be necessary.

2. Choose your dichroic mirrors to be of laser or super resolution/TIRF flatness (i.e. a radius of curvature of around 255 m or more) to achieve optimal beam quality.

3. The AOTF is able to tune the laser power tenfold.

4. Course tuning of overall excitation power can be achieved using neutral density filters.

5. Beam expansion is dependent on initial beam width and desired illumination area, see subheading 3.4.1.1.

6. The diffuser makes a coherent-speckle-free homogeneous illumination area, reducing the difference in emission intensity of the dyes so it is possible to count the number of dyes in the region of interest.

7. The short-pass filter should have an OD value well above 6 at the trapping laser and detection laser wavelengths in order to reduce back ground signal.

8. Passivation solutions are stored in PBS with 10 mM NaN_3 and 1 mM EDTA to prevent bacterial growth.

9. Quantitative analysis for example allows for determination of the number of fluorophores.

10. Experiments with DNA often make use of lambda phage constructs, which have a contour length of 16 µm.

11. A difference of 10% (p = 0.1) allows readily discriminating between one or two fluorophores.

12. For our system, with D_{laser} = 700 µm, f_x = 500 mm and f_{obj} = 3.33 mm, we find a desired magnification of $N_{desired}$ = 17.

13. Several online tools, like SearchLight, are available that can be used to visualize excitation and emission spectra and to combine these with lasers, filters et cetera [15].

14. In our lab, we frequently work with a broad series of synthetic dyes such as Alexa Fluor 488/555/647, Cy3 and Cy5, and different types of intercalators, but also with organic dyes such as eGFP and mCherry. Therefore, we choose to combine four lasers (488, 532, 561 and 639 nm) to have optimal flexibility.

15. Our choice for the use of an AOTF is based on the ease of use and the fact that µManager drivers are available for this device.

16. If the height of the microscope entrance is not practical to work with, it might be needed to include a periscope in your design, to avoid mounting on tall posts that are less rigid than shorter posts.

17. It is advisable to use two fixed reference points, one close by and one far away, to ensure that the beam path is not changed.

18. With the use of two mirrors, full control over both beam position and angle can be achieved. Iteratively, use the first mirror to center the beam at an aperture close by, and the second mirror on an aperture as far away as possible. This process of beam-walking results in collinear laser beams.

19. The AOTF generally induces an angle in the laser paths. It is advisable to check whether the laser beams still overlap after inserting the AOTF.

20. Choose the spacer between the irises as big as possible for optimal alignment.

21. Insert at least two mirrors between the AOTF and the microscope in order to have the possibility of beam-walking the laser beams through the objective.

22. These apertures will remain in the setup as fixed reference points if later adjustment of the different lasers is necessary.

23. The QWP transforms the linearly polarized laser light into circularly polarized light. This ensures that dyes with a fixed orientation will be excited to a similar extend independently of their orientation.

24. Usage of a cage system to hold the lens mounts greatly facilitates alignment and later adjustment of lenses.

25. To check collimation, either create a very long path and move the lens until the beam diameter stays constant, or use a shear plate device and move the lens until a parallel pattern of interference stripes is obtained.

26. Many microscopes have a front port on which a camera can be directly mounted to inspect the imaging plane of the objective.

27. The thickness of the coverslip should be according to the specifications of the objective. In our case 170 μm

28. Obtaining a collimated beam can be challenging because of the intrinsic divergence of very narrow Gaussian beams. Checking collimation can best be performed by projecting the outgoing laser beam on a point far away and trying to minimize the spot size.

29. The smaller the pixel size, the more accurately a single emitter can be located. However, the relative contribution of noise gets larger when the signal of a single emitter is spread over more pixels. Therefore, more photons of the same emitter are needed in order to detect it, implying longer illumination times and/or higher excitation powers. In our lab, we have chosen a pixel size of 130 nm as a reasonable compromise.

30. Some microscope bodies offer the possibility to have an extra e.g. 1.5x magnification.

31. An additional magnification inside the Optosplit can be requested from the manufacturer.

32. Keep in mind that the focal length of L10 should be minimally 5 cm in order to overlap the focus with the focus of the Optosplit lens.

33. Be aware to always have this filter in the detection path when the trapping laser is on. Omitting this step will seriously damage the camera chip.

34. Image a point in the flow cell that is easily recognizable such as a corner.

35. For optimal imaging quality it is advised to choose a dichroic mirror that transmits the fluorescence emission light instead of the LED light.

36. A detailed description of the alignment steps of the Optosplit itself is given in the Optosplit manual.

37. Moving lens L10 results in a change of the magnification of $N_{tot} = \frac{f_9^2 + dx(f_9 - f_{ob} - s)}{f_9 f_{ob}}$. For our system, moving the lens over it is full range results in a change of the magnification of less than 0.1%.

38. In principle, the MCL piezo mirror is never turned off. If it has to be turned on/off, make sure it is not connected to the computer when doing so.

39. The use of water or oil depends on specific the requirements of the objective and condenser in the setup.

40. Make sure that the 1064 nm trapping laser is blocked from this PSD using a 1000 nm short pass filter, only 980 nm light should be registered on this PSD.

41. The bead imaging camera can be used to monitor (by the presence of beads) whether solutions are inside the flow cell.

42. A single dsDNA construct shows a plateau in the force-extension curve around 65 pN [18,19].

43. Since intercalator binding to DNA is strongly force dependent, increasing the force can be used to facilitate binding and consequently imaging of the intercalator [20].

44. If frequent breakage of the DNA is observed by a drop in the force and the disappearance of fluorescence, it is likely that due to exposure of the intercalator to the excitation light photo nicking of the DNA backbone is induced. It is advisable to lower the excitation power and/or decrease the force on the DNA.

45. For objects smaller than the beads, as a rule of thumb a range of plus and minus half the bead diameter with a step size of 500 nm can be used as a starting point.

46. Note that the SxO will bind both strands of DNA. The YOYO will remain bound up to one minute.

3.6   Competing interest statement

The combined optical tweezers and fluorescence technologies used in this article are patented and licensed to LUMICKS B.V., in which I.H., E.J.G.P. and G.J.L.W. have a financial interest.

References

1. Hashemi Shabestari, M., Meijering, A. E. C., Roos, W. H., Wuite, G. J. L. & Peterman, E. J. G. Chapter Four - Recent Advances in Biological Single-Molecule Applications of Optical Tweezers and Fluorescence Microscopy. in Single-Molecule Enzymology: Nanomechanical Manipulation and Hybrid Methods (eds. Spies, M. & Chemla, Y. R. B. T.-M. in E.) vol. 582 85–119 (Academic Press, 2017).
2. Moffitt, J. R., Chemla, Y. R., Smith, S. B. & Bustamante, C. Recent advances in optical tweezers. Annu. Rev. Biochem. 77, 205–228 (2008).
3. Brouwer, I. et al. Sliding sleeves of XRCC4-XLF bridge DNA and connect fragments of broken DNA. Nature 535, 566–569 (2016).
4. Gutierrez-Escribano, P. et al. A conserved ATP- And Scc2/4-dependent activity for cohesin in tethering DNA molecules. Sci. Adv. 5, 1–16 (2019).
5. King, G. A., Biebricher, A. S., Heller, I., Peterman, E. J. G. & Wuite, G. J. L. Quantifying Local Molecular Tension Using Intercalated DNA Fluorescence. Nano Lett. 18, 2274–2281 (2018).
6. Heller, I. et al. Versatile Quadruple-Trap Optical Tweezers for Dual DNA Experiments. in Optical Tweezers: Methods and Protocols (ed. Gennerich, A.) 257–272 (Springer New York, 2017). doi:10.1007/978-1-4939-6421-5_9.
7. Heller, I. et al. STED nanoscopy combined with optical tweezers reveals protein dynamics on densely covered DNA. Nat. Methods 10, 910–916 (2013).
8. Lee, W. M., Reece, P. J., Marchington, R. F., Metzger, N. K. & Dholakia, K. Construction and calibration of an optical trap on a fluorescence optical microscope. Nat. Protoc. 2, 3226–3238 (2007).
9. Heller, I. et al. Versatile Quadruple-Trap Optical Tweezers for Dual DNA Experiments. in Optical Tweezers: Methods and Protocols 257–272 (2017).
10. Brouwer, I. et al. Probing DNA-DNA Interactions with a Combination of Quadruple-Trap Optical Tweezers and Microfluidics. in Optical Tweezers: Methods and Protocols 275–293 (2017).
11. Candelli, A. et al. A toolbox for generating single-stranded DNA in optical tweezers experiments. Biopolymers 99, 611–620 (2013).
12. nderson, C. M., Georgiou, G. N., Morrisoni, I. E. G., Stevenson, G. V. W. & Cherry, R. J. Tracking of cell surface receptors by fluorescence digital imaging microscopy using a charge-coupled device camera. Low-density lipoprotein and influenza virus receptor mobility at 4°C. J. Cell Sci. 101, 415–425 (1992).
13. Kubitscheck, U. Fluorescence microscopy: from principles to biological applications. (Weinheim, Wiley-Blackwell, 2013).
14. Nyquist, H. Certain Topics in Telegraph Transmission Theory. Trans. Am. Inst. Electr. Eng. 47, 617–644 (1928).
15. https://searchlight.semrock.com/. https://searchlight.semrock.com/.
16. https://micro-manager.org/wiki/Device_Support. https://micro-manager.org/wiki/Device_Support.
17. Gross, P. et al. Quantifying how DNA stretches, melts and changes twist under tension. Nat. Phys. 7, 731–736 (2011).
18. Smith, S. B., Cui, Y. & Bustamante, C. Overstretching B-DNA : The Elastic Response of Individual Double-Stranded and Single- Stranded DNA Molecules Published by : American Association for the Advancement of Science Stable URL : http://www.jstor.org/stable/2889889. Science (80-.). 271, 795–799 (1996).
19. Cluzel, P. et al. DNA: An Extensible Molecule. Science (80-.). 271, 792–794 (1996).
20. Biebricher, A. S. et al. The impact of DNA intercalators on DNA and DNA-processing enzymes elucidated through force-dependent binding kinetics. Nat. Commun. 6, 7304 (2015).

Imaging unlabeled proteins on DNA with super-resolution
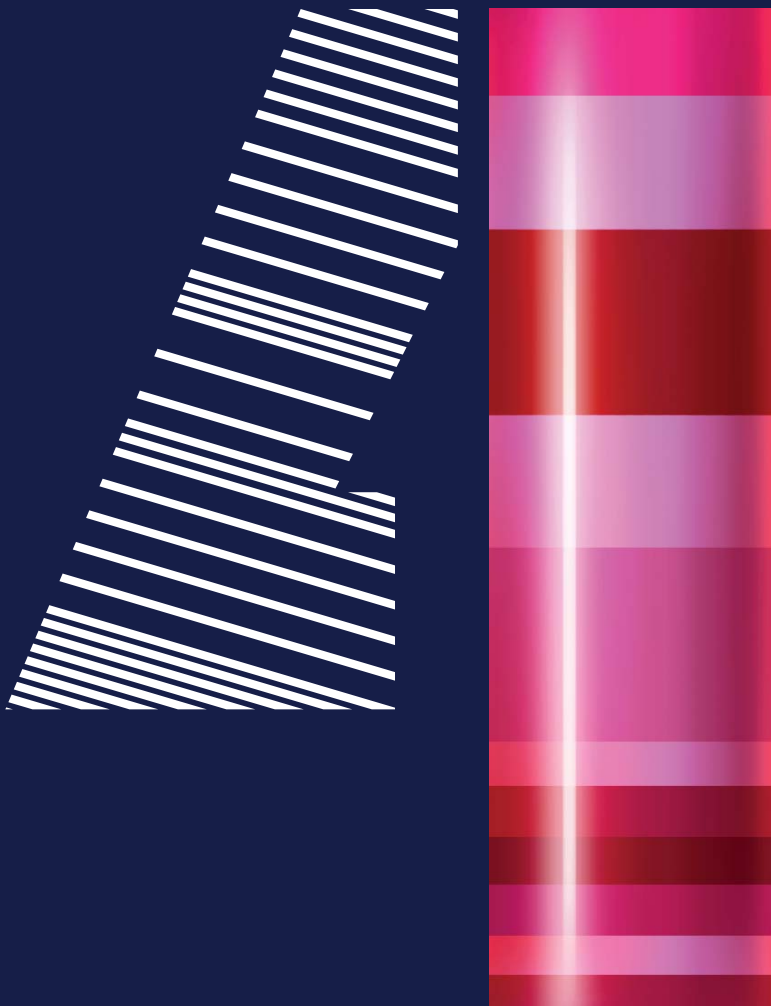
4.1 Abstract

Fluorescence microscopy is invaluable to a range of biomolecular analysis approaches. The required labeling of proteins of interest, however, can be challenging and potentially perturb biomolecular functionality as well as cause imaging artefacts and photo bleaching issues. Here, we introduce inverse (super-resolution) imaging of unlabeled proteins bound to DNA. In this new method we use DNA-binding fluorophores that transiently label bare DNA but not protein-bound DNA. In addition to demonstrating diffraction-limited inverse imaging, we show that inverse Binding-Activated Localization Microscopy or "iBALM" can resolve biomolecular features smaller than the diffraction limit. The current detection limit is estimated to lie at features between 5 nm and 15 nm in size. Although the current image-acquisition times preclude super-resolving fast dynamics, we show that diffraction-limited inverse imaging can reveal molecular mobility at ~0.2 sec temporal resolution and that the method works both with DNA-intercalating and non-intercalating dyes. Our experiments show that such inverse imaging approaches are valuable additions to the single-molecule toolkit that relieve potential limitations posed by labeling.

4.2 Introduction

Fluorescence microscopy is the imaging method of choice for an extensive range of in vivo and in vitro studies in life sciences. In these studies, imaging of (individual) labeled molecular complexes typically provides spatially and temporally resolved information of their presence, location, motion, colocalization, conformation, and stoichiometry as well as insight into the morphology of extended molecular architectures[1,2]. Fluorescence microscopy typically relies on the fluorescent labeling of proteins of interest through their fusion with fluorescent proteins or through (site-)specific attachment of synthetic dyes. While such labeling can often be performed with high specificity and efficiency, labeling is also associated with significant challenges and drawbacks related to the labeling procedures and optimization involved. In particular, the most critical drawbacks occur if labeling interferes with the structure and/or function of the biomolecule of interest or if it causes for example artificial clustering of labeled proteins[3].

At present, label-free imaging techniques that circumvent drawbacks associated with labeling are receiving increased attention. These techniques include second and third harmonic generation, stimulated Raman scattering, interferometric scattering (iSCAT), and interference reflection microscopy[4–7]. Here we set out to develop a fluorescence-based approach capable of visualizing unlabeled proteins bound to DNA. Instead of labeling and imaging the proteins of interest themselves, we employ an inverse imaging strategy by imaging the regions of DNA that are not covered with protein using transiently-binding DNA-labels. While in principle any fluorescent DNA-binding label can be used, we first focus on the use of commercially available DNA-intercalating dyes that exhibit 2-3 orders of magnitude enhanced fluorescence upon binding DNA[8]. These well-studied dyes have been used extensively to report on the presence and location of double-stranded DNA, on structural transitions of DNA, as well as on DNA replication and DNA digestion activities[9–14]. Indeed, fluorescent intercalator displacement assays have demonstrated that DNA-bound proteins compete with intercalators for DNA-binding sites, such that a suppressed signal from these labels can report on the presence of unlabeled DNA-binding proteins[15,16]. Here we further extend the power of this approach by imaging the DNA intermittently bound by intercalators and thus retrieving spatially-resolved information on unlabeled DNA-bound proteins.

Super-resolution approaches have enhanced the resolving power of fluorescence microscopy by improving its spatial resolution from the traditional diffraction limited resolution of ~250 nm to 25 nm or less[17–19]. Such enhanced resolution has also been applied to intercalator-based imaging of DNA: by localizing intermittent DNA-binding events of intercalators in an approach termed "Binding-Activated Localization Microscopy" (BALM), super-resolved images of double-stranded DNA have been obtained with a spatial resolution of 14 nm[20]. Inspired by this study, we present experimental evidence that DNA-bound-protein sections can be visualized with a resolution better than the diffraction limit without the need for labeling the proteins, in an approach we call "inverse Binding-Activated Localization Microscopy", iBALM (Figure 4.1a). We use Monte Carlo simulations to obtain insight into the parameters determining the spatial resolution. Finally, we show that the inverse imaging approach extends to the use of transiently DNA-binding species other than intercalators to visualize the dynamics of protein complexes moving along DNA.

4.3 Materials and Methods

The Monte Carlo simulations. Locations of binding events were randomly generated over a length of 1 µm DNA and events that overlapped the blocked region were subsequently discarded. Normalized Gaussian profiles of localizations were summed according to position. The width of the Gaussians was calculated using the formula of localization uncertainty as described in[21]

$$\langle (\Delta x)^2 \rangle = \frac{s^2 + a^2/12}{N} \left(\frac{16}{9} + \frac{8\pi(s^2 + a^2/12)b^2}{Na^2} \right), \qquad 4.1$$

where s is given by the standard deviation of the point spread function, a is the pixel size, N is the number of photons collected and b is the background noise. For our experimental scheme a=130 nm and b=5.2. The standard deviation of the point spread function can be calculated by $s = 0.25\lambda/NA$, where λ is the light wavelength (λ=570 nm for SxO emission) and NA the numerical aperture of the objective (NA=1.2). The number of photons for each binding event was drawn from a gamma distribution with a scale parameter equal to the number of photons as a simulation parameter and a shape parame-

ter, k, measured from experimental data (k=2.95). We next compared the results from this approach to the actual position of the protein patch and determined the percentages of correct localizations and false positives. On a non-blocked region of the DNA, mean and standard deviation of the summed intensity profile along the DNA was determined. The threshold, given by $I_{th} = I_{av} - N * \sigma_I$, was used as criterion to test whether a blocked region was detected and whether any non-blocked regions would pop-up as false positives. Here, the parameter N tunes the tradeoff between minimal detection size and false positives. For any given parameter set, 20 iterations of every parameter combination were performed and subsequently the chance of true and false positives was calculated.

Instrumentation. Experiments were performed on a custom-built inverted microscope that combined dual-trap optical tweezers with either wide-field or confocal fluorescence microscopy[22,23]. In brief, two optical traps are generated using a 10 W 1064nm CW fiber laser (YLR-10-LP, IPG Photonics). Beam splitting and recombination is achieved using two polarizing beam-splitter cubes (10BC16PC.9, Newport). Independent trap steering is done via a coarse-positioning piezo stepper mirror (AG-M100N, Newport) and an accurate piezo mirror (Nano-MTA2X Aluminium, Mad City Labs). Two 300 mm lenses are used to couple the laser beams into a water-immersion objective (Plan Apo x60, numerical aperture 1.2, Nikon). Force measurement is done with back-focal-plane interferometry by collecting the light using a condenser lens and separating the two trapping paths with a polarizing beam-splitter cube and two position-sensitive detectors (DL100-7PCBA3, Pacific Silicon Sensor). Fluorescence microscopy was performed on a wide-field setup using an EMCCD camera (iXON+ 897E, Andor Technology). For the localization experiments, the EM-gain was turned off. A 491-nm excitation laser (Cobolt Calypso 50mW CW) was used for exciting YOPRO and a 532-nm excitation laser (Cobolt Samba 50mW CW) was used for exciting SYTOX Orange. XLF experiments were performed with a confocal fluorescence setup as described before[22]. Briefly, a pulsed laser system (ALP-745-710-SC) was used to create an excitation beam centred at 467nm. A tip/tilt piezo mirror (S-334.1SD, Physik Instrumente GmbH & Co) was used for beam scanning and a fiber coupled APD (APDs SPCM-AQRH-14-FC, fibers SPCM-QC9, PerkinElmer) was used for detection. Line scanning of 190ms was used to create XLF images.

ThunderSTORM analysis.   Localization of binding events was performed using the imageJ plugin ThunderSTORM. To each local maximum a fit of a Gaussian was performed with the weighted least-squares method using a fitting radius of 3 pixels. The results were visualized by depicting every localization as a normalized Gaussian without performing any selection on the localizations. The mean intensity of the localizations was 366 photons (mode 231 photons), while the background had an offset of 18±5 photons. This yielded an average localization uncertainty of 25 nm (mode 19 nm).

DNA, intercalators, proteins and buffers.   Biotinylated DNA constructs were produced from bacteriophage λ DNA as described previously[23]. DNA-dumbbell constructs were produced in the flow cell by spontaneous binding of biotinylated DNA to streptavidin-coated polystyrene microspheres (4.65μm diameter, Spherotech). SYTOX Orange and YO-PRO-1 were obtained from Invitrogen. hRAD51 labeling with Alexa 647 was performed as described previously[24]. RAD51 experiments were performed in RAD51 buffer, containing 20 mM TrisHCl at pH 7.5, 1 mM CaCl2 and 100 mM KCl. For localization experiments, 20μM hRAD51 was pre-incubated for one hour with 10ng/μL bacteriophage λ DNA, 20 mM TrisHCl at pH 7.5, 2 mM CaCl2, 1 mM ATP and 30 mM KCl. After incubation, hRAD51-DNA constructs were diluted in RAD51 buffer. For the fluorescence intercalator displacement assay (Supplementary Figure 4.1), a similar pre-incubation was performed with variable hRAD51 concentration. After incubation, the DNA was diluted in RAD51 buffer containing 1 μM SxO to yield a ~10% staining of the DNA. Absorption spectra were collected with a UV-Vis spectrophotometer (Varian Cary 4000). hXLF labeling with eGFP was performed as was described before[25]. TFAM labeling with Alexa 555 was performed via cysteine-maleimide linkage as described before[26]. TFAM experiments were conducted in 10mM HEPES pH 7.5, 25mM NaCl, 1mM DTT, 0.05% casein and 0.05% Pluronics. hXLF-eGFP experiments were conducted in 20 mM Tris-HCl (pH 7.5), 1 mM DDT and 25 mM KCl.

4.4   Results

As a first demonstration of the ability to visualize unlabeled proteins on DNA, we studied human recombinase protein RAD51 (hRAD51) using DNA-intercalation-based inverse imaging. Here, DNA was incubated with hRAD51 in a cal-
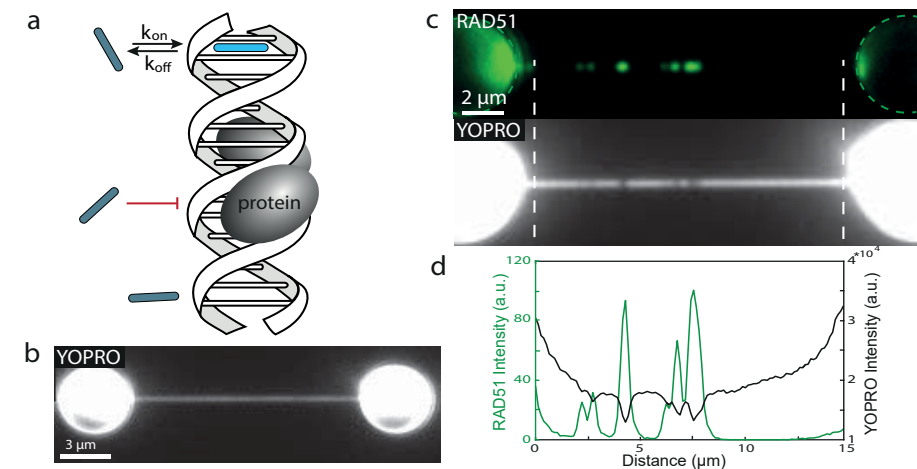
Figure 4.1: Inverse microscopy proof of principle. a) Schematic of inverse microscopy principle. Inverse microscopy relies on the competition of binding sites between protein (grey oval) and fluorescent probe (rod). b) YOPRO imaging in the absence of hRAD51 reveals a homogeneously stained DNA strand (exposure time: 1s). c) Fluorescence wide-field images of hRAD51-Alexa647 signal (upper, acquired in absence of YOPRO) and the subsequently acquired YOPRO image (lower) on DNA that is tethered between two optically trapped polystyrene beads (exposure time: 1s). d) Intensity profile between the white dotted lines of the wide-field images of (c) shows a strong correlation between the position of peaks in the hRAD51-A647 image (green profile) and the dips in the YOPRO image (black profile).

cium-containing buffer to form DNA-bound hRAD51 filaments[27,28] (methods). This DNA was subsequently tethered to two optically trapped polystyrene beads and stretched to yield a DNA-dumbbell configuration. In this experiment, we used Alexa Fluor 647-labeled hRAD51 to allow direct confirmation of the presence and location of hRAD51 on the DNA (Figure 4.1a) in conventional wide-field epifluorescence imaging (methods). Concurrently, we used the mono-intercalator YO-PRO-1 (YOPRO) in order to visualize the DNA for inverse imaging. Even at low average intercalation density (<10%), the rapid and sequence-independent DNA-binding kinetics of YOPRO (~10 ms-1), combined with ~1s camera exposure time, yields a uniform staining of the DNA in absence of hRAD51 (Figure 4.1b). In presence of DNA-bound hRAD51, however, regions of suppressed YOPRO signal (i.e. 'dark' spots along the DNA) are clearly visible (Figure 4.1c). Indeed, the locations of these dark spots in the YOPRO image correspond excellently to the locations of DNA-bound hRAD51
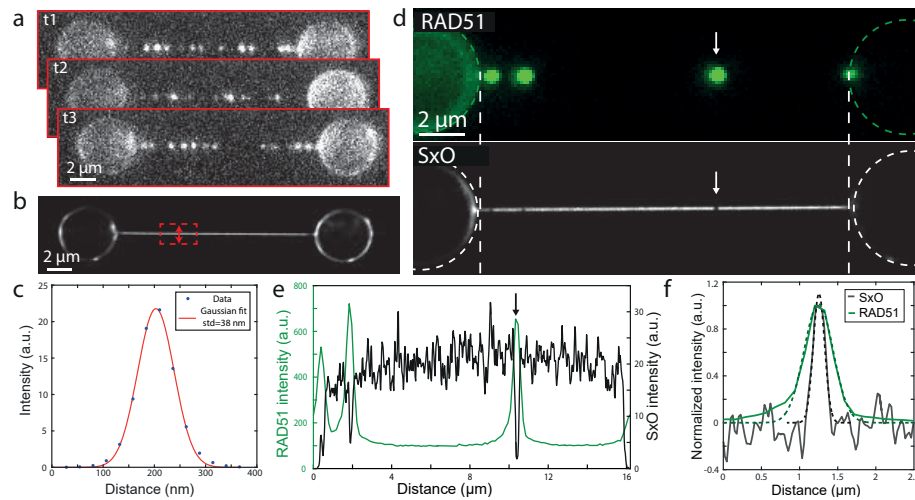
Figure 4.2: Super-resolution imaging of DNA with BALM and visualization of DNA-bound proteins with iBALM. a) Fluorescence images show individual SxO binding events on optically manipulated DNA (exposure time: 1s). b) Super-resolution reconstruction of the SxO binding events on optically manipulated DNA. c) Cross section and Gaussian fit taken perpendicular to the DNA orientation, as indicated in the super-resolved image in (b). d) Wide-field image of hRAD51-A647 filaments bound to DNA (upper) and the corresponding reconstructed super-resolution image of SxO binding to DNA (lower) accumulated over 100 minutes. e) Intensity profile along the DNA between the white dotted lines of the images in (c) show a strong correlation between hRAD51 position (green profile) and dark spots in the super-resolved SxO image (black profile). f) Comparison of the intensity profile of the diffraction-limited RAD51 signal and the inverted intensity profile of the iBALM signal, at the position indicated by the arrows in (d) and (e). The dashed lines are gaussian fits that correspond to FWHM values of 450±20 nm and 180±10 nm for the hRAD51-A647 and SxO signals, respectively.

(Figure 4.1d). This experiment demonstrates that DNA-bound hRAD51 locally suppresses intercalator binding, which is in line with our findings in fluorescent intercalator displacement experiments performed in bulk solution on unlabeled hRAD51 bound to DNA (Supplementary Figure 4.1a). Similar inverse imaging experiments were performed on the mitochondrial transcription initiation protein TFAM, revealing a clear spatial correlation of the suppressed YOPRO signal with TFAM-Alexa555 bound regions of the DNA (Supplementary Information 4 andSupplementary Figure 4.4). These experiments provide the proof of concept that spatial information on the location

of DNA-bound proteins can be retrieved through intercalator-based inverse imaging without the need to label the proteins themselves.

To further extend the concept of inverse labeling to super-resolution microscopy, we first analyzed the performance of binding-activated localization microscopy on optically manipulated DNA. Here, we employed the mono-intercalator Sytox Orange (SxO) because it has binding-event durations in the range of seconds ($k_{off}^{-1} \approx 1\ s$ at 15 pN DNA tension[9]). At nanomolar intercalator concentration, such long binding times allow us to conveniently localize the positions of individually resolved DNA-intercalation events (Figure 4.2a). The average number of photons collected per binding event per frame was 366 (1s exposure time). We reconstructed a super-resolution image of the DNA based on the localization of $\sim 5.0 \cdot 10^4$ individual SxO binding events (Figure 4.2b), which demonstrates the feasibility of BALM on optically manipulated DNA. Note that control of DNA tension (implemented here using optical tweezers) allows tuning the event duration due to the strongly DNA tension-dependent off-rate of intercalators[9]. Together with the intercalator concentration, DNA tension thus provides control over event frequency and duration, which allows convenient tuning of the spatial and temporal resolution of (inverse) localization microscopy. Additionally, we note that control of DNA tension allows suppressing the thermal fluctuations of the DNA, which may otherwise decrease the effective (super-)resolution due to motion blurring[22,29]. In the reconstructed image, the standard deviation of the DNA cross-section was 38±2 nm (corresponding to a FWHM of 90±5 nm, Figure 4.2c and Supplementary Information 2)[20,30]. Importantly, the high number of localizations acquired shows the feasibility of a dense sampling of the DNA (3 nm-1 or ~1 event per base pair), which will assist the inverse imaging of proteins and protein patches with DNA-bound footprints in the range of 5-50 nanometers.

Next, we combined the inverse labeling strategy with the principle of BALM, in order to demonstrate that we can super-resolve unlabeled proteins on DNA in an approach we call "inverse BALM" (iBALM). To this end, we again turned to dsDNA that was pre-incubated with hRAD51-A647 and used SxO for localization microscopy of DNA. In this experiment, a localization density of 1.7 nm-1 was achieved with an average localization precision of individual SxO binding events of 25 nm. The reconstructed iBALM image exhibits dark spots, comparable to those observed in the diffraction limited

experiment (cf. Figure 4.1) yet resolved at an enhanced resolution. Indeed, these super-resolved dark spots coincide with the location of hRAD51-A647 filaments on the dsDNA, as observed through direct imaging of hRAD51-A647 (Figure 4.2d,e). The observation that the SxO signal nearly vanishes at the RAD51-bound DNA indicates that RAD51 filaments indeed prevent SxO binding. The full-width at half maximum (FWHM) of the hRAD51 filament in the super-resolved iBALM image (see arrow in Figure 4.2d,e) is 180±10 nm (corresponding to 120±7 hRAD51 monomers), which is more than a factor of two better than the FWHM observed in the diffraction-limited Alexa Fluor 647 image (450±20 nm) (Figure 4.2f). The size of the hRAD51 filament that we estimated through iBALM, is in good quantitative agreement with an estimate of the number of hRAD51 monomers in the filament based on the Alexa Fluor 647 fluorescence signal, and with an estimate of the number of basepairs that are inaccessible for SxO binding based on the suppressed intercalator signal (See Supplementary Information 3). While the total image acquisition time of Figure 2d-f was 100 minutes, all RAD51 patches could already be detected after 5 minutes of imaging (using an automated detection algorithm, seeSupplementary Figure 4.2). These results demonstrate a quantitative fluorescence-based super-resolution imaging method of unlabeled protein filaments on DNA.

To obtain quantitative insights into the performance and limitations of iBALM, we performed Monte Carlo simulations of our inverse imaging approach. These simulations assume that a 1 μm long DNA molecule has a protein (patch) bound at its center. Stochastic DNA intercalation events were generated at random positions along the DNA, except at the protein-bound section (see methods). These simulated intercalation events were subsequently used to reconstruct an iBALM image (see simulated reconstructed iBALM profile, Figure 4.3a). In order to identify protein-bound DNA in the simulated iBALM profiles, we invoked an intensity threshold I_{th}, below which the DNA is considered to be bound by proteins. We calculate the intensity threshold as $I_{th} = I_{av} - N * \sigma_I$, in which I_{av} is the average intensity and σ_I is the standard deviation of the intensity. In principle, σ_I and I_{av} can be estimated through an iterative approach without prior knowledge (Supplementary Information 1), but, for simplicity, we obtained these parameters here directly from the simulated sections of bare DNA. Parameter N needs to be chosen to achieve a balanced tradeoff between false positives, correct
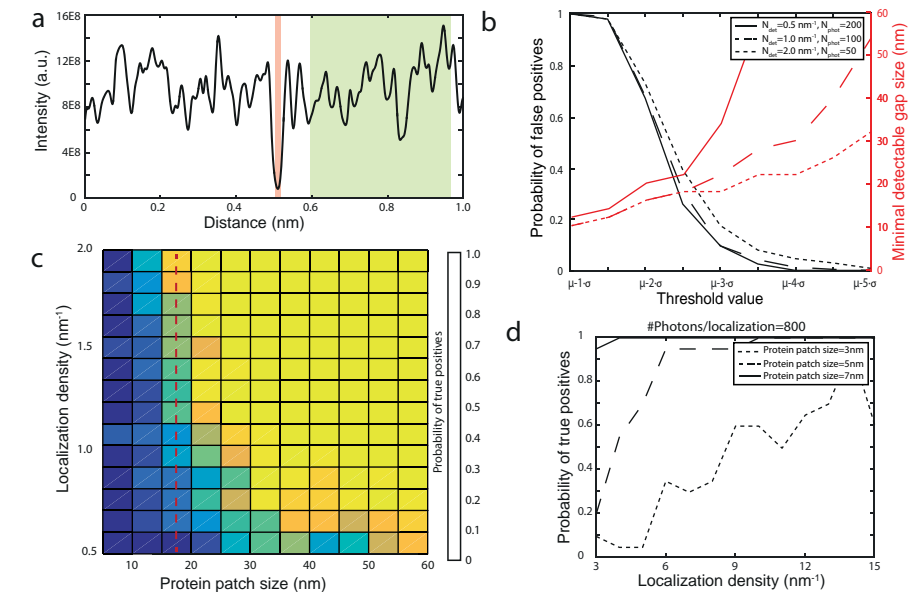

Figure 4.3: Monte Carlo simulations give insight into the performance of iBALM. a) Example of a simulated intensity profile with a localization density N_{det}=1 nm⁻¹. Red area depicts the blocked region representing a protein patch. Green region is used to determine mean and standard deviation of the intensity profile. b) Influence of the threshold value on the probability of finding false positives (black) and on the minimal detectable patch size (red). Three different combinations of localization densities were compared, while keeping the average number of photons constant at 100 per nm (continuous, dashed and dotted line). c) The probability of detecting a protein patch of varying size as a function of localization density. Color scale depicts probability of detecting true positives. The threshold parameter and number of photons per intercalator were chosen to be N=3.5 and N_{phot}=200 respectively. d) Probability of detecting small protein patches (<10nm) at a photon yield of N_{phot}=800 as a function of localization density.

detections, and the minimum detectable patch size. To quantify the impact of this tradeoff, we varied N for a range of different protein patch sizes and a range of localization densities (Figure 4.3b). In these simulated experiments, the number of detected photons was kept constant at 100 per nm DNA (methods). The following observations can be made: (i) the percentage of false positives drops sharply with increasing N. Specifically, for N=3.5, the fraction of false positives drops below 10%, independent of localization density; and (ii) increasing N further above 3.5 yields minimal improvement in false positives, while it substantially deteriorates (increases) the minimal detectable patch size, in a manner that is strongly dependent on localiza-

tion density and precision. For example, a minimum detectable patch size of 23 nm is achieved using N=3.5, at an intercalation density of 2 nm^{-1} and 50 detected photons per intercalator (corresponding to a localization accuracy of 65nm).

Next, we sought to investigate how the efficiency of detecting protein patches of varying size depends on the localization density (Figure 4.3c). To this end, a second set of simulations was performed in which the number of photons per intercalator was fixed to 200, resulting in a localization accuracy of 19 nm (for simulations of different photon counts see Supplementary Figure 4.3a). As expected, the detection efficiency increases with increasing localization density and with increasing patch size (Figure 4.3c). For example, in order to detect protein patches between 20 and 55 nm in size with a minimum efficiency of 50%, a minimal localization density of about 0.75 nm^{-1} was required. These simulations furthermore show that the smallest protein (patch) sizes that can be detected reliably is about 15 nm (dashed line), which is comparable in size to large protein complexes such as nucleosomes, DNA Polymerase or to filament-forming proteins such as RAD51. This lower limit can be further enhanced to the size of a single protein of 5 nm by increasing the number of detected photons per intercalator to 800 (corresponding to an enhanced localization accuracy of 7 nm) at an intercalator density of 10 nm^{-1} (Figure 4.3d). Taken together, these simulations indicate that, under the conditions of our iBALM experiments (localization density of 1.7 nm^{-1} and localization accuracy of 25 nm), the minimum detectable protein (patch) size is 15 nm (detection probability >90%). For RAD51, such 15 nm patch corresponds to a minimum detectable number of 10 proteins.

To explore further applications of our inverse imaging approach, we turn to the limit of high protein density, where inverse imaging may serve to quantify the length of long nucleoprotein filaments. In previous studies, the typical length of uninterrupted, defect-free hRAD51 nucleoprotein filaments on dsDNA has been measured using AFM to be on average 500 base pairs[31]. We revisited this quantification by exposing dsDNA that was saturated with hRAD51 (as confirmed by force-extension analysis and fluorescence images (Supplementary Figure 4.1bd)) to the intercalating dye YOPRO. Fluorescence imaging of YOPRO reveals a clear, sparse binding pattern of the intercalator to the hRAD51-saturated DNA (Figure 4.4a) that is distinct from the relatively homogeneous YOPRO binding pattern that we observed previously at low
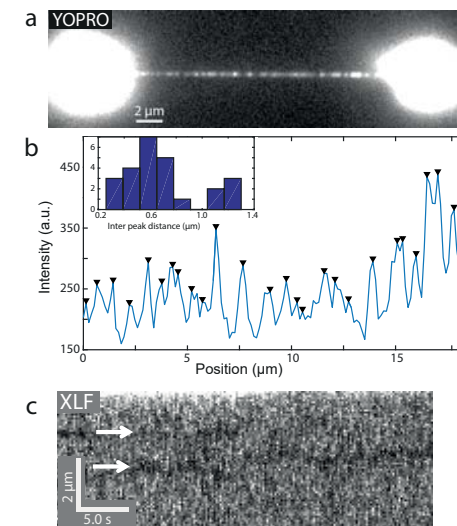
Figure 4.4: Inverse microscopy applications. a) YOPRO imaging reveals a sparse binding pattern after the DNA was saturated with hRAD51 binding (exposure time: 1s). b) Intensity profile of the fluorescence image of (a). Black triangles indicate the position of detected peaks. Inset: histogram of nearest peak distances. c) Kymograph of eGFP-labeled hXLF on optically manipulated DNA (line trace: 190ms). DNA-bound hXLF-eGFP oligomers were bleached and are visualized as dark traces (arrows) in a brighter background of transiently binding hXLF-eGFP monomers.

hRAD51 coverage (cf. Figure 4.1b). The YOPRO binding pattern of Figure 4.4a is consistent with a dense coverage of the DNA by continuous hRAD51 filaments that are interrupted by gaps where intercalators are permitted to bind to the exposed DNA. The peak-to-peak distance in the intensity profile (Figure 4.4b inset) thus provides an upper limit estimate for the hRAD51 filament length of 0.7 μm or 1.4 kbp, which is in good agreement with previous estimates from AFM data[31] (we tentatively attribute the second peak at twice the distance (Figure 4.4b inset) to a double average filament length when gaps are not picked up by our peak-finding routine). In this inverse imaging approach, the filament length could be estimated owing to the small DNA-binding footprint of intercalators of (at most) two base pairs[9]. Such small footprint allows intercalators to report on sub-nanometer gaps between hRAD51 filaments that are too small to resolve through direct imaging of fluorescently labeled hRAD51.

In another application of inverse microscopy, we aimed to visualize the one-dimensional (diffusive) motion of DNA-bound proteins along dsDNA. Since visualizing one-dimensional diffusive motion requires a temporal resolution in the order of seconds[32], we turned to diffraction-limited inverse microscopy, which is intrinsically faster than super-resolution localization microscopy because it does not require image reconstruction from a multitude of sparse images. Furthermore, we employed the human protein XLF-eGFP to label the DNA instead of using intercalators. XLF is a DNA-repair

protein that binds dsDNA intermittently as a monomer, but it can also form stable oligomers that exhibit one-dimensional diffusion along the DNA over extended periods of time[25]. After continued exposure of such bound oligomers to fluorescence excitation, their fluorophores photo-bleach, leaving 'dark' complexes that are essentially representative of unlabeled complexes bound to DNA. Laser-scanning confocal fluorescence microscopy can subsequently report on the transient binding mode of monomeric hXLF-eGFP to the DNA that surrounds such dark complexes. Indeed, kymographs obtained under such conditions clearly show dark regions of DNA, which we associate with larger photobleached hXLF-eGFP complexes that locally suppress transient binding of hXLF-eGFP monomers to the DNA (Figure 4.4c, temporal resolution is 190 ms). In support of this hypothesis, the dark spots exhibit one-dimensional diffusion along the stretched DNA with a diffusion constant $D=0.058\pm0.008$ $\mu m^2/s$ (see Supplementary Figure 4.3b,c), consistent with the previously determined diffusion constant in the range of D=0.05 to 0.5 $\mu m^2/s$ for large XLF complexes[25]. These last results showcase not only the versatility of the inverse imaging approach to report on spatial dynamics, but also the generality of the approach beyond the use of DNA-intercalators as inverse labels.

4.5 Discussion

In this study we have demonstrated an inverse imaging method that is capable of (super-)resolving unlabeled protein patches bound to DNA. This method is related to fluorescent intercalator displacement (FID) assays[15,16], but with the significant benefit that spatially resolved information of unlabeled proteins can be retrieved by registration of the local absence of fluorescence. In order to correctly assign a local lack of fluorescence to bound proteins, knowledge of DNA location is required, which, in our experiments, is accomplished through optical manipulation, but other methods can be envisioned such as the use of surface-bound DNA or DNA curtains, DNA in nanofluidic confinement, or by flow-stretching DNA.

DNA intercalators appear to be well suited for our inverse imaging approach: intercalators facilitate essentially background-free imaging because of their 2-3 orders of magnitude fluorescence enhancement upon DNA intercalation. Moreover, a range of well-characterized intercalators with a small DNA-binding footprint is commercially available[9], which makes it possible to

quantitatively estimate the number of base pairs covered by the unlabeled proteins (Supplementary Figure 4.1 & Supplementary Information 3). A possible concern of using intercalators is their potentially perturbing effect on DNA structure and on enzymatic reactions[9]. However, such perturbation has been well-characterized and can be minimized through experimental design: Through proper choice of DNA tension, intercalator and salt concentration, the DNA-binding kinetics and affinity can be tuned over ~7 orders of magnitude and, for example, achieve low coverage (e.g. <1%) or high off-rates to minimize perturbation (provided that such salt concentration and tension is compatible with the DNA-protein interaction of interest)[9]. While most of our experiments indeed focused on using DNA intercalators, we also demonstrated our inverse imaging approach using non-intercalating probes. In principle, any DNA-binding dye can be used as long as it competes with the protein of interest for DNA-binding sites. Labels suitable for inverse imaging should ideally bind DNA transiently while minimally perturbing it.

A common problem for fluorescence-based approaches is photobleaching. Inverse imaging, much like PAINT[33], circumvents photobleaching problems by continuously drawing new labels from bulk solution in order to report on the features of interest (e.g. bare DNA). Bleaching followed by photo-nicking of DNA, which can result in DNA breaks, on the other hand, can be problematic. This is particularly relevant for intercalators since their chromophoric systems interact strongly with the DNA. In our hands, photo-induced DNA breaks indeed limited the total duration of an experiment. Several approaches may be taken to suppress this photo-nicking problem and increase experiment duration or photon yield, such as the use of reducing and oxidizing reagents[34].

The ability of inverse imaging to retrieve spatially resolved information on molecular structures without the need to label the proteins of interest themselves sets the method apart from other fluorescence-based imaging approaches. Other label-free imaging methods such as second and third harmonic generation exist, but these are restrictive in the proteins/structures that yield contrast. Inverse imaging, on the other hand, can be used to image any DNA-binding protein. While this makes the method versatile, a lack of specific contrast also requires judicious experimental design in order to enable correct interpretation of inverse images. A label-free technique such as iSCAT gains some specificity by quantifying molecular weight[5]. On

the other hand, scattering-based techniques such as iSCAT cannot make use of conventional super-resolution methods that rely on switching between bright and dark states.

We demonstrated super-resolution imaging of unlabeled protein patches through inverse binding-activated localization microscopy (iBALM). The high sampling density that is required for iBALM causes super-resolution imaging to be comparatively slow. We showed that much higher temporal resolution can be achieved through beam-scanning confocal (diffraction limited) imaging of XLF-eGFP as DNA-labeling molecule. Similarly high time resolution may be achieved in super-resolution inverse imaging by employing beam-scanning (1D) STED imaging of intercalating dyes (e.g. Sytox Red, cf. 22).

We envision wide applications for inverse imaging and iBALM approaches. Although we have focused on imaging isolated DNA strands, one could also imagine quantitative imaging of regions of variable DNA accessibility in chromosomes[35]. Furthermore, these inverse imaging principles may be applied to systems other than DNA, including the cytoskeleton (e.g. microtubules)[36] and two- or three-dimensional structures like lipid surfaces[37]. We consider inverse imaging and iBALM to be valuable additions to the single-molecule toolkit that can complement existing methods and relieve potential limitations posed by labeling in a wide range of applications.

4.6   Supplementary information

Supplementary information 1: Threshold determination without prior knowledge of protein patch location
The method to determine the position of a protein patch as suggested in the main text relies on determination of the threshold based on the fluorescence intensity on a bare piece of DNA. This method requires either a control experiment without protein or prior knowledge of the protein patch position. We suggest here an alternative method to determine the threshold that does not require prior knowledge of the protein patch position or a control experiment. We propose to calculate the threshold on the full length of the DNA and then iteratively discarding the data points and corresponding regions within the localization uncertainty[24] that fall below the threshold $I_{th} = I_{av} - N * \sigma_I$ and calculating the threshold again until it converges to a constant value. This constant value is obtained without prior knowledge of the protein patch position and can now be used to determine where the protein patches are located. It has to be noted that this iterative method only works on sparsely coated DNA.

Supplementary Information 2: Resolution estimate using DNA cross section analysis
As an estimate of the acquired resolution of our BALM experiments, we determined the average width of the cross section along the DNA (Figure 4.2b). To this end, we selected five 1 μm long sections along the DNA and determined the width of these five cross-sections by fitting a Gaussian. This yielded an average FWHM of 90±5 nm. It has to be noted that this cross section might be an upper-limit of the resolution because of instrumental drift, which was estimated to be 50 nm perpendicular to the DNA during the course of the experiment.

Supplementary Information 3: Comparison of three approaches to estimate hRAD51 filament length

In order to compare the estimate of the hRAD51 filament length that was observed using iBALM, we employed three methods and find similar results. First, we estimated the number of hRAD51-A647 monomers present in the filament from the fluorescence intensity of the control image (Figure 4.2D, top panel). In order to quantify the fluorescence intensity from a single hRAD51-A647 molecule, we analyzed the bleaching steps that are observed after prolonged exposure to the excitation light. A total number of 100 hRAD51-A647 monomers was estimated to be present in the filament of Figure 2 (cf. arrow in Figure 4.2D). Assuming a labeling ratio of 1, and a hRAD51 DNA-binding footprint of 3 bp, corresponding to 1.5nm length[41], we estimate a filament length of 150 nm.

Secondly, we estimated the DNA length that was inaccessible for intercalator binding by determining the suppressed intercalator signal from the wide-field imaging data. To this end, we summed the intensity of all intercalator binding events and perform a background correction based on the fluorescence intensity in absence of intercalator binding events. The area (intensity x distance) under the intensity curve was compared between a region with and without hRAD51 filament present (Supplementary Figure 4.1c). The lack in intercalator signal in the hRAD51 filament region was converted to a distance by assuming complete blockage of intercalator binding along the filament length. This leads to an estimate of 220 nm DNA length that was unoccupied by intercalators. Finally, the above two fluorescence-intensity-based quantifications of the size of the hRAD51 filament are in good agreement with the FWHM of the super-resolved image, which was found to be 180 ± 10 nm (cf. Figure 4.2F).
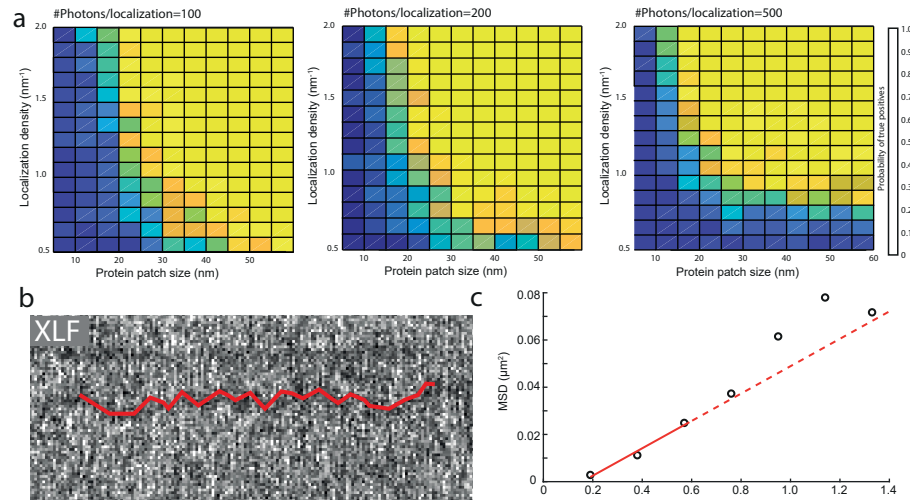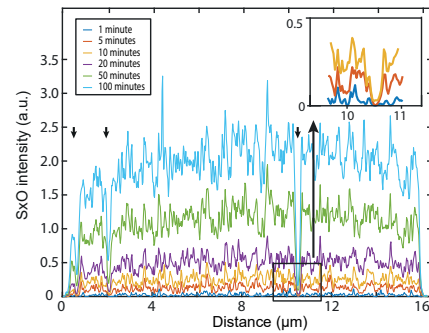
Supplementary Information 4: inverse imaging of TFAM

In an assay comparable to that ofFigure 4.1, we imaged the mitochondrial transcription initiation protein TFAM bound to DNA and compared these with images of YOPRO binding (Supplementary Figure 4.4a-d). Similarly to the results with hRAD51, TFAM-Alexa555 bound regions of the DNA correlated with suppressed YOPRO signal. Indeed, the intensity profile of the TFAM signal is spatially correlated with the inverted intensity profile of YOPRO binding. (cf. Supplementary Figure 4.4b,d).

4.7   Supplementary Figures
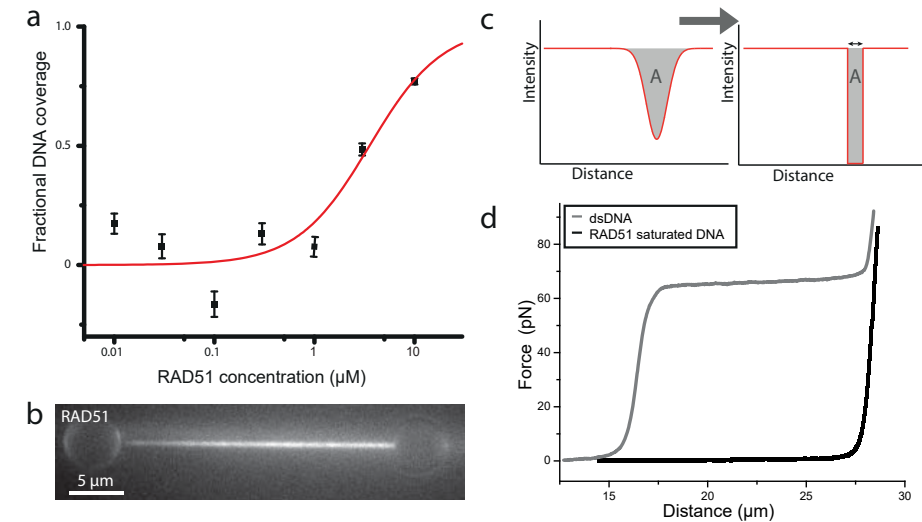
Supplementary Figure 4.1: a) Fluorescent intercalator displacement assay using normalized intercalator fluorescence to report unlabeled hRAD51 binding to DNA. b) Fluorescence imaging of hRAD51-A647 shows a homogenously coated DNA strand, indicating DNA saturation by hRAD51. c) Method to determine hRAD51 filament length by comparing the lack of intercalator fluorescence signal and converging that to an estimated region that is inaccessible for intercalator binding. d) Force-distance curves of bare DNA (grey) and DNA that is saturated by hRAD51 binding (black). The absence of an overstretching plateau and a ~1.7-fold increase in contour length of the hRAD51-coated DNA, compared to that of bare DNA, indicates saturated coverage of the DNA by hRAD51[30].

Supplementary Figure 4.2: Time evolution of the super resolution image of Figure 2d-f. Arrowheads indicate the location of hRAD51 patches. Inset shows a zoom in on one of the hRAD51 locations showing that after 5 minutes the hRAD51 patch can be localized due to a dip in the super resolved image. The iterative threshold determination as described in Supplementary Information 1 successfully finds all three hRAD51 patches after 5 minutes of imaging.

Supplementary Figure 4.4: a,c) Wide-field fluorescence images of DNA-bound TFAM (upper) and corresponding images of YOPRO binding (lower). b,d) Intensity profile of TFAM from (a,c) after background correction shows a correlation with the inverted intensity profile of YOPRO binding.

Supplementary Figure 4.3: a) The probability of detecting a protein patch of varying size as a function of localization density for three different values of photons per localization. Color scale depicts probability of detecting true positives. At localization densities of more than 1.0 nm-1 increasing values of photons per localization enable detection of smaller protein patches. b) Kymograph of hXLF-eGFP bound to dsDNA and in red the depiction of manual tracking of a bleached hXLF oligomer. c) Mean-squared-displacement analysis of a hXLF oligomer bound to DNA. Linear fitting to the first three MSD values (red line) results in an estimate of the diffusion constant of D=0.058±0.008 µm²/s.

References

1.   Huang, B., Bates, M. & Zhuang, X. Super-Resolution Fluorescence Microscopy. Annu. Rev. Biochem. 78, 993–1016 (2009).
2.   Lichtman, J. W. & Conchello, J. A. Fluorescence microscopy. Nat. Methods 2, 910–919 (2005).
3.   Wang, S., Moffitt, J. R., Dempsey, G. T., Xie, X. S. & Zhuang, X. Characterization and development of photoactivatable fluorescent proteins for single-molecule-based superresolution imaging. Proc. Natl. Acad. Sci. 111, 8452–8457 (2014).
4.   Freudiger, C. W. et al. Label-Free Biomedical Imaging with high sensitivity by stimulated raman scattering microscopy. Science (80-.). 322, 1857–1861 (2008).
5.   Ortega-Arroyo, J. & Kukura, P. Interferometric scattering microscopy (iSCAT): new frontiers in ultrafast and ultrasensitive optical microscopy. Phys. Chem. Chem. Phys. 14, 15625–15636 (2012).
6.   Cole, D., Young, G., Weigel, A., Sebesta, A. & Kukura, P. Label-Free Single-Molecule Imaging with Numerical-Aperture-Shaped Interferometric Scattering Microscopy. ACS Photonics 4, 211–216 (2017).
7.   Simmert, S. et al. LED-based interference-reflection microscopy combined with optical tweezers for quantitative three-dimensional single microtubule imaging. Opt. Express 26, 14499–14513 (2018).
8.   Glazer, A. N. & Rye, H. S. Stable dye-DNA intercalation complexes as reagents for high-sensitivity fluorescence detection. Nature 359, 859–861 (1992).
9.   Biebricher, A. S. et al. The impact of DNA intercalators on DNA and DNA-processing enzymes elucidated through force-dependent binding kinetics. Nat. Commun. 6, 1–12 (2015).
10.   Perkins, T. T., Smith, D. E. & Chu, S. Single Polymer Dynamics in an Elongational Flow. Science (80-.). 276, 2016–2021 (1997).
11.   Glazer, A. N., Peck, K. & Mathies, R. A. A stable double-stranded DNA-ethidium homodimer complex: application to picogram fluorescence detection of DNA in agarose gels. Proc. Natl. Acad. Sci. 87, 3851–3855 (1990).
12.   Bianco, P. R. et al. Processive tanslocation and DNA unwinding by individual RecBCD enzyme molecules. Nature 409, 374–378 (2001).

4

13. Finkelstein, I. J., Visnapuu, M. L. & Greene, E. C. Single-molecule imaging reveals mechanisms of protein disruption by a DNA translocase. Nature 468, 983–987 (2010).

14. Hamdan, S. M., Loparo, J. J., Takahashi, M., Richardson, C. C. & Van Oijen, A. M. Dynamics of DNA replication loops reveal temporal control of lagging-strand synthesis. Nature 457, 336–339 (2009).

15. Zaitsev, E. N. & Kowalczykowski, S. C. Binding of double-stranded DNA by Escherichia coli RecA protein monitored by a fluorescent dye displacement assay. Nucleic Acids Res. 26, 650–654 (1998).

16. Boger, D. L., Fink, B. E., Brunette, S. R., Tse, W. C. & Hedrick, M. P. A simple, high-resolution method for establishing DNA binding affinity and sequence selectivity. J. Am. Chem. Soc. 123, 5878–5891 (2001).

17. Betzig, E. et al. Imaging Intracellular Fluorescent Proteins at Nanometer Resolution. Science (80-.). 313, (2006).

18. Rust, M. J., Bates, M. & Zhuang, X. Sub-diffraction-limit imaging by stochastic optical reconstruction microscopy (STORM). Nat. Methods 3, 793–795 (2006).

19. Willig, K. I., Rizzoli, S. O., Westphal, V., Jahn, R. & Hell, S. W. STED microscopy reveals that synaptotagmin remains clustered after synaptic vesicle exocytosis. Nature 440, 935–939 (2006).

20. Schoen, I., Ries, J., Klotzsch, E., Ewers, H. & Vogel, V. Binding-activated localization microscopy of DNA structures. Nano Lett. 11, 4008–4011 (2011).

21. Mortensen, K. I., Churchman, L. S., Spudich, J. A. & Flyvbjerg, H. Optimized localization analysis for single-molecule tracking and super-resolution microscopy. Nat. Methods 7, 377–381 (2010).

22. Heller, I. et al. STED nanoscopy combined with optical tweezers reveals protein dynamics on densely covered DNA. Nat. Methods 10, 910–916 (2013).

23. Gross, P., Farge, G., Peterman, E. J. G. & Wuite, G. J. L. Combining Optical Tweezers, Single-Molecule Fluorescence Microscopy, and Microfluidics for Studies of DNA–Protein Interactions. Methods Enzymol. 475, 427–453 (2010).

24. Brouwer, I. et al. Two distinct conformational states define the interaction of human RAD51-ATP with single-stranded DNA. EMBO J. 37, (2018).

25. Brouwer, I. et al. Sliding sleeves of XRCC4-XLF bridge DNA and connect fragments of broken DNA. Nature 535, 566–569 (2016).

26. King, G. A. et al. Acetylation and phosphorylation of human TFAM regulate TFAM-DNA interactions via contrasting mechanisms. Nucleic Acids Res. 46, 3633–3642 (2018).

27. van Mameren, J. et al. Dissecting Elastic Heterogeneity along DNA Molecules Coated Partly with Rad51 Using Concurrent Fluorescence Microscopy and Optical Tweezers. Biophys. J. 91, L78–L80 (2006).

28. Hilario, J., Amitani, I., Baskin, R. J. & Kowalczykowski, S. C. Direct imaging of human Rad51 nucleoprotein dynamics on individual DNA molecules. PNAS 106, 361–368 (2009).

29. Candelli, A., Wuite, G. J. L. & Peterman, E. J. G. Combining optical trapping, fluorescence microscopy and micro-fluidics for single molecule studies of DNA-protein interactions. Phys. Chem. Chem. Phys. 13, 7263–7272 (2011).

30. Backer, A. S., Lee, M. Y. & Moerner, W. E. Enhanced DNA imaging using super-resolution microscopy and simultaneous single-molecule orientation measurements. Optica 3, 659–666 (2016).

31. Ristic, D. et al. Human Rad51 filaments on double- and single-stranded DNA: Correlating regular and irregular forms with recombination function. Nucleic Acids Res. 33, 3292–3302 (2005).

32. Vestergaard, C. L., Blainey, P. C. & Flyvbjerg, H. Optimal estimation of diffusion coefficients from single-particle trajectories. Phys. Rev. E - Stat. Nonlinear, Soft Matter Phys. 89, (2014).

33. Schnitzbauer, J., Strauss, M. T., Schlichthaerle, T., Schueder, F. & Jungmann, R. Super-resolution microscopy with DNA-PAINT. Nat. Protoc. 12, 1198–1228 (2017).

34. Vogelsang, J. et al. A reducing and oxidizing system minimizes photobleaching and blinking of fluorescent dyes. Angew. Chemie - Int. Ed. 47, 5465–5469 (2008).

35. Deng, W., Tsao, S. W., Lucas, J. N., Leung, C. S. & Cheung, A. L. M. A new method for improving metaphase chromosome spreading. Cytometry 51A, 46–51 (2003).

36. Bailey, M., Conway, L., Gramlich, M. W., Hawkins, T. L. & Ross, J. L. Modern methods to interrogate microtubule dynamics. Integr. Biol. (United Kingdom) 5, 1324–1333 (2013).

37. Owen, D. M. & Gaus, K. Imaging lipid domains in cell membranes: The advent of super-resolution fluorescence microscopy. Front. Plant Sci. 4, 1–9 (2013).

4

Exposing chromosome mechanics and architecture using optical manipulation and fluorescence microscopy

A.E.C. Meijering, K. Sarlos, C.F. Nielsen, H. Witt, J. Harju, E. Kerklingh, G.H. Haasnoot, A.H. Bizard, I. Heller, Y. Liu, C.P. Broedersz, E.J.G. Peterman, I.D. Hickson and G.J.L. Wuite.
In preparation

5.1   Abstract

During cell division, DNA is compacted by about four orders of magnitude in length to form X-shaped mitotic chromosomes. While several proteins essential for this process, such as Condensin I & II and Topoisomerase IIα (TOP2A), have been identified, the spatial organization of mitotic chromosomes remains elusive, due to difficulties of visualizing the structure of chromatin and of controlling experimental conditions in living cells. To overcome these challenges, we have developed a method to optically manipulate isolated mitotic chromosomes, enabling high-resolution force measurements and fluorescence visualization of the chromosomal structure under controlled experimental conditions. We use this method to assess chromosome mechanics and to investigate the structural role of TOP2A with a spectrum of approaches including force-extension analysis, microrheology-like oscillatory experiments, salt-induced chromosome swelling and immuno-fluorescence imaging of non-fixed chromosomes. Remarkably, we find that, under increasing mechanical load, chromosomes exhibit robust anomalous stiffening behavior. We introduce a Hierarchical Worm-like Chain (HWLC) model to describe the chromosome as a heterogeneous assembly of nonlinear mechanical elements that behave as WLCs. In this model, the hierarchy of nonlinear mechanical behaviors, gives rise to a weaker stiffening exponent by the successive stiffening of the internal components in the heterogeneous chromosome. In line with this picture, we find that upon TOP2A depletion the anomalous stiffening behavior is retained, albeit with an even weaker scaling exponent. Interestingly, the reversibility of salt-induced expansion and compaction of chromosomes is disrupted upon TOP2A depletion, providing further support for the structural role for this protein in the mitotic chromosome. Our results demonstrate the strength of highly controlled mechanical assessment to come to a quantitative description of chromosome mechanics. We anticipate that our method will be a starting point for further investigations on the chromosomal structure and the role of specific proteins therein.

5.2   Introduction

Eukaryotic chromosome structure changes dramatically throughout the cell cycle. In interphase, chromosomes appear to have a disperse shape and individual chromosomes are not readily distinguishable. As cells enter mitosis, the replicated chromosomes condense into compact, cylindrical structures that are segregated over the daughter cells by the mitotic spindle. Forces applied to chromosomes by the mitotic spindle during cell division have been estimated to be in the order of hundred piconewton [1,2]. It is therefore not surprising that interference with the compacted structure of the mitotic chromosome often leads to unfaithful chromosome segregation, DNA damage or mitotic exit [3].

It is thought that the structure of the condensed chromosome is crucial for withstanding such forces, enhancing robustness of chromosome segregation. Electron-microscopy studies have revealed the presence of a series of DNA loops emanating from a central core along the chromosome arms. These observations have led to a model of chromosome organization where consecutive loops of chromatin are anchored to a central protein scaffold [4]. Key players in obtaining this organization are thought to be ring-shaped 'condensin' SMC (structural maintenance of chromosomes) complexes, which extrude DNA loops forming a radial loop structure [5], together with Topoisomerase IIα (TOP2A) [6,7], which can resolve DNA catenations. Condensins have been shown to be essential for the formation and maintenance of mitotic chromosomes both in vivo [8] and in vitro [9], whereas TOP2A has a crucial role for mitotic chromosome formation in vitro and in vivo [10,11], but its role for maintenance of the structure is under debate [12]. Moreover, how the collective action of these proteins leads to large-scale organization of mitotic chromosomes remains poorly understood.

In the past decades, molecular architectures of biomolecules and biomolecular complexes have been studied with great success using micromechanical measurements (atomic force microscopy, magnetic and optical tweezers) [13]. In this light, remarkably few of such mechanical studies have been performed on chromosomes. A landmark study manipulating chromosomes in vivo with a micropipette revealed that chromosomes experience an estimated force of several hundred piconewton during anaphase, which estimate was later confirmed by fluorescence reporter experiments [1,2]. A series of studies focused on the mechanical stability of chromosomes, by

5

aspirating chromosomes from both ends with two micropipettes in vitro and subsequently stretched them [14–16]. These studies have shown that both newt and human chromosomes can be reversibly stretched in a linear fashion up to 5 times their native length applying forces in the nanonewton range. Follow-up investigations have for example shown that condensin depletion results in decreased chromosome stiffness [17]. These studies have sparked further questions about the chromosomal structure: what is the architecture that governs such a robust force response? And what is the role of the several key proteins in obtaining and maintaining that architecture? Although current approaches to study chromosomes including Hi-C, fluorescence microscopy, and simulations have revealed a wealth of information on chromosome architecture, they do not allow for active control and manipulation of the chromosome structure. In order to assess chromosome structure and dynamics in more detail, it is vital to develop methodologies that provide control over chromosome environment in combination with high force resolution, high throughput and the possibility for high-resolution fluorescence microscopy.

Here, we present a method that allows for the investigation of chromosomal architecture using the combination of optical tweezers, fluorescence microscopy and microfluidics to manipulate isolated human mitotic chromosomes with nanometer precision and measure the applied forces with piconewton resolution. We show that we can routinely characterize the force response from isolated, non-fixed mitotic chromosomes and assess their mechanical properties using approaches including force-extension analysis, microrheology-like oscillatory measurements and single-molecule immuno-fluorescence imaging. Our results reveal the viscoelastic response of chromosomes which show a robust strain-stiffening behavior that deviates from classical polymer models. Based on these observations, we propose a model that captures the heterogeneous structure in the form of an assembly of components with a hierarchy of nonlinear behaviors; the successive stiffening of these non-linear components combine to result in the anomalous large-scale stiffening behavior of the chromosome as a whole. In the light of this model, we investigated the role of the most abundant chromosome scaffold protein, TOP2A and found that TOP2A degradation has a strong effect on the memory of the chromosomal structure arguing for a structural role of TOP2A in the chromosome architecture. Together, the development

of this new approach allows for unprecedented micromechanical and visual assessment of mitotic chromosome architecture and the role of specific proteins therein.

5.3   Results

5.3.1   Site-specific biotinylation and attachment of mitotic chromosomes

In order to handle metaphase chromosomes in optical tweezers it is required to (i) have specific biotin handles in order to bind them to optically trapped streptavidin-coated microspheres and to (ii) obtain them in highly purified conditions with all architectural proteins present. Hence, we set out to develop chromosomes with biotinylated telomeres. Site-specific biotinylation was achieved using a previously reported method, in which constitutively active BirA was fused to telomere repeat-binding factor 1 (TRF1)[18]. Growing U2OS BirA-TRF1 cells or HCT116 cells transduced with lentivirus in the presence of biotin results in pan-telomeric biotinylation (Methods) (Figure 5.1a). Fluorescence imaging of chromosome spreads of U2OS-BirA-TRF1 cells incubated with Alexa Fluor 568 streptavidin (Supplementary Figure 5.1a) confirms that 96% of the cells (n_{total} =66) have biotin incorporation of which 98% of the telomeres (n_{total} =1434) are specifically biotinylated. Next, we optimized a chromosome isolation protocol using a modified version of an existing chromosome isolation method[19] that yielded highly concentrated and pure mitotic chromosomes devoid of cell debris (Methods). A typical sample contains 10^5-10^6 chromosomes/ml, a concentration sufficiently high for use in our microfluidic flow cell.

5.3.2   Chromosome attachment and visualization

For optical tweezers assays, individual chromosomes need to be attached between microspheres inside the microfluidic flow cell used in our dual-trap optical tweezers instrument[20]. To that end we developed a novel workflow (Figure 5.1b and Supplementary Figure 5.1b). First, two streptavidin-coated microspheres (diameter: 4.6 μm) are trapped in two independent optical traps; one of the trapped microspheres is brought in close proximity to a chromosome in solution (detected by bright-field imaging), resulting in
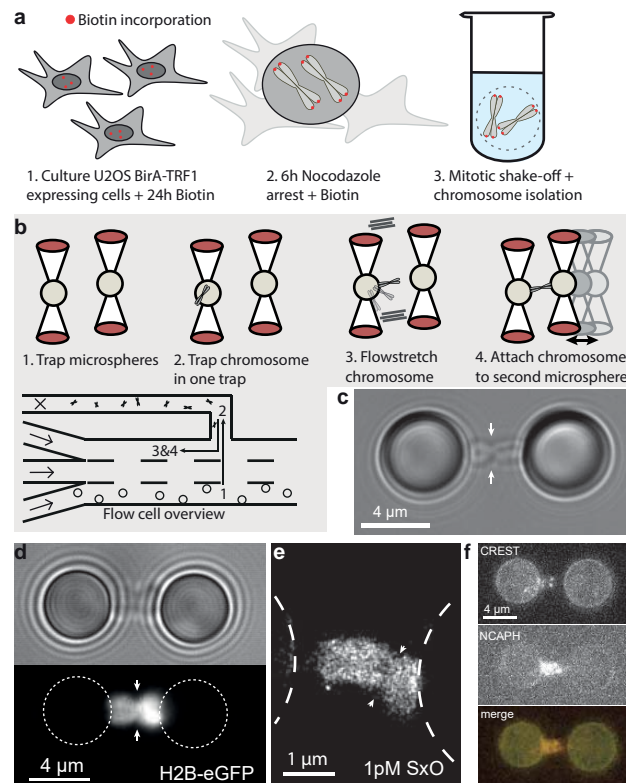
Figure 5.1: Chromosome attachment and visualization. a) Upon addition of biotin to U2OS cells expressing BirA-TRF1, biotin is incorporated around the telomeres of chromosomes. The concentration of mitotic cells is enhanced upon addition of 4h Nocodazole. Mitotic cells are harvested by shaking and chromosomes are isolated from cells by application of mechanical shear stress to disrupt the cell membrane. b) Schematic of chromosome attachment to microspheres in a microfluidic flow cell with parallel channels (below). After trapping two streptavidin coated microspheres (1), a chromosome is attached to one microsphere by exploitation of the radiation pressure of the optical trap that the chromosome experiences (2). In one of the main channels of the flow cell, the chromosome gets flow stretched (3) and attached to the second microsphere (4). c) Bright-field image of mitotic chromosomes show telomeric attachment of four arms. The centromeric region is discernable by an indentation of the chromosome (arrows). d) Fluorescence of H2B-eGFP (bottom) and corresponding bright-field (top) image. e) BALM super resolved image of SxO binding events. Centromeric region is depicted by arrowheads. f) Immuno-staining of NCAPH and CREST shows localization of Condensin I along the chromatids and two foci that reveal the position of the centromeres.

the attraction of the chromosome by the radiation pressure of the optical trap. Incubating chromosome and microsphere together in the trap for ~10 seconds, results in robust attachment of the telomeric end of the chromosome to the microsphere (Supplementary Figure 5.1b). Next, the microspheres are moved to another microfluidic channel containing only buffer and the flow in the microfluidics system is switched on (Figure 5.1b). The chromosome attached to one of the microspheres is flow-stretched to assess correct attachment (~80% of chromosomes were attached with one end of the chromosome, 20% with both ends in a "hugged" conformation on the bead, Supplementary Figure 5.1c). If the chromosome is correctly attached, it is brought into close proximity of the second microsphere to induce attachment. Note that due to the relatively small cross-section of chromosomes compared to the microspheres, we expect that chromosomes attach to microspheres with the telomeres from both sister chromatids. Proper attachment of the chromosomes to both microspheres is inspected with bright-field imaging, which provides enough contrast to recognize the parallel chromatids and the centromeric region (Figure 5.1c). In order to investigate the specificity of the biotin-streptavidin bonds, we attempted to attach chromosomes isolated from a U2OS WT cell line, without the BirA-TRF1 fusion protein. Non-specific attachment of these chromosomes to both microspheres occurs only in 6% of the attempts (n_{total}=17), compared to 88% with the U2OS-BirA-TRF1 chromosomes (n_{total} =25) (Supplementary Figure 5.1d). Taken together, these results show that we have developed an efficient workflow for the specific and stable telomeric attachment of the chromosomes between two microspheres held in two optical traps.

Having established attachment of mitotic chromosomes to microspheres kept in two optical traps, we first aimed to expand on the toolbox of chromosome visualization. We set out to image eGFP-labeled histone H2B using epi-illuminated wide-field fluorescence imaging. In fluorescence images of these chromosomes, the chromatids and centromeric region can be readily discriminated (Figure 5.1d). In addition, we used DNA-binding intercalators to fluorescently label optically trapped chromosomes. To this end we move the chromosomes to a flow channel in our microfluidic flow cell containing YO-PRO-1 (YOPRO). This results in bright chromosome images, with the chromosome appearing homogeneously stained (Supplementary Figure 5.1e). Next, we used BALM super-resolution imaging [21] of the chromosome, by localizing

individual SytoxOrange (SxO) intercalator fluorophores intermittently binding to the chromosome to get a more detailed view of the trapped chromosomes. Such BALM images (Figure 5.1e) reveal that the localization density in the centromeric region and in between the chromatids appears lower, albeit to a lesser extent than in the H2B-eGFP images (Figure 5.1d), respectively, because of the high protein density at the centromere precluding SxO binding and the absence of DNA in between the arms.

In order to investigate the presence and location of specific proteins we explored if immunostaining can be used as a flexible, yet specific labeling approach for isolated non-fixed chromosomes. To circumvent fixation and thereby preserve native chromosome structure, we developed a workflow where chromosomes were successively incubated with primary and secondary antibodies and cleared from free antibodies by dilution and centrifugation on a glycerol cushion, before introducing them in the flow cell for optical trapping (Methods). We first incubate with antibodies against histone H3, which is expected to be distributed similarly along the chromosome as H2B used above. Indeed, images of immunostained H3 (Supplementary Figure 5.1f) look qualitatively similar to those of eGFP-H2B (Figure 5.1d). Next, we used antibodies against NCAPH, a subunit of Condensin I, which localizes along the central scaffold of the chromosome arms [9]. Although strong localization to a central scaffold is not evident in the images (Supplementary Figure 5.1g), a clear Condensin I depleted region can be seen in between the chromatids and in the centromeric region as expected [22]. Finally, we explore multi-color immuno-fluorescence labeling using simultaneously antibodies against centromeric proteins CREST and NCAPH. Double-stained chromosomes show NCAPH fluorescence over the whole length of the chromosomes and, depending on the orientation of the chromosome with respect to the imaging plane, either one or two bright spots at the location of the centromeres (Figure 5.1f and Supplementary Figure 5.1h). These three different fluorescence imaging strategies for optically manipulated chromosomes can be used as a tool to assess chromosome integrity and provide the flexibility and specificity that is needed to address questions regarding the internal structure of mitotic chromosomes.

5.3.3
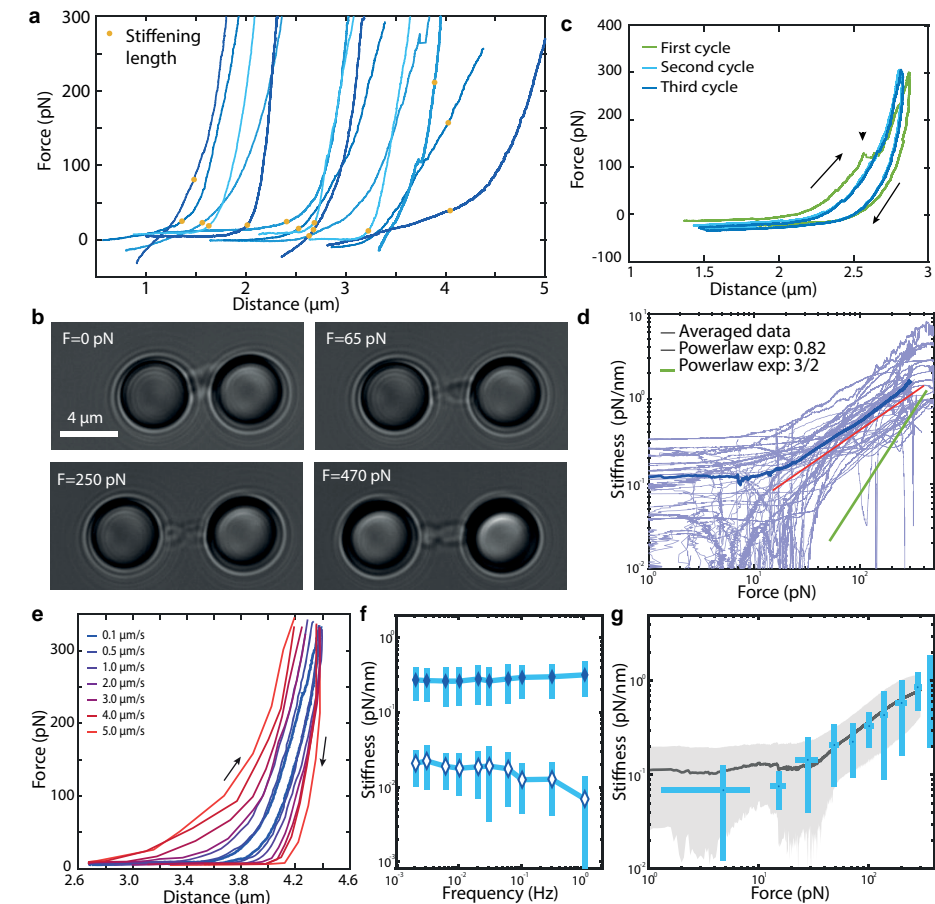
Figure 5.2: Mechanical characterization of U2OS chromosome stretching. a) Representative series of force-extension curves depict a linear stiffness regime for low forces (F<10 pN) and a non-linear stiffness regime (F>20 pN) where the stiffness of the chromosomes increases with force. Stiffening lengths are indicated with dots. b) Bright-field images of stretching a U2OS chromosome. c) Three consecutive cycles of elongation and retraction (direction depicted by arrows) of a chromosome to 300 pN. Small rupture event is depicted by arrowhead. d) Individual differential stiffness curves (light blue) and average curve (blue) show a linear stiffness regime up to around 10 pN followed by power-law scaling in the regime between 20 to 200pN with a scaling factor of γ=0.82±0.05 (red line). Green line depicts scaling of 3/2 as is expected for a WLC. e) Chromosome stretching at increasing rates shows transition to rate dependent hysteresis at rates above 0.5 μm/s. f) The storage modulus (filled diamonds) and loss modulus (open diamonds) determined at a force of 50 pN are relatively constant over three orders of magnitude. The loss modulus (open diamonds) is at least an order of magnitude smaller than the storage modulus. g) The average values (dots) and error bars (SEM) from the oscillation data measured at 1 Hz, overlapped with the differential stiffness derived from force-extension experiments (grey line: mean, grey region: SEM).

### 5.3.4 Mechanical characterization of mitotic chromosomes

Having laid the foundation for high-resolution micromanipulation and imaging of mitotic chromosomes, we set out to investigate chromosome architecture by characterizing their mechanical properties over a broad range of forces. Specifically, we measured force-extension curves by elongating chromosomes at a slow rate (<0.02 μm/s) as we separate the two traps while recording the force acting on the microspheres (Figure 5.2ab). In the low force regime (up to 10 pN), the force-extension behavior is linear, albeit with a large variability in initial stiffness. Beyond a characteristic elongation, the chromosomes display a surprisingly similar, dramatic increase in the force, reflecting a transition to non-linear stiffening of the chromosome. As a measure for chromosome length, we determined the characteristic elongation for the onset of stiffening for all chromosomes (Methods). Interestingly, this stiffening length shows a relatively broad distribution, comparable for both the U2OS and HCT116 chromosomes ($2.5 \pm 0.2\ \mu m$ and $2.8 \pm 0.3\ \mu m$ respectively, Supplementary Figure 5.2a). This variability may reflect the five-fold difference in number of base pairs between the smallest and largest chromosomes of the human genome. Despite the variability in initial stiffness and the stiffening length, the nonlinear force-extension curves show a remarkably similar general trend of increasing stiffness.

Next, we tested the reversibility of their mechanical response. The force-extension response of the majority of the chromosomes (~90%) is highly reversible up to forces of 300 pN (Figure 5.2c and Supplementary Figure 5.2c). This observed reversibility is in accord with micropipette aspiration studies on mitotic chromosomes [15,17]. Interestingly however, while bright-field images do not show evidence for major structural changes to the chromosome (Figure 5.2b), we sometimes observe sudden drops in the force response, suggestive of small rupture events (Figure 5.2c, arrow). Force drops of >5 pN are most abundant during the first stretch cycle (in 23% of cases; n_{total} =155) and occur less frequently during consecutive stretches (in 14% of third stretches; n_{total} =79). Overall, the force-extension curves of consecutive stretches do not exhibit major signatures of plastic deformation in this force range.

To further characterize and quantify the non-linear stiffening that the chromosomes exhibit in the higher force regime, we determined the differential stiffness $k(F) = \frac{\Delta f}{\Delta d}$, as a function of force F, by evaluating the numer-

ical derivative of the force-extension curves (Supplementary Figure 5.2c) (Methods). Remarkably, the stiffness-force curves reveal, on a log-log scale, a surprisingly robust behavior for all chromosomes that were measured: at moderate to high forces (20-200 pN), the differential stiffness increases dramatically with force, increasing more than ten-fold over the initial, linear stiffness (Figure 5.2d). The linear increase on such logarithmic scale implies a power-law dependence, $k \propto F^\gamma$. Such power-law strain-stiffening behavior is predicted by basic models for polymers and their associated network assemblies: the freely-jointed-chain (FJC) is characterized by $\gamma = 2$ and the worm-like-chain (WLC) by $\gamma = 3/2$. In contrast, for chromosomes we observe $\gamma = 0.82 \pm 0.05$. Thus, the chromosome exhibits significantly weaker non-linear stiffening response that is distinct from these classical models.

To rule out that the anomalously weak stiffening behavior of chromosomes can be explained by remodeling of the structure, for example due to dynamic cross-links, we investigated the rate- and frequency dependence of the stiffening response. When a chromosome was stretched at increasing rates, an increasing hysteresis is seen between extension and retraction curves from rates above 0.5 μm/s, suggesting a significant viscous component to the response (Figure 5.2d). The dissipated energy as determined by numerical integration scales linearly with the rate and cannot be explained by viscous drag on the beads (Supplementary Figure 5.2d), indicating that at high stretch rates the chromosome exhibits a viscoelastic response. To quantify the viscoelastic response in the intermediate time-scales at various mechanical loads, we performed a differential approach: the chromosomes are loaded with a fixed pre-tension; subsequently, we superimpose a small distance oscillation at varying frequency to probe the differential force response at this force load, yielding the storage modulus $k'(F, \omega)$ and loss modulus $k''(F, \omega)$ (Methods). The storage modulus determined in this way is nearly constant over three orders of magnitude in frequency and is ten-fold larger than the loss modulus (Figure 5.2f). Moreover, the differential storage modulus measured over a range of forces is consistent with the stiffness derived directly from the force-extension data (Figure 5.2g). Taken together, these results show that the chromosome has a predominantly elastic mechanical response in the intermediate frequency range. Thus, we attribute the anomalously weak power-law stiffening to the intrinsic non-linear elastic response of the chromosome.

5
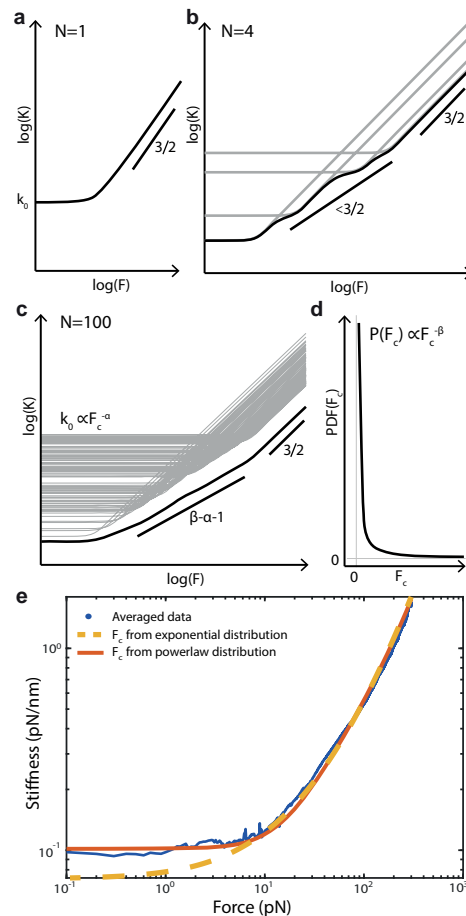
Figure 5.3: Successive stiffening of serial WLCs. a) Stiffness-force curves of a single WLC transitions from a constant stiffness directly towards a strain stiffening regime with a power-law scaling of 3/2. b) Stiffness force-curves of four WLCs (grey) in series result in an overall response (black) with an irregular transition zone to non-linear stiffening that has a lower effective strain stiffening exponent than 3/2. c) Strain stiffening curves of 100 serial WLC's with critical forces that have power-law distribution of $P(F_c) \propto F_c^{-\beta}$. (d) result in a smooth transition zone with a power-law exponent of $\beta - \alpha - 1$. f) Comparison of the experimental data (blue dots) with two realizations of the HWLC model where the critical forces are picked from a power-law distribution with total length L=1.0 µm and number of sub-chains N=300 (red line) or critical forces are picked from an exponential distribution with total length L=11.0 µm and number of sub-chains N=11000 (yellow dashed line).

5.3.5 A mechanical view of chromosomes

Our results corroborate that the nonlinear mechanics of the chromosomes do not behave according to classical models like a FJC or WLC polymer, which predict a strain stiffening power-law exponent of 3/2 and assume a uniform structure (Figure 5.3a). In fact, chromosomes exhibit a heterogeneous and hierarchical structure. This can be deduced from the presence of a proteinaceous scaffold, telomeric and centromeric regions, and the occurrence of G-banding patterns upon Giemsa staining reflecting chromatid compartments of dense heterochromatin and less condensed euchromatin [17,22,23]. The various elements of this structure could exhibit their own non-linear elastic response, characterized by an initial linear stiffness response and

a critical force for the onset of stiffening; the combined effect of all elements in this heterogeneous assembly would then combine to determine the mechanics of the chromosome as a whole.

To capture the heterogeneous nature of the chromosome, we propose a Hierarchical Worm-Like Chain (HWLC) model where we combine different WLC's in series, each with its own structural features such as contour length and persistence length. As an illustration of this idea, the mechanical response of this model including just a few mechanical elements is depicted in Figure 5.3b. At low force, the response of this system is dominated by the softest element. Above a critical force, however, this element stiffens, allowing the linear stiffness of the next softest elements to dominate, etc., leading to the sequential stiffening behavior. In this example, the step-like nature of the stiffening behavior is caused by the small number of mechanical elements that each stiffen at their own characteristic force. The number of different mechanical elements in an actual chromosome is likely larger, and their individual properties may be determined by a range of stochastic and assembly processes, such as the folding, looping, wrapping, and bundling of DNA.

To investigate whether a disordered many-component system could explain the observed stiffening response, we tested under what conditions the overall response of the HWLC model would lead to a smooth and reduced effective stiffening exponent. We find that the distribution that determines the hierarchy of critical forces for stiffening of the mechanical elements is crucial. While various distributions such as an exponential distribution render the overall stiffening response weaker, only a power-law distribution for the critical forces according to $P(F_c) \propto F_c^{-\beta}$ (Figure 5.3d) gives rise to genuine power-law stiffening power of the HWLC with an exponent $\beta - \alpha - 1$, where α is set by the relation between the initial stiffness and the critical force of each element, $k_0 \propto F_c^{-\alpha}$ (Supplementary Information 1). Conceptually, the overall mechanical response is always dominated by the softest non-stiffened element, resulting in an effective power-law exponent that is smaller than the power-law exponent of the individual WLC's (Figure 5.3c). When all elements of the structure have stiffened, the HWLC model predicts a transition to power-law exponent of 3/2.

To demonstrate that the HWLC model can capture our experimentally observed response, we first employ an exponential distribution for critical

forces and select model parameters to resemble the experimentally observed stiffening response. Indeed, with this distribution, we can realize a stiffness-force curve that is in close accord with our data (Figure 5.3e). Although this model does not capture the linear stiffness regime accurately for these model parameters and the model parameters have to be relatively large to obtain a reasonable agreement with the data (total chain length L=11.0 μm and number of sub-chains N=11000), we find that it closely resembles the nonlinear stiffening behavior of chromosomes for moderate and larger forces. Although the agreement is reasonable, there is no a priori reason for such an exponential distribution of critical forces in the chromosome. For comparison, we therefore also investigated a realization of the model where we select the critical forces from a power-law distribution. Remarkably, in this case we obtain a stiffness-force curve that is in close accord with our data and yields more reasonable values for the total chain length (L=1.0 μm, and number of sub-chains N=300)(Figure 5.3e). Taken together, we conclude that the HWLC model with a broad distribution of critical forces can give rise to a weaker stiffening exponent and can quantitatively account for the observed nonlinear mechanical response of chromosomes in our experiments.

5.3.6 Stretching of TOP2A-depleted chromosomes

To further investigate the relationship between structure and mechanics, we employed our mechanical characterization tools to assess the effect of one of the proteins essential for chromosome formation on the anomalous stiffening discussed above. The crucial role of TOP2A for mitotic chromosome formation has been well established for four decades [6,7,24,25], but its specific structural role has been a topic of ongoing debate [6,11,26]. To test the role of TOP2A in the anomalous strain-stiffening behavior we measured chromosomes depleted of TOP2A. To this end, we use rapid (1 hour) auxin inducible degradation (AID) of TOP2A in HCT116 cells [12]. In order to precisely control the exact moment of TOP2A depletion within the cell cycle, we applied the CDK1as system of chemical genetics to synchronize cells at the G2/M border [27] (Supplementary Figure 5.3a). We found that 0.25 μM 1NM-PP1 treatment for 16 hours efficiently arrests HCT116 TOP2A-mAID CDK1as cells in G2 (Supplementary Figure 5.3b). Six days prior to chromosome isolation we transduced HCT116 TOP2A-mAID CDK1as cells with lentivirus carrying
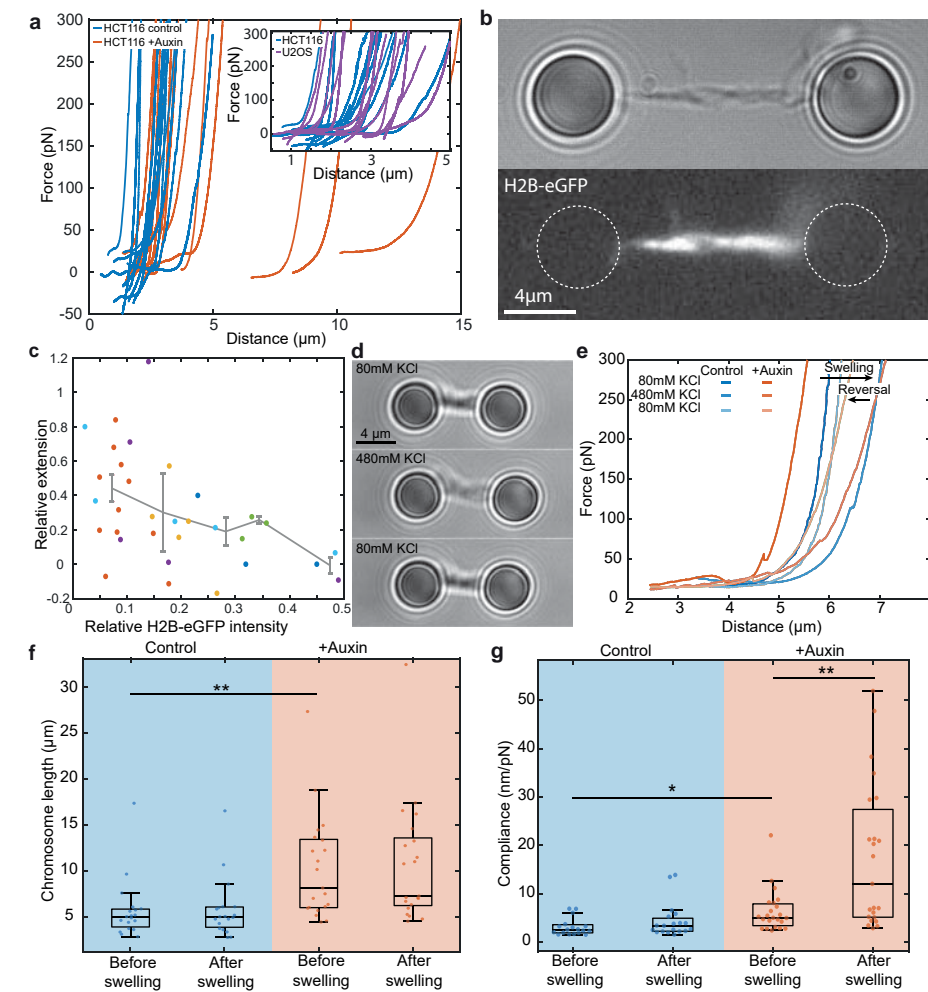
Figure 5.4: Mechanical and visual assessment and salt-induced expansion of TOP2A degraded HCT116 chromosomes. a) Stretching curves of control chromosomes (blue) and TOP2a degraded chromosomes (red). Inset: comparison of force-extension curves from HCT116 (blue) and U2OS (magenta) chromosomes. b) Bright field image of TOP2a degraded chromosome and corresponding H2B immunofluorescence image. c) The relative extension of darker and brighter H2B-eGFP regions as a function of relative intensity. Colors depict specific chromosomes. d) Bright field images of a chromosome in its original buffer containing 80 mM KCl and subsequent images after flushing in 480 mM KCl and return to 80 mM KCl. e) Force-extension curves of a control and TOP2A-degraded HCT116 chromosome before, during and after exposure to high salt buffer (480 mM KCl). Changes in length (f) and compliance (g) of chromosomes before and after the high salt exposure of control and TOP2A degraded chromosomes.

BirA-tagged TRF1 (Supplementary Figure 5.3c). We then arrested cells in G2 for 16 hours, before releasing them into nocodazole with or without auxin to arrest cells in prometaphase and depleted TOP2A for 4 hours (Supplementary Figure 5.3c). Mitotic cells were detached by shaking and chromosomes are isolated from this population. The chromosome spreads depicted altered chromosome morphology upon auxin exposure similar to what has been reported recently [12]: 75% of chromosomes appear hypocondensed in spreads compared to 5% of control chromosomes (Supplementary Figure 5.3d). Immunostaining of TOP2A on chromosome spreads shows that no antibodies bind to TOP2A-depleted chromosomes, confirming the depletion of TOP2A (Supplementary Figure 5.3e).

Surprisingly, the force-extension curves of the TOP2A-depleted chromosomes look qualitatively remarkably similar to control chromosomes. In contrast to the chromosome spreads, we only observe a small change of the stiffening length from $2.8 \pm 0.3\,\mu m$ to $3.0 \pm 0.1\,\mu m$ (p=0.03) for the majority of the chromosomes (Figure 5.4a and Supplementary Figure 5.4a). Moreover, an additional population of much longer chromosomes (with a stiffening length larger than 5 μm) is observed, as expected based on the observation of the hypocondensed morphology in chromosome spreads (Supplementary Figure 5.3d). In the tweezers experiments, these longer chromosomes occurred less frequently than in the chromosome spread, which might be caused by their lower bright-field contrast resulting in a selection bias for more contrast-rich, shorter chromosomes. Nevertheless, we find that TOP2A-depleted chromosomes are slightly softer: their compliance (inverse stiffness) at 200 pN is significantly higher $3.5 \pm 0.4\,nm/pN$ (TOP2A-depleted) versus $2.3 \pm 0.2\,nm/pN$ (control), p=0.013 (Supplementary Figure 5.4b). Moreover, the strain-stiffening power-law exponent is lower for TOP2A-depleted chromosomes 0.79 ± 0.04 (TOP2A-depleted) versus 0.98 ± 0.07 (control)(p=0.04), which, according to the HWLC model corresponds with a broader power-law distribution of critical forces (Supplementary Figure 5.4c and Figure 5.3d). To investigate whether such structural changes are also reflected in the visual appearance of the chromosome, we imaged H2B-eGFP labeled chromosomes with fluorescence microscopy during stretching. The elongated, hypocondensed chromosomes appear to have an altered morphology with irregular shapes and heterogeneous histone distributions along the chromosome arms (Figure 5.4b). Imaging chro-

mosomes during stretching demonstrated that darker regions containing a lower chromatin density extended more than brighter regions (Figure 5.4c and Supplementary Figure 5.4d). This direct observation of heterogeneous extension behavior of chromatin-rich and -arm regions is in line with expectations from the proposed HWLC model. Together, these changes in length, compliance and stiffening exponent indicate that TOP2A plays a crucial role in establishing the mitotic chromosome structure.

5.3.7   Salt-induced chromosome swelling

To investigate whether TOP2A also serves a structural role in maintaining the mitotic chromosome structure, we induced chromosome expansion and compaction by alternating the salt concentration between 80 mM KCl and 480 mM KCl (Figure 5.4d), following earlier studies [9,28]. Force-extension curves were obtained before, during and after salt-expansion (Figure 5.4e). During salt expansion we observed a strong elongation and softening of the chromosomes in agreement with literature [28]. Although the TOP2A degraded chromosomes are significantly larger before expansion, the chromosome lengths do not significantly change after expansion and compaction neither in the control nor in the TO2A-depleted group (Figure 5.4f). The compliance at 200 pN of the TOP2A-degraded chromosomes, however, significantly increases from $6 \pm 1\,nm/pN$ to $15 \pm 3\,nm/pN$ (p=0.0002), while the compliance of control chromosomes did not change (Figure 5.4g). In a similar fashion, the strain-stiffening power-law exponent of the control chromosomes does not appear to change, while that of TOP2A-depleted chromosomes with a high stiffening length (>5 μm) decreases significantly from 1.1 ± 0.2 to 0.4 ± 0.1 (p=0.0017) (Supplementary Figure 5.4e). Notably, the force-extension curves of the expanded chromosomes do not change after prolonged exposure to the higher salt concentration, indicating that there is no loss of material on the time scale of this experiment, which could be an explanation for the observed differences (Supplementary Figure 5.4f). Instead, we conclude that TOP2A applies a structural memory for refolding of the chromosome towards its original structure after salt expansion. These striking observations indicate that next to being indispensable for mitotic chromosome formation, TOP2A also serves a structural role in the maintenance of the mitotic chromosome.

5.4   Discussion

We have developed a methodology to combine optical tweezers with the specific attachment of mitotic chromosomes isolated from human cell lines. With this method we show that we can access mechanical information of individual chromosomes with a variety of experimental approaches, while having full control over experimental conditions and the possibility of several fluorescence imaging procedures. Although we restrained our experiments to forces up to 300 pN, in principle the maximal force that can be reached is only limited by the trapping power of the laser. Our piconewton resolution force-extension and oscillatory experiments show that chromosomes from U2OS and HCT116 cell lines exhibit a strain-stiffening response with a power-law exponent considerably lower than predicted by classical polymer models such as the WLC. While the initial stiffness and length of chromosomes were found to show substantial variability, the stiffening behavior for different chromosomes was remarkably robust. Such a robust response among chromosomes, suggests that this is an emergent behavior of the structure that is independent of the details of each particular chromosome. The strain-stiffening behavior is remarkably different from the linear force-extension that was observed before with micropipette aspiration studies [15,17]. Differences in force resolution and chromosome attachment strategy could explain the observed differences.

Based on the strain-stiffening behavior we observe, we propose a model based on successive stiffening of elements within the heterogeneous chromosomal structure as depicted in Figure 5.5. In this model the overall stiffening exponent arises from the broad distribution defining a hierarchy of critical forces that determine the individual stiffening of the mechanical elements in the chromosomal assembly. In this picture, the anomalous stiffening behavior of chromosomes emerges as a result of its heterogeneous nature. Indeed, in line with this model, we observe a reproducible shift in the stiffening response after perturbing the chromosomal structure by TOP2A-depletion or salt exposure. At the same time, fluorescence imaging indicates that the chromosomes exhibit significant heterogeneity along their length. It is tempting to speculate that such a hierarchical structure of nonlinear mechanical elements could be beneficial. At low forces, the strain increments will be distributed over the softer elements; with increasing force, however, they will rigidify such that further stretching is limited, implying
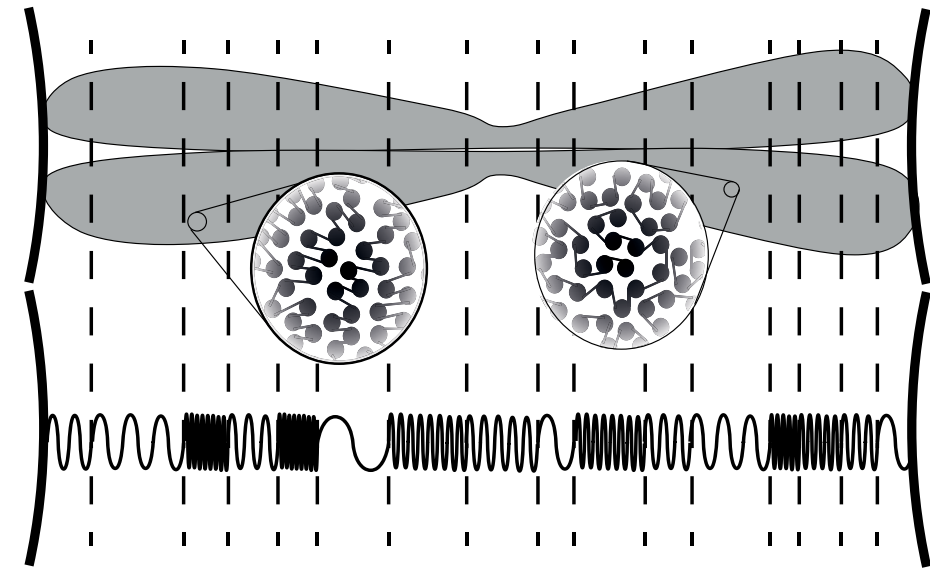
Figure 5.5: The mechanical response of mitotic chromosomes can be described with a HWLC model where as that of a series of WLCs with a broad distribution of material mechanical nonlinear properties gives rise to an emergent lowered stiffening response than that of the individual mechanical elements.

that additional strain increments will be largely bourn by the next stiffer mechanical element. At larger mechanical load, this will lead to a distribution of strain over all the mechanical elements according to their initial stiffness and critical stiffening forces. It will be exciting to further extend this kind of chromosome research to test whether the elements of the model are serially arranged, and could for example be related to G-banding patterns or condensin distributions along the chromosome as was proposed by previous AFM studies [23,29,30], or whether they are rather an expression of hierarchical structures that sequentially stiffen, or even a combination of those two. As such, the structural integrity of chromosomes could be protected against the pulling forces that they experience during mitosis. Such protection might be essential for passing the delicate chromosome folding organization existing in the mother cell to the two daughter cells.

We found that TOP2A-depleted chromosomes show subtle but significant variations in their mechanical properties. The most striking finding is that TOP2A is necessary to provide mechanical reversibility after salt-induced chromosome expansion, suggesting that TOP2A also fulfills a structural role for the maintenance of the compacted chromosome structure. It has been

hypothesized that such structural role can be achieved by acting as a staple between chromatin loops through binding of two dsDNA strands in the locked conformation of the protein complex [12]. This is also in line with our observation that the mechanical response of chromosomes is predominantly elastic, which makes it unlikely that structural remodeling by for example TOP2A activity during stretching takes place. How such a dual role of first resolving entanglements during compaction and then cross linking chromatin to maintain the condensed chromatin structure, is achieved will be an interesting topic of further research.

At the same time, the role of TOP2A in the chromosomal structure has been suggested to be a tight interplay with Condensin I, where, in a continuous process of topological rearrangements, Condensin I provides directionality for the (dis)entanglement of chromatin by TOP2A [12,26,31,32]. Our method provides an ideal platform to investigate such an interplay. The ability to physically manipulate chromosomes and the ability to image proteins, while providing a high degree of control over experimental conditions, makes our method ideal to further investigate the structural and mechanical roles of proteins such as Condensin I and II or Cohesin. We foresee that, by selective depletion, exposure to inhibitors and external addition of such proteins, we can gain more insight into the mechanism in which such proteins compact mitotic chromosomes. As such, this technique bridges quantitative single-molecule experiments with investigation of the complex macro-molecular complex of the chromosome under near-physiological conditions.

Acknowledgements

References

1. Nicklas, R. B. Measurements of the force produced by the mitotic spindle in anaphase. J. Cell Biol. 97, 542–548 (1983).
2. Ye, A. A., Cane, S. & Maresca, T. J. Chromosome biorientation produces hundreds of piconewtons at a metazoan kinetochore. Nat. Commun. 7, 1–9 (2016).
3. Vázquez-Diez, C. & Fitzharris, G. Causes and consequences of chromosome segregation error in preimplantation embryos. Reproduction 155, R63–R76 (2018).
4. Paulson, J. R. & Laemmli, U. K. The structure of histone-depleted metaphase chromosomes. Cell 12, 817–828 (1977).
5. Gibcus, J. H. et al. A pathway for mitotic chromosome formation. Science (80-.). 359, (2018).
6. Earnshaw, W. C., Halligan, B., Cooke, C. A., Heck, M. M. S. & Liu, L. F. Topoisomerase II is a structural component of mitotic chromosome scaffolds. J. Cell Biol. 100, 1706–1715 (1985).
7. Samejima, K. et al. Mitotic chromosomes are compacted laterally by KIF4 and condensin and axially by topoisomerase IIα. J. Cell Biol. 199, 755–770 (2012).
8. Ono, T. et al. Differential contributions of condensin I and condensin II to mitotic chromosome architecture in vertebrate cells. Cell 115, 109–121 (2003).
9. Hudson, D. F., Vagnarelli, P., Gassmann, R. & Earnshaw, W. C. Condensin is required for nonhistone protein assembly and structural integrity of vertebrate mitotic chromosomes. Dev. Cell 5, 323–336 (2003).
10. Farr, C. J., Antoniou-Kourounioti, M., Mimmack, M. L., Volkov, A. & Porter, A. C. G. The α isoform of topoisomerase II is required for hypercompaction of mitotic chromosomes in human cells. Nucleic Acids Res. 42, 4414–4426 (2014).
11. Hirano, T. & Mitchison, T. J. Topoisomerase II does not play a scaffolding role in the organization of mitotic chromosomes assembled in Xenopus egg extracts. J. Cell Biol. 120, 601–612 (1993).
12. Nielsen, C. F., Zhang, T., Barisic, M., Kalitsis, P. & Hudson, D. F. Topoisomerase IIa is essential for maintenance of mitotic chromosome structure. Proc. Natl. Acad. Sci. U. S. A. 117, (2020).
13. Neuman, K. C. & Nagy, A. Single-molecule force spectroscopy: optical tweezers, magnetic tweezers and atomic force microscopy. Nat. Methods 5, 491–505 (2008).
14. Houchmandzadeh, B., Marko, J. F., Chatenay, D. & Libchaber, A. Elasticity and structure of eukaryote chromosomes studied by micromanipulation and micropipette aspiration. J. Cell Biol. 139, 1–12 (1997).
15. Sun, M., Kawamura, R. & Marko, J. F. Micromechanics of human mitotic chromosomes. Phys. Biol. 8, (2011).
16. Poirier, M., Eroglu, S., Chatenay, D. & Marko, J. F. Reversible and irreversible unfolding of mitotic newt chromosomes by applied force. Mol. Biol. Cell 11, 269–276 (2000).
17. Sun, M., Biggs, R., Hornick, J. & Marko, J. F. Condensin controls mitotic chromosome stiffness and stability without forming a structurally contiguous scaffold. Chromosom. Res. 26, 277–295 (2018).

18. Garcia-Exposito, L. et al. Proteomic Profiling Reveals a Specific Role for Translesion DNA Polymerase η in the Alternative Lengthening of Telomeres. Cell Rep. 17, 1858–1871 (2016).

19. Spector, D. L., Goldman, R. D. & Leinwand, L. A. Cells: a laboratory manual. (1998).

20. Heller, I., Hoekstra, T. P., King, G. A., Peterman, E. J. G. & Wuite, G. J. L. Optical tweezers analysis of DNA-protein complexes. Chem. Rev. 114, 3087–3119 (2014).

21. Schoen, I., Ries, J., Klotzsch, E., Ewers, H. & Vogel, V. Binding-activated localization microscopy of DNA structures. Nano Lett. 11, 4008–4011 (2011).

22. Kireeva, N., Lakonishok, M., Kireev, I., Hirano, T. & Belmont, A. S. Visualization of early chromosome condensation: A hierarchical folding, axial glue model of chromosome structure. J. Cell Biol. 166, 775–785 (2004).

23. Hliscs, R., Mühlig, P. & Claussen, U. The nature of G-bands analyzed by chromosome stretching. Cytogenetic and Genome Research vol. 79 162–166 (1997).

24. Adachi, Y., Luke, M. & Laemmli, U. K. Chromosome assembly in vitro: Topoisomerase II is required for condensation. Cell 64, 137–148 (1991).

25. Johnson, M., Phua, H. H., Bennett, S. C., Spence, J. M. & Farr, C. J. Studying vertebrate topoisomerase 2 function using a conditional knockdown system in DT40 cells. Nucleic Acids Res. 37, (2009).

26. Piskadlo, E. & Oliveira, R. A. A topology-centric view on mitotic chromosome architecture. Int. J. Mol. Sci. 18, 1–21 (2017).

27. Saldivar, J. C. et al. An intrinsic S/G2 checkpoint enforced by ATR. 361, 806–810 (2018).

28. Poirier, M. G., Monhait, T. & Marko, J. F. Reversible hypercondensation and decondensation of mitotic chromosomes studied using combined chemical-micromechanical techniques. J. Cell. Biochem. 85, 422–434 (2002).

29. Tamayo, J. Structure of human chromosomes studied by atomic force microscopy: Part II. Relationship between structure and cytogenetic bands. J. Struct. Biol. 141, 189–197 (2003).

30. Hoshi, O. & Ushiki, T. Three-dimensional structure of G-banded human metaphase chromosomes observed by atomic force microscopy. Archives of Histology and Cytology vol. 64 475–482 (2001).

31. Charbin, A., Bouchoux, C. & Uhlmann, F. Condensin aids sister chromatid decatenation by topoisomerase II. Nucleic Acids Res. 42, 340–348 (2014).

32. Baxter, J. et al. Positive supercoiling of mitotic DNA drives decatenation by topoisomerase II in eukaryotes. Science (80-.). 331, 1328–1332 (2011).

33. Hochegger, H. et al. An essential role for Cdk1 in S phase control is revealed via chemical genetics in vertebrate cells. J. Cell Biol. 178, 257–268 (2007).

34. Dull, T. et al. A Third-Generation Lentivirus Vector with a Conditional Packaging System. J. Virol. 72, 8463–8471 (1998).

35. Rother, J., Nöding, H., Mey, I. & Janshoff, A. Atomic force microscopy-based microrheology reveals significant differences in the viscoelastic response between malign and benign cell lines. Open Biol. 4, (2014).

36. Marko, J. F. & Siggia, E. D. Stretching DNA. Macromolecules 28, 8759–8770 (1995).

37. Broedersz, C. P. & MacKintosh, F. C. Modeling semiflexible polymer networks. Rev. Mod. Phys. 86, 995–1036 (2014).

5.5   Methods

Cell lines and cell culture.   All cell lines were cultured in DMEM supplemented with 10% FBS and penicillin-streptomycin in a humidified incubator at 37°C and 5% CO2. The U2OS TRF1-BirA cell line [18] was a kind gift from Roderick J. O' Sullivan (University of Pittsburgh, USA). Endogenous H2B in the U2Os TRF1-BirA cell line was tagged with EGFP like described in [12]. The HCT116 TOP2A-mAID H2B-EGFP cell line was a kind gift from Damien F. Hudson (MCRI, Australia) and described in [12]. The HCT116 TOP2A-mAID H2B-EGFP cell line was modified for CDK1as chemical genetics by knock-in of CDK1as and knockout of endogenous CDK1 like described in [27] and based on [33]. The three plasmids for the CDK1as on-shot system were purchased from Addgene: "CDK1as_T2A_Zeocin" and "pX330_human CDK1" plasmids were gifts from William Earnshaw (Addgene plasmid # 118596 and # 118597) and "pCMV(CAT) T7-SB100" was a gift from Zsuzsanna Izsvak (Addgene plasmid # 34879). Incubation time and concentration of 1NM-PP1 was optimized by propidium iodide flow cytometry (Supplementary Figure 5.3b), performed like described in ref. 12. A Neon transfection system (Thermo-Fischer Scientific) was used for transfections of HCT116 and U2OS cell lines according to manufacturer recommendations. 1NM-PP1 and nocodazole was purchased from Sigma-Aldrich. IAA was purchased from Santa Cruz.

Lentiviral production and transduction.   We produced 3rd generation lentiviral particles for integration of BirA-TRF1. HEK293T cells were grown with 25μM cloroquine diphosphate (Sigma-Aldrich) for 5 hours before being transfected with plasmids pMD2.G, pMDLg/pRRE and pRSV-Rev (Addgene #12259, #12251 and #12253. Kind gifts from Didier Trono [34] and a transfer plasmid for BirA-TRF1 integration. Calphos mammalian transfection kit (Clontech) was used for transfections according to manufacturer protocol. 18 hours after transfection, media with transfection complexes was removed and fresh medium added. 48 hours after transfection the growth medium was harvested, centrifuged at 500g for 5 min. and the supernatant containing viral particles

filtered at 0.45µM before being concentrated 10X using Amicon Ultra-15 100kDa centrifugal units (Merck-Millipore). The viral concentrate was snap-frozen and stored at -80ºC. For lentiviral transduction, HCT116 TOP2A-mAID CDK1as cells was incubated with 7.5µg/mL polybrene in 3mL 10X lentiviral concentrate and 7mL growth medium for 1 hour with mixing every 15 min. Cells were then seeded in T-175 flask and the culture expanded for chromosome isolation.

Chromosome isolation. A previously reported method was adjusted in order to isolate mitotic chromosomes in large quantities with minimal cell debris contamination [19]. In brief, cells were grown with 12.2 mg/L biotin (Sigma-Aldrich) for 24h before isolation. On the day of isolation, 8-10 T175 flasks of cells was treated for 4 hours with 200ng/mL nocodazole (Sigma-Aldrich) and we then performed mitotic shake-off to enrich for mitotic cells. The mitotic cells were centrifuged at 300 g for 5 min. resuspended in 10mL 75mM KCl and 5mM TRISHCl pH 7.4 and incubated for 10 min. at RT. All steps were carried out at 4ºC from this point on. Cells were centrifuged at 300g for 5 min and resuspended in 8mL polyamine (PA) buffer (20m TRIS-HCl pH 7.4, 0.5mM EDTA-K, 80mM KCl, 1mM spermidine, 0.4mM spermine and 0.2% tween-20, supplemented with Complete mini protease and Phostop phosphatase inhibitor cocktails (Roche). This suspension was then dounce homogenized for 25 strokes with tight pestle. This suspension was cleared twice of cell debris by centrifugation at 300g for 5 min. Chromosomes were purified using a glycerol gradient containing two layers (60% glycerol in PA and 30% glycerol in PA). After centrifugation at 1750 g for 30 minutes the chromosomes could be collected from the 60% glycerol fraction and stored at -20ºC in ~60% glycerol in PA buffer with a concentration of 10^6-10^7 chromosomes/mL. Neither visual inspection, nor force-extension response shows a change of the chromosomes even after storing them for up to two months.

Western blotting. SDS-PAGE and immunoblotting was carried out like described previously (Nielsen et al. 2015, Nat Comm.) Antibodies used were: CDK1 (ab133327, Abcam), c-Myc (sc-40, Santa Cruz) and Histone H3 (ab1791, Abcam).

Dual trap optical tweezers with wide field fluorescence. The dual trap optical set-up was described previously [20]. In brief, two optical traps are created

using a 20 W, 1064 nm CW fiber laser (YLR-20-LP-IPG, IPG Photonics). Two traps are created by splitting the laser beam into two paths using a polarizing beam splitter cube and can be steered independently using one accurate piezo mirror (Nano-MTA2X10, Mad City Labs) and one coarse positioning piezo step mirror (AG-M100N). After recombination of the two paths they are coupled into a Nikon microscope body using two 300mm lenses, and focused in the flow cell with a 1.2 NA water immersion objective (Nikon, Plan apo VC NA1.2). Back-focal plane interferometry is used to measure forces and bead tracking is performed by LED illuminated bright field imaging on a CMOS camera (DCC1545M, Thorlabs). Wide field epifluorescence is achieved by illumination with 488, 532, 561 and 639 nm lasers (Cobolt 06-01 Series) and detection via separation of the emission light using an OptoSplit III (Cairn Research) and imaging on a EMCCD camera (iXon 897 Life, Andor Oxford Instruments Technology).

Microfluidics and flow cell preparation. A microfluidic flow-system (u-Flux, LUMICKS B.V.) is used to insert solutions into a 5-channel silicon flow cell. Before each experiment bleach cleaning is performed to remove residual debris from flow cell, followed by Sodium thiosulfate neutralization. Passivation is performed to reduce chromosome attachment to tubing and flow cell walls by incubation for 1 hour with 0.05% casein solution, followed by excessive rinsing with PA buffer.

Immunofluorescence. Chromosomes were incubated overnight at 4°C with primary antibody in a concentration of 5 µg/mL and subsequently diluted a factor of five in PA buffer and stored for 1 hour at 4°C. Next, chromosomes were incubated with secondary antibody in a concentration of 5 µg/mL for 1 hour at room temperature. After addition of PA buffer to dilute another factor of five, chromosomes were stored for 30 minutes at 4°C. To remove excessive antibodies, chromosomes were centrifuged at 750 RCF for 5 minutes on a 20 µL glycerol cushion. Supernatant was removed, leaving ~100µL chromosome solution that could be used for imaging. Primary antibodies were anti-NCAPH (Sigma Aldrich), CREST anti-sera (Immunovision) and anti-H3-Alexa647 (ThermoFisher). Secondary antibodies were anti-rabbit-Alexa647 (ThermoFisher) and anti-human-Alexa488 (ThermoFisher).

Statistical analysis. Average values and errors are always represented as mean ± standard error of the mean (SEM). Differences in populations are tested using a Wilcoxon rank-sum test, where a p-value<0.05 is regarded as significant (*) and a p-value<0.01 as highly significant (**).

Differential stiffness, stiffening length and compliance. To calculate the differential stiffness from force-distance curves, the force distance curve was first smoothed using a moving average with a window size of 1/15 of the total data points in the force curve, followed by numerical derivation. To determine the onset of stiffening, first the plateau stiffness was determined as the most likely stiffness at forces below 50 pN, as estimated from the maximum of a kernel density estimate of the stiffness values. The onset of stiffening was then determined as the point where the stiffness exceeds the plateau stiffness by one standard deviation of all stiffnesses below 50 pN. To determine the compliance at 200 pN the inverse of the stiffness of the chromosome at a force of 200 pN was used.

Microrheolohy. Oscillations of the optical trap were generated by applying a sinusoidal voltage to the analog input of the piezo mirror controller (Nano-Drive, MCL, Madison, USA) in order to apply the oscillation on top of the digitally controlled mirror position. The signal was first generated digitally using Labview (National Instruments, Austin, USA). The analog voltage was then produced with a digital analog converter (DAQ, National Instruments, Austin, USA). Oscillations were produced with an amplitude of 25 mV corresponding to a trap displacement of roughly 200 nm. The frequency of the oscillation was varied between 2 mHz and 1 Hz. Data analysis of the oscillations was performed in Matlab (Mathworks, Natick, USA). First, the bead-bead distance and the force were synchronized based on the position of the bead, where the force was measured. Then the oscillatory data was analyzed following a procedure by Rother et al. [35]. In brief, both the force as well as the bead-bead separation were detrended and fitted with a sine function with a fixed frequency set to the experimental frequency and an additional offset. Then the complex stiffness was calculated as $k = \frac{A_F}{A_d} e^{i(\varphi_F - \varphi_d)}$ with the amplitude and the phase of the force oscillation A_F and φ_F, the amplitude and the phase of the distance oscillation A_d and φ_d, respectively.

5.6 Supplementary Information

5.6.1 Supplementary information 1: Hierarchical Worm-Like Chain (HWLC) model

5.6.1.1 Introduction
To provide insight into the nonlinear mechanical response of a chromosome, we here develop and analyze a class of toy models describing a disordered serial assembly of nonlinear mechanical components. Each of these assembly components is characterized by its linear stiffness and critical force - the characteristic force threshold at which the component stiffens dramatically. The structure of chromosomes is heterogeneous, and it is affected by noisy physical and biological processes, including polymer fluctuations and the localization of structural proteins such as histones, cohesins or condensins. Together, these processes determine how the DNA is wrapped, looped, folded, and bundled in chromosomes. To capture the partially heterogeneous and disordered nature of the chromosome, we assume that the characteristics of the nonlinear assembly components are randomly sampled from given distributions. Thus, we propose that broad distributions of the mechanical characteristics of components define structurally heterogeneous models, which describe the integrated mechanical properties of complex assemblies, such as chromosomes.

Our aim is to predict the nonlinear mechanical response of a randomly sampled assembly, and to investigate if this expected response can quantitatively reproduce the anomalous stiffening behavior of chromosomes we observed in our tweezer experiments.

5.6.1.2 Model for flexible WLC components
Consider N components extending in series, with component i characterised by its critical force $F_{c,i}$ and linear response spring coefficient $k_{0,i}$. These components can correspond to segments of the chromosome with different elastic properties, to cross-linking structural elements within a gel-like network experiencing shear, or to collective mechanical modes on different length-scales of a hierarchical assembly.

We presume that the critical forces are independently and identically distributed according to some probability density function $P(F_c)$. In general,

$F_{c,i}$ and $k_{0,i}$ may not be independent, and we will presume that they follow some constitutive law: $k_0(F_c) = \int P(k_0|F_c)k_0 dk_0$, which is the mean linear spring coefficient for a component with critical force F_c.

We presume that each component can be described as a flexible worm-like chain with its contour length L_i larger than its persistence length $l_{p,i}$. We will discuss how our model generalizes to other component types in Section 5.6.1.3.

When a force F is exerted on the assembly, each flexible WLC component's extension x_i satisfies $F = g(x_i, F_{c,i}, k_{0,i})$, where

$$g(x_i, F_{c,i}, k_{0,i}) = F_{c,i}\left(\frac{x_i}{L_i} - \frac{1}{4} + \frac{1}{4(1-x_i/L_i)^2}\right) [36]$$

with $L_i = \frac{2}{3}\frac{k_{0,i}}{F_{c,i}}$. Note that in this case, since $k_0 \propto LF_c$, we have that $k_0(F_c) \propto F_c \int P(L|F_c)L dL$, so that the constitutive law is set by possible correlations between the component length L_i and persistence length $l_{p,i} = k_B T F_{c,i}^{-1}$, with Boltzmann's constant k_B and temperature T.

The total response of the assembly is found by considering its total extension, $X = \sum_{i=1}^{N} x_i$. Thus, we have

$$F' := \frac{dF}{dX} = \left(\frac{dX}{dF}\right)^{-1} = \left(\sum_i \frac{1}{dg(x_i, F_{c,i}, k_{0,i})/dx_i}\right)^{-1}.$$

The dominant contributions to the total response $F'(F)$ will hence be given by the softest components, with the smallest individual responses $\frac{dg(x_i, F_{c,i}, k_{0,i})}{dx_i}$. Geometrically, this implies that the total response curve of the assembly roughly follows the behaviour of the lowest individual response curve. This idea is illustrated by the total response of an assembly with three components, as shown in Supplementary Figure 5.5a. The step-like features in the overall response curve are a result of the small number of components in this example, and these features are expected to become less apparent as the number of components increases.

For a general assembly, we distinguish two cases:

1. The individual response curves of the components cross. Consequently, the dominant component in the overall response of the assembly varies as a function of the force Supplementary Figure 5.5a. This corresponds to a constitutive law $k_0(F_c) \propto F_c^{-\alpha}$, with $-\alpha < 3/2$.
2. The individual response curves of the components never cross, implying that the component with minimum k_o always dominates the

stiffening response of the whole assembly (Supplementary Figure 5.5b). This corresponds to a constitutive law $k_0(F_c) \propto F_c^{-\alpha}$, with $-\alpha > 3/2$.

In case 1, we can estimate the average total response of the chain by considering contributions from only those components that are still in the linear response regime: $F'(F)^{-1} \approx \int_F^\infty \frac{NP(F_c=f)}{k_0(f)} df$.

Note, this integral scales with $F^{-\gamma}$ if the integrand scales with $F^{-\gamma-1}$. Importantly, we see that our model predicts that the assembly stiffens according to a power-law relationship $F'(F) \propto F^\gamma$, if we assume a constitutive law $k_0(F_c) \propto F_c^{-\alpha}$, together with critical force distribution $P(F_c) \propto F_c^{-\alpha-\gamma-1}$. We verify this scaling prediction by performing simulations of such a disordered assembly (Supplementary Figure 5.5c). In fact, by suitable choices of the parameters that specify the constitutive relation and the critical force distribution, we find behavior in accordance with the experimentally measured chromosome response: $F'(F) \propto F^\gamma$, with $\gamma \approx 0.85$.

In case 2, individual response curves of the different components lie parallel to one another or asymptotically approach the same limit, and we therefore cannot neglect contributions to the total response from components that have already started stiffening, as in case 1. For case 2, the expected total response can hence be approximated as

$$F'(F)^{-1} \approx \int_F^\infty \frac{NP(F_c=f)}{k_0(f)} df + \int_0^F \frac{NP(F_c=f)}{dg(x,f,k_0(f))/dx} df.$$

In general, no exact scaling behavior for the total stiffening response is expected, since the largest contributions come from the second term, and $dg(x, f, k_0(f))/dx$ scales differently at different f. However, in principle, certain long-tailed distributions of $F_{c,i}$ could give stiffening responses which resemble scaling behavior.

5.6.1.3 Extension to semi-flexible WLCs and other chain models

Next, we demonstrate that the model described above can also be generalized to assemblies of other kinds of components, such as semi-flexible WLCs. The modification corresponds to supposing that each component's individual response follows $F = \mathbf{g}(x_i, F_{c,i}, k_{0,i})$ for some $g \neq \mathbf{g}$. As an example, for semi-flexible WLCs with $L_{p,i} > l_i$, we have

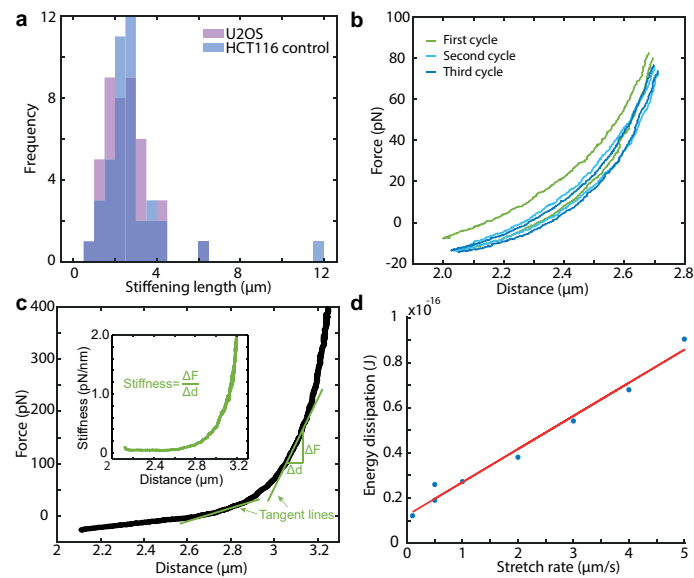$$\mathbf{g}(x_i, F_{c,i}, k_{0,i}) = \frac{9F_{c,i}}{\pi^2}\left(\frac{1}{(1-\epsilon_i)^2} - \frac{\epsilon_i}{3} - 1\right) [37],$$

where $\epsilon_i = x_i \frac{\pi^2}{15} \frac{k_{0,i}}{F_{c,i}}$. In this limit, the constitutive law is given by $k_0(F_c) \propto F_c^2$.

The two categories of models described in Section 5.6.1.2. are further generalized by comparing the exponent of the constitutive law to the large-force stiffening behavior of each component. Specifically, if the components follow a constitutive law $k_0(F_c) \propto F_c^{-\alpha}$ and $\lim\limits_{F \gg F_c} F'(F) \propto F^\delta$, the individual response curves of the components cross when $-\alpha < \delta$. This implies, for example, that all models consisting of semi-flexible chains, with $2 = -\alpha > \delta = 3/2$, fall under category 2; the individual response curves never cross. As for flexible WLCs with $-\alpha > 3/2$, serial assemblies of semi-flexible WLCs can exhibit stiffening behavior that resembles scaling, given that the critical forces are broadly distributed. Interestingly, we find that for semi-flexible WLCs, an exponential distribution of critical forces can result in such behavior (Supplementary Figure 5.5d).
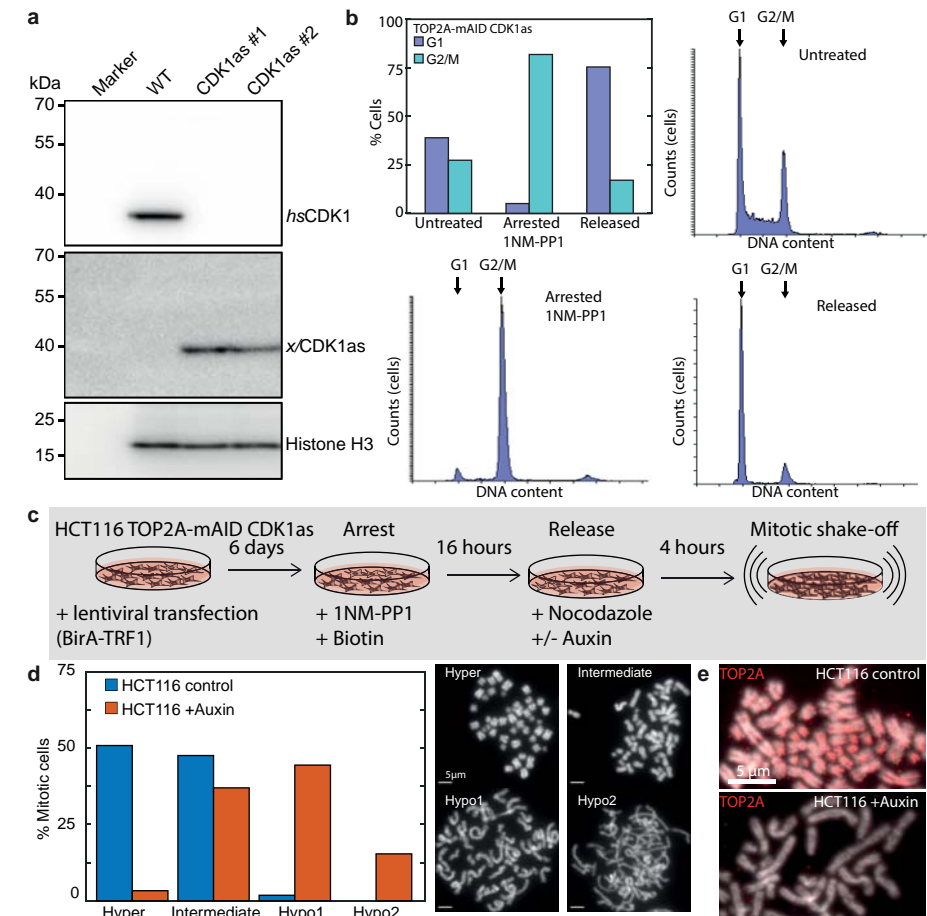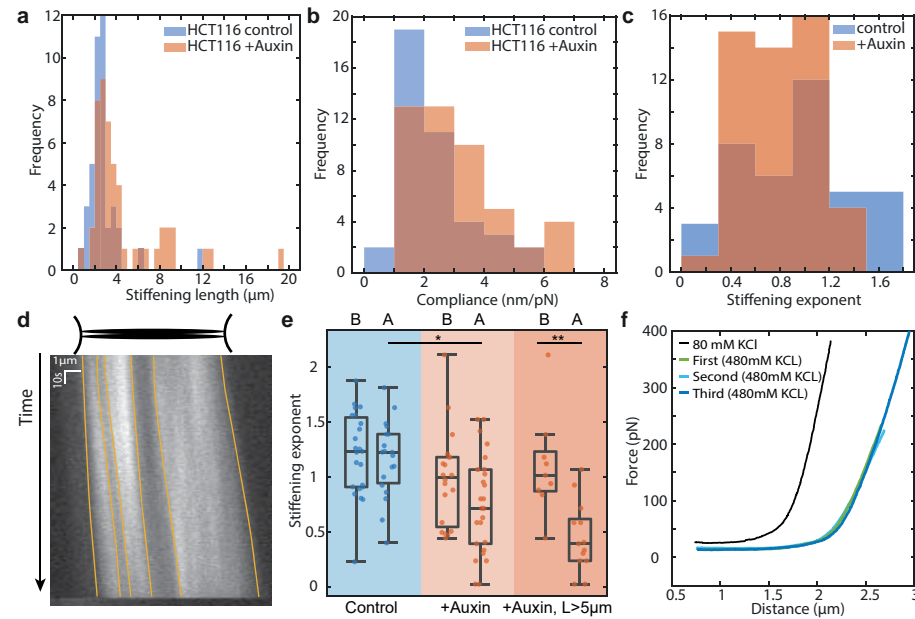
5.7 Supplementary Figures
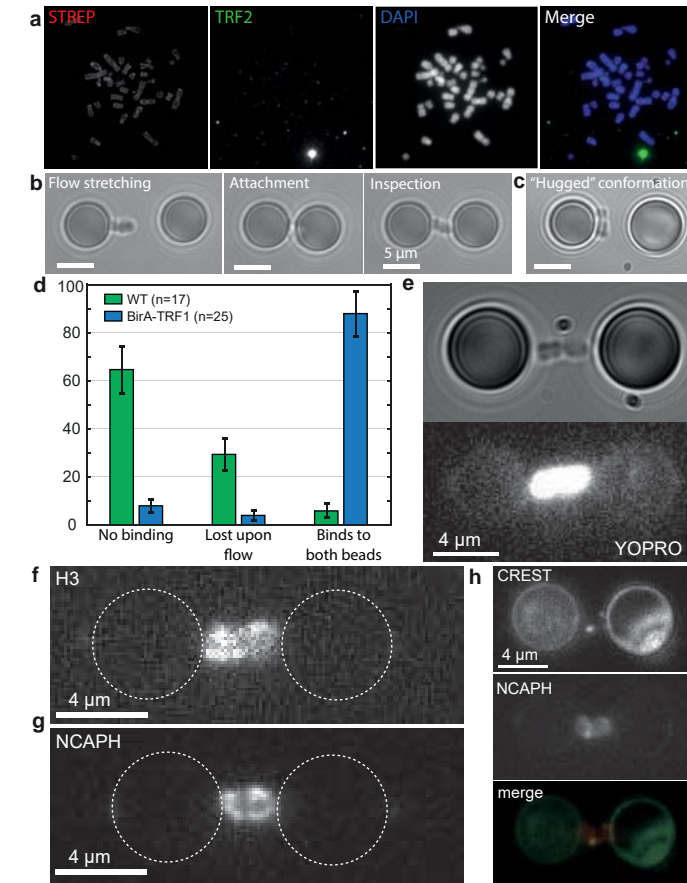
Supplementary Figure 5.1: Chromosome attachment and visualization. a) Upon addition of biotin to U2OS cells expressing BirA-TRF1, biotin is incorporated around the telomeres of chromosomes. The concentration of mitotic cells is enhanced upon addition of 6h Nocodazole. Mitotic cells are harvested by shaking and chromosomes are isolated from cells by application of mechanical shear stress to disrupt the cell membrane. b) Schematic of chromosome attachment to microspheres in a microfluidic flow cell with parallel channels (left). After trapping two streptavidin coated microspheres (1), a chromosome is attached to one microsphere by exploitation of the radiation pressure of the optical trap that the chromosome experiences (2). In one of the main channels of the flow cell, the chromosome gets flow stretched (3) and attached to the second microsphere (4). c) Bright-field image of mitotic chromosomes show telomeric attachment of four arms. The centromeric region is discernable by an indentation of the chromosome (arrows). d) Fluorescence of H2B-eGFP (bottom) and corresponding bright-field (top) image. e) BALM super resolved image of SxO binding events. Centromeric region is depicted by arrowheads. f) Immuno-staining of NCAPH and CREST shows localization of Condensin I along the chromatids and two foci that reveal the position of the centromeres.

Supplementary Figure 5.2: a) Histogram of stiffening length of U2OS and HCT116 chromosomes. b) Three consecutive elongation and retraction curves of a chromosome stretched to around 80pN. c) Differential stiffness is determined by a taking the numerical derivative of the force-extension data, i.e. approximating the slope of a tangent line to the data. Stiffness-distance plots (inset) show that the stiffness increases with distance. f) Energy dissipation during extension-relaxation experiments as a function of stretch rate (blue dots) shows a linear increase (red line to guide the eye).

Supplementary Figure 5.3: a) Immunoblot of wildtype HCT116 cells (WT) and clones of CDK1as in which endogenous CDK1 has been knocked out (hsCDK1, 34kDa) and the mutant CDK1as gene has been knocked-in and is expressed ectopically (xlCDK1as, 40kDa). The CDK1 antibody used only recognises hsCDK1 xl-CDK1as is tagged with MYC and detected by c-Myc antibody. #1 is a TOP2A-mAID clone and #2 the TOP2A-mAID H2B-EGFP clone used in this study. Histone H3 was used as a loading control. b) Optimization of CDK1as cell synchronization. Quantification of G1 and G2/M content from PI-flow cytometry profiles of untreated HCT116 TOP2A-mAID CDK1as cells, HCT116 TOP2A-mAID CDK1as cells grown with 0.25µM 1NM-PP1 for 16 hours to arrest them in G2 phase, and HCT116 TOP2A-mAID CDK1as cells grown with 0.25µM 1NM-PP1 for 16 hours and then released from this block and grown for 4 hours. c) Diagram of experimental procedure of TOP2A depletion. d) Statistics on the different chromosome morphologies and how often they are observed in control versus TOP2a degraded cells with representative images of chromosome spreads. e) Immunostaining for TOP2A on chromosome spreads of control and the auxin exposed HCT116 TOP2A-mAID CDK1as cells confirms degradation of TOP2A in the auxin exposed chromosomes.

Supplementary Figure 5.4: Histograms of stiffening length (a), compliance at 200 pN (b) and strain stiffening power-law exponent (c) for control and auxin exposed chromosomes. d) Kymograph of fluorescence signal during chromosome stretching. The boundaries of regions with different histone intensity signal are depicted by lines. e) Stiffening exponent of force-extension curves for HCT116 control chromosomes, auxin exposed chromosomes and auxin exposed chromosomes with a stiffening length above 5 μm before (B) and after (A) salt-induced expansion. f) Force-extension curve of HCT116 chromosome be-fore salt-induced expansion at 80 mM KCL (black line) and three consecutive force-extension curves during salt induced expansion at 480 mM KCl.
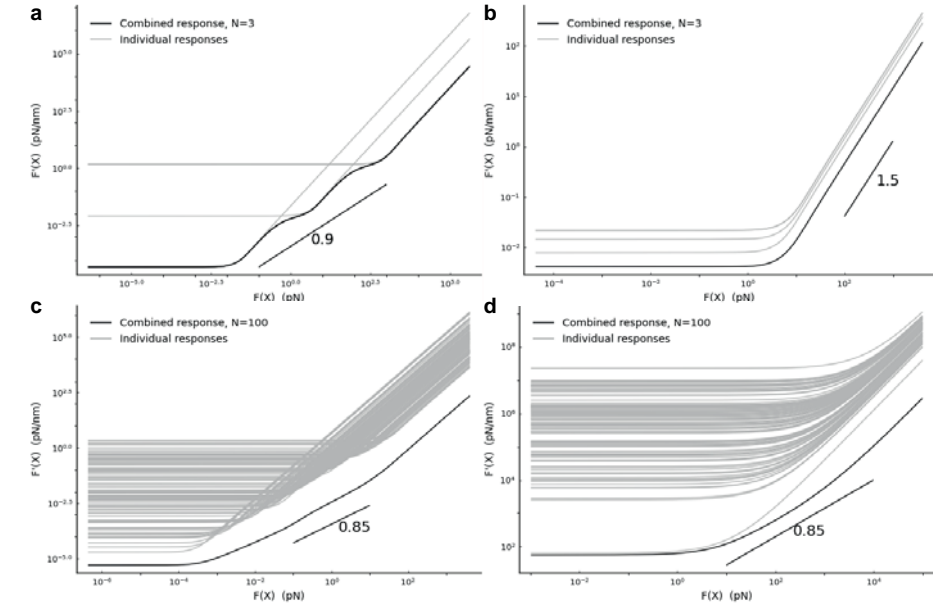
Supplementary Figure 5.5: The individual and total responses for an assembly of three flexible worm-like chains. For this example, critical forces are given by a power-law; $P(F_c) \propto F_c^{-0.9}$, with cut-offs 0.0004 and 40 pN. All chains are of equal length $L = 1000nm$, and the constitutive law is hence $k_0 = LF_c$. b) The individual and total response curves for an assembly of three flexible WLCs, with power-law distributed critical forces $P(F_c) \propto F_c^{-1}$, with cut-offs 0.0004 and 40 pN. The length of each component is chosen as $L(F_c) = \frac{3000}{\sum F_{c,i}^2} F_c^2$, so that the total length of the assembly is 3000 nm, and the constitutive law is $k_0(F_c) = L(F_c)F_c \propto F_c^3$. c) The individual and total response curves for an assembly of 100 flexible WLCs with power-law distributed critical forces; $P(F_c) \propto F_c^{-\beta}$, $\beta = 0.85$, and equal component lengths; $k_0(F_c) = LF_c^{-\alpha}$, $\alpha = -1$, $L = 30nm$. Slope prediction is given by $\beta - \alpha - 1 = 0.85$. Cut-offs for P($F_c$) are 0.0004 and 40 pN. d) The individual and total response curves for an assembly of 100 semi-flexible WLCs with an exponential distribution of critical forces: $P(F_c) = \frac{e^{-F_c/50}}{50}$. The linear spring coefficients are $k_0 = F_c^2 \frac{90}{\pi^4 k_B T}$.

5

Outlook

The work described in this thesis may serve as a starting point for a wide variety of interesting research on the investigation of chromosomes. During development of a method to optically manipulate mitotic chromosomes as presented in Chapter 5, we occasionally observed that a DNA tether was pulled out from one end of the chromosome, which might open up a new possibility to unravel the structure of mitotic chromosomes. At the same time, efforts have been made to develop new technical and methodological tools to expand the possibilities of mitotic chromosome manipulation. Two of these projects particularly resulted in promising preliminary results: super-resolution imaging of optically trapped chromosomes and manipulation of chromosomes in different geometries. I will first describe the preliminary results of these three projects and briefly outline how these experiments can contribute to the research on mitotic chromosomes. I will conclude with a section describing some of the outstanding questions in the field that might be addressed with the use of optical micromanipulation of mitotic chromosomes.

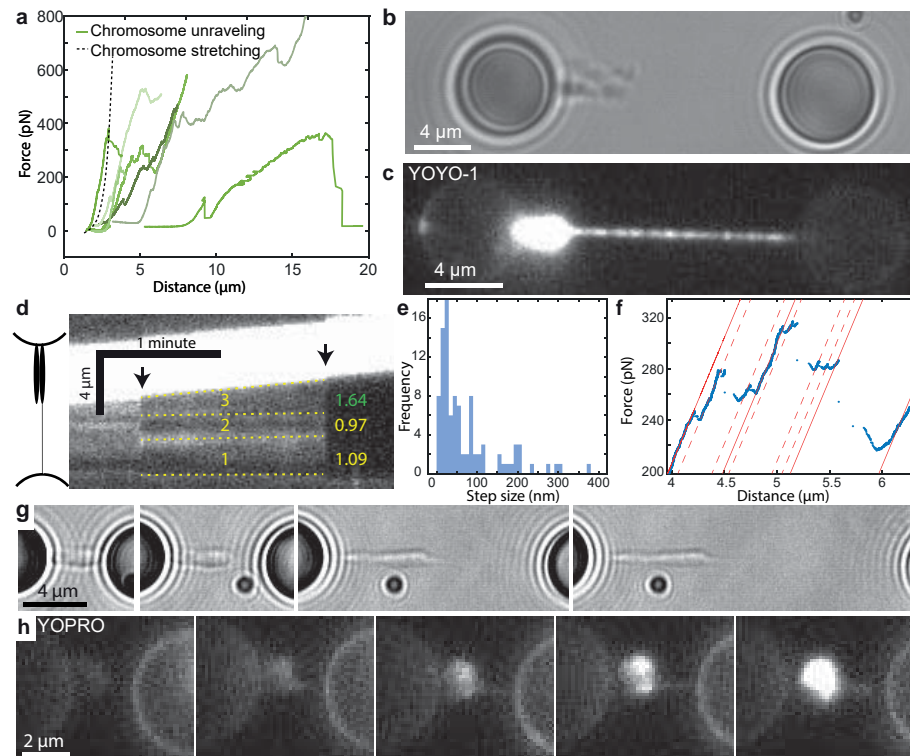## 6.1 Mechanical unraveling of the chromosome

The research described in Chapter 5, focuses on the stretching of entire mitotic chromosomes along their length. Another unique possibility that our methods allows is to study the linear arrangement of the DNA inside the mitotic chromosome. We hypothesized that in the presence of only a few biotin-streptavidin links, we should be able to unravel the chromosome from one end. Such unravelling of the DNA from one end, could reveal valuable insights into the existence and nature of chromatin loops that emanate from a central scaffold[1].

Indeed, in a small subset of the chromosome samples (6%) large ruptures were observed in the force extension curves (Figure 6.1a), leading to a configuration where, apparently, the chromosome was firmly attached to one of the beads, while an invisible tether was pulled out from the other side of the chromosome (Figure 6.1b). Visualization of one of those tethers using the intercalator YOYO-1 resulted in an inhomogeneous staining pattern, confirming that the tether consists of DNA and suggesting that the intercalator is unable to bind some regions of the tether possibly due the presence of DNA-binding proteins as described in Chapter 4 (Figure 6.1bc)[2].

Fluorescence imaging of a tether over time reveals stepwise disappearance of the tethers (Figure 6.1c), consistent with the presence of only a few DNA strands. Moreover, tracing the length between differently stained patches of the intercalator binding to the tether, reveals that the part of the tether closest to the chromosome mass is extended by a factor of 1.64, while two other regions of the tether are barely extended (a fraction of 1.09 and 0.97). This indicates that the additional tether length is originating from unraveling of the chromosome (Figure 6.1d).

The occurrence of DNA tethers coincided with rapid elongation of the chromosome as apparent from steps in the force-extension curve. To investigate the nature of the unraveling in more detail, a step-finding algorithm was used to analyze the force-extension data. The step-sizes had a peak at distances of 25 nm and a long tail to distances as high as 400 nm (Figure 6.1e). When looking at the steps more closely, it appears that some larger steps (400-800 nm) are split up into smaller steps (Figure 6.1f). A step-size of 25 nm agrees with the elongation caused by nucleosome unwrapping[3]. The larger steps (>100 nm) suggest that internal structures or cross links get broken. It is tempting to speculate that these larger steps could be related to the rupture of chromatin loops. Such loops have been predicted to be around 70-80 kbp[1,4], which would correspond with a nucleosome-bound DNA fiber of around 2-4 μm[5], almost an order of magnitude larger than what we observed. However, the loops might be cross-linked to or catenated with other loops, resulting in smaller observation of step-sizes. The visualization and localization of certain proteins on the tethers, such as condensins and nucleosomes, together with data of tether formation on condensin depleted chromosomes would provide more insight into the nature of chromosome unraveling.

Another observation from the chromosome unraveling stems from bright-field and fluorescence snap-shots of a few tether-pulling experiments, which revealed that some tethers originate from only one of the chromosome's arms. Interestingly, when these chromosome-tether structures were stretched, it became apparent that the parallel chromosome arm of the other chromatid was stretched to a similar extent as the arm from which the tether originated (Figure 6.1g) and experienced a similar force as can be concluded from the increase in force-sensitive intercalator binding (Figure 6.1h). This might indicate that the chromatids are still connected to each other and

6

Figure 6.1: Mechanical unraveling of chromosome ends. a) Formation of tethers is characterized by irregular force extension curves and longer extensions compared with chromosome stretching (black dotted line). b) BF image shows a chromosome mass attached to one of the beads and an invisible connection to the other bead. c) Fluorescent imaging in presence of 100pM YOYO-1 enables visualization of a tether and shows a disperse staining along its length. d) A kymograph, showing intercalator intensity along the chromosome and tether in time. Tracing of intercalator staining during stretching reveals inhomogeneous elongation of the tether in which the region closest to the chromosome mass is extended the most (relative increase of 0.64). Arrows depict two events where sudden intensity drops are observed, likely representing ruptures of DNA strands in the tether. e) Histogram of step-sizes from force-extension curves. f) Selection from a part of a force-extension curve with the result of the step-finding procedure. Bigger steps (red lines) are often split-up into smaller steps (dashed red lines). g) A tether that originate from one of the chromatids reveal that the unattached sister chromatid is stretched along with the attached chromatid. h) Fluorescence imaging of force sensitive YOPRO binding to a chromosome with a tether at increasing forces. An increase in fluorescence of YOPRO over the entire chromosome is observed, suggesting a distribution of force in lateral direction.

that the applied force is distributed in a lateral direction. Such connections could be governed by DNA linkages or by linker proteins, such as topoisomerases or cohesin. Yet, cohesin complexes are thought to be absent from chromatid arms at this stage in mitosis [6]. Although it is too early to draw any conclusions from these few observations, they warrant further investigation by for example attachment of the chromatid arms to different microspheres with the use of a quadruple-trap optical tweezers system or by the addition of topoisomerase to resolve potential DNA catenations.

The investigation of such tethers would greatly benefit from a controlled strategy to provoke the formation of tethers and probe the mechanical unraveling of chromosomes. We believe that these tethers arise because there is a limited number of biotin-streptavidin linkages connecting the chromosome to the bead. This idea is based on two observation: first, upon addition of the proteinase trypsin, chromosomes often entirely detach from the beads and show a high occurrence of tethers. This indicates the degradation of biotin and streptavidin itself results in chromosome unraveling; second, isolated chromosomes that were not purified from cell debris using glycerol gradient purification, showed much higher tether occurrence. This might be a result of partial shielding of the streptavidin-coated microspheres by cell debris. Therefore, in order to induce tether formation, we can, in the future, test two types of approaches to reduce the number of biotin-streptavidin bonds: i) reducing the biotinylation level on the chromosome itself, or ii) reducing the streptavidin-biotin bond formation during the chromosome attachment. Of these approaches, the latter is more efficient and easier to control. However, it is still feasible to have, for example, a lower biotin concentration in the cell culture, in order to achieve lower biotinylation levels of the telomeres. On the other hand, several approaches to reduce the biotin-streptavidin binding efficiency can be envisioned. For example, by introducing free streptavidin, biotin or other passivation agents in solution the number of binding sites on either the microspheres or the chromosomes themselves can be reduced.

To summarize, these experiments have already led to interesting results and promise to reveal valuable insights into the arrangement of the DNA inside the chromosome. Research on the mechanical unraveling of chromosomes could reveal the local conformation of chromatin packaging by analysis of step-sizes in the force-extension data. At the same time, investi-

gation of the staining pattern of certain proteins, like Condensin I and II and Topoisomerase IIα, by fluorescence imaging complemented with unraveling of chromosomes that lack one of those proteins can aid our understanding of the role of these proteins. With a few methodological improvements it should be possible to access this information more readily and with a high reproducibility, which will enable the systematic visualization and force-prob-ing of chromosome unraveling.

6.2   STED imaging of optically trapped chromosomes

Imaging chromosomes upon application of stress can provide a powerful tool to investigate mitotic chromosome structure. For example, in Chapter 5, this combination has revealed the heterogeneous structure and force response of the mitotic chromosome along its length. In the example above, this combination is used to argue that upon tether pulling chromosomes get unraveled from the chromosome mass. However, fluorescence imaging of the chromosome is hindered by the density of the structure and the small dimensions of the chromosome. With conventional microscopy techniques, features that are closer together than the diffraction limit, which is in the order of 200-300 nm for the visible spectrum, cannot be discerned[7]. With super-resolution approaches like stimulated emission depletion (STED) mi-croscopy, this limit can be overcome to resolve features that are much closer together. Therefore, we are developing a method to combine an optical tweezers setup with three-dimensional (3D)STED.

The general idea of STED is to apply, after brief confocal excitation with a diffraction limited spot, a partially overlapping stimulated emission depletion beam, such that the fluorophores in the overlap zone are effi-ciently brought back to their ground state, resulting in an effectively much smaller area with excited fluorophores (Figure 6.2a). In three dimensions, the depletion beam should therefore have the shape of a hollow sphere. Due to several sources of optical aberrations from either the setup itself or emerging due to the inhomogeneity of the refractive index of the sample, the shape of the STED beam needs adaption to the specific experimental circumstances. These adaptations are implemented with the use of adaptive optics (AO) that optimizes the quality of the STED point spread function, by detecting and then compensating the optical aberrations. We first tested the performance of the AO optimization by imaging nano-gold-beads (50 nm
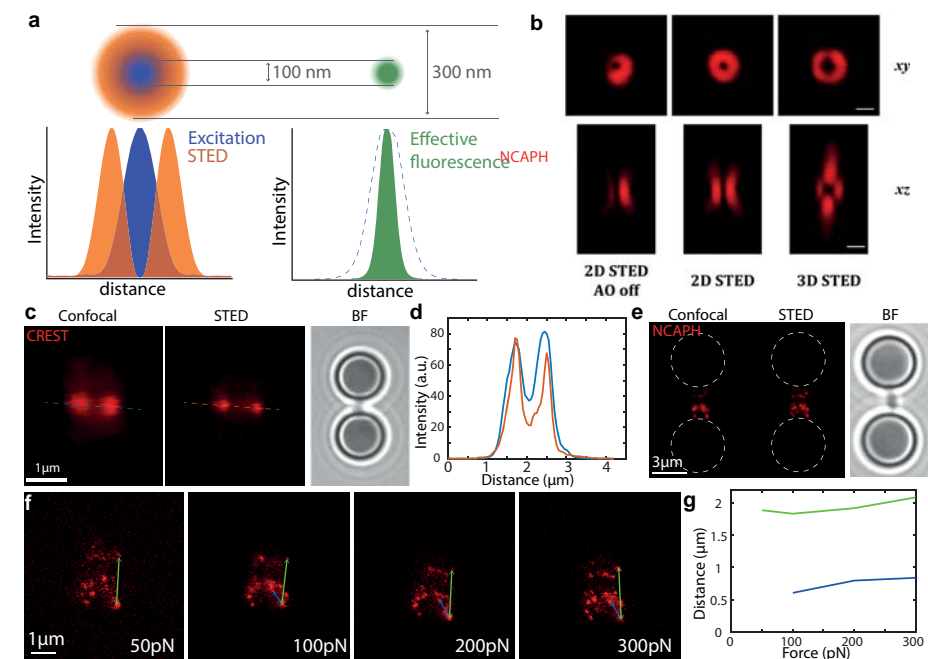
Figure 6.2: STED imaging of optically manipulated chromosomes. a) STED imaging relies on the depletion of excited fluorophores in an area around the ex-citation beam, thereby decreasing the effective area of fluorescence. b) Acous-to-optic modulation of the PSF for 2D and 3D STED shows a clear improvement in the shape of the STED beam. c) Imaging of a CREST labeled chromosome with confocal microscopy and STED. A comparison of an intensity profile along the blue and red dotted lines is provided in (d) and shows a reduced width of the centromere fluorescence upon STED imaging. e) Comparison of Confocal and STED imaging on a NCAPH (Condensin I) labeled chromosome. f) Imaging of NCAPH labeled chromosome during stretching. Blue and green arrows depict the distance between two pair of foci which increases as a function of force (g).

diameter) that are embedded in agarose gel. Indeed, a clear improvement in the quality of the STED point spread functions could be observed after the AO optimization (Figure 6.2b).

To show the functionality of the 3D STED technique on chromosomes, we imaged CREST-stained chromosomes with the immuno-staining protocol as described in Chapter 5. Two centromeres could clearly be discriminated using conventional confocal imaging, and upon imaging with 3D STED, the spot size of the centromeres was reduced from $FWHM_{conf} \approx 500$ nm to $FWHM_{STED} \approx 300$ nm (Figure 6.2cd). Moreover, thanks to the possibility to per-

form 3D imaging, we were able to determine that the two centromeres did not lie in the same focal plane.

Next, we tested whether the 3D STED imaging would yield higher resolution than confocal imaging on proteins that are abundantly present along the chromosome. We used immuno-staining of NCAPH which is a subunit of Condensin I, as described in Chapter 5. The confocal image shows a relatively vague image with some higher intensity spots along the chromosomes. However, the 3D STED image shows an irregular pattern of Condensin I spots on a virtually dark background (Figure 6.2e), which is in good agreement with previous observations [8,9]. By imaging Condensin I while stretching the chromosome, we can potentially obtain insight into the relative extension of different chromosome regions. Therefore, we performed 3D STED imaging at four different extensions and resulting forces (Figure 6.2f) and determined the distance between two pairs of foci at these forces (Figure 6.2g). As expected, the distance between these foci increased with force. We are currently working on an analysis to establish a three-dimensional reconstruction of the foci, in order to determine how different parts of the chromosome move with respect to one another as a function of force.

Taken together, this novel method promises to provide information on the relative motion of different chromosome components as a function of force. This type of data can contribute to the picture of chromosome mechanics and would be extremely valuable to validate a model that predicts the successive stiffening of different chromosomal elements.

6.3   Chromatid segregation

The process of chromosome segregation consists of an intricate series of complex steps, the exact timing of which is essential for faithful completion of mitosis. The first important realization is the formation of the compact mitotic chromosome structure. In the next phases of mitosis, the sister chromatids get attached via their kinetochores to the mitotic spindle that pulls on them from opposite poles of the cell, and after fulfillment of the spindle assembly checkpoint (SAC) the chromatids get segregated. An approach to actively induce the segregation of sister chromatids by the application of force and under controlled experimental conditions would open up a wealth of opportunities to study the processes that govern chromatid segregation. To this end, new tools for the micromanipulation of mitotic chromosomes

will be required. Some important steps to achieve this have already been made and will be presented here.

In order to segregate the sister chromatids with the use of optical tweezers, we need i) specific biotin handles on the kinetochores of the chromosome to bind them to streptavidin-coated microspheres, and ii) a strategy to induce the cleavage of cohesin. First, using a similar method as described in Chapter 5, we developed a cell line with ectopically expressing CENPB-BirA HT1080 cells. Fluorescence imaging of chromosome spreads incubated with AlexaFluor 568 streptavidin confirmed that chromosomes showed biotinylation of the centromeric region (Figure 6.3a).

In order to induce cleavage of cohesin we tested several strategies. One possibility is to purify the protein Separase, which naturally cleaves cohesin after fulfilment of SAC (Figure 6.3b). The challenge is that this protein is tightly regulated by several pathways in order to prevent premature cleavage. Most importantly, the active site of Separase is bound by the protein Securin. Only after passing SAC, Securin quickly gets degraded, thereby revealing the active site of Separase. Securin also acts as a chaperone for Separase and it is therefore extremely challenging to purify Separase without Securin bound to it. We applied a strategy that was described by Stemman et al. [10], where Xenopus frog egg extract is used to degrade Separase-bound Securin. However, this might not be sufficient to induce cleavage of cohesin, since Separase is also inhibited by two Securin-independent processes: Separase phosphorylation and SGO2-Mad2 binding [10,11]. As an alternative to the physiological cleavage of cohesin by Separase, we tested a cell line that ectopically expresses a mutated version of cohesin with an HRV cleavage site on one of its subunits, RAD21/SCC1 (Figure 6.3b) and shRNA against endogenous RAD21/SCC1 [12]. Although, cleavage with HRV protease is generally a very efficient process, it should be noted that due to the presence of wild-type cohesin, chromatid segregation might still be hindered.

Next, we set out to attach the centromeric-biotinylated chromosomes to the microspheres using the workflow as described in Chapter 5. The efficiency of attachment was noticeably lower than with telomeric-biotinylated chromosomes. Generally, attachment failed either during the step of chromosome flow stretching, which we attribute to the lowered viscous drag force that a centromeric-attached chromosome experiences, or during the attachment of the second bead, which turned out to be relatively inefficient.

6
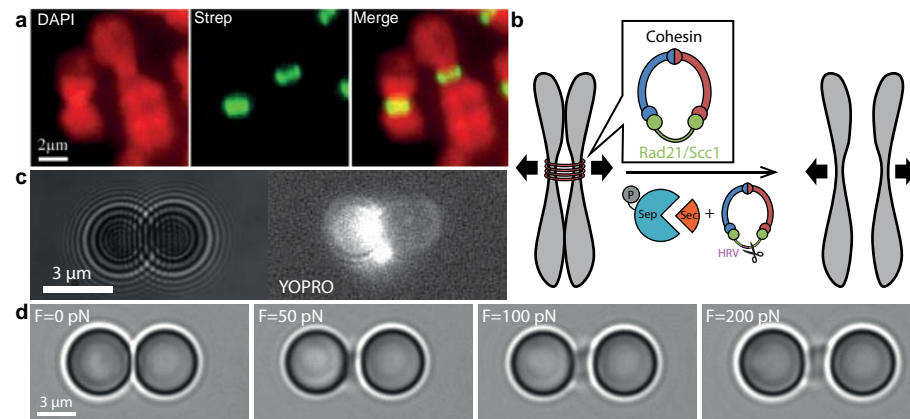
Figure 6.3: Micromanipulation of mitotic chromosomes via their centromeres.
a) Sister chromatids are prevented from segregation by cohesin proteins which are primarily located at the centromeric region. Chromosomes will be exposed to i) purified Separase of which Securin will be degraded prior to the experiment, and ii) HRV protease that can cut the Rad21/Scc1 subunit of the cohesin proteins that contain an HRV cleavage site. Subsequently, a mechanical load will be applied along the centromeres to observe whether chromatid segregation can been induced. b) Chromosome spreads stained with DAPI and Streptavidin conjugated with Alexa Fluor 568 show that the centromeric region of chromosomes are biotinylated. c) A mitotic chromosome attached via its centromeres to two microspheres. Due to the close proximity of the microspheres, the chromsome is hard to discern with BF imaging, but shows a clear signal upon fluorescence imaging with 100nM YOPRO. d) After exposure to Separase and HRV protease, a chromosome was subjected to forces up to 200 pN. Although a small extension of the structure could be achieved, segregation of chromatids was not observed.

However, in about 10% of the attempts we managed to attach a chromosome in between two microspheres and could visualize it with fluorescence microscopy using the DNA binding intercalator YOPRO (Figure 6.3c). These results show that we can optically manipulate centromeric-attached mitotic chromosomes.

Motivated by the successful optical manipulation of centromeric biotinylated chromosomes, we attempted to induce chromosome segregation. First, we noticed that application of forces up to 300 pN did not induce any observed separation of the microspheres. Next, we moved the chromosome to a side channel containing a mixture of purified Separase and HRV protease. However, we did not observe any visual separation of the chromatids,

nor did we see an additional change in the bead-to-bead distance even after prolonged applications of forces around 200 pN.

In order to induce chromatid segregation, there are several aspects of this experiment that we are currently addressing. First of all, we want to improve the efficiency of chromosome attachment to the microspheres. The CENPB-BirA fusion protein is located quite far inside the chromosome in a region referred to as the inner-kinetochore. This potentially poses several problems: i) the proteins that become biotinylated might be difficult to reach by a microsphere outside of the chromosome, ii) a microsphere might get attached to proteins from both chromatids simultaneously, since the biotinylated areas are really close together, and iii) ideally an attachment point is chosen that is closer to the natural attachment site of microtubules, which is on the outer kinetochore. Therefore, we are currently looking at several candidate proteins, located on the outer-kinetochore, that can be fused to BirA. Moreover, we consider the use of smaller microspheres to reduce the chance of simultaneous attachment to the two chromatids. And finally, we are thinking about a system where we can use an additional linker, such as much smaller beads, which we can use to pre-incubate the chromosomes. Together, we hope that these strategies will improve chromosome attachment to microspheres.

On the other hand, we are trying to realize alternatives to the current strategy of cohesin cleavage. We foresee three issues with the current approaches: i) Separase purification is very time-consuming and yields low concentrations and volumes of the protein. This might lead to very inefficient cleavage of cohesin; ii) cohesin might be prevented to be cleaved by Separase by other inhibitory mechanisms; iii) upon HRV-cleavage of cohesin, a background of non-cleaved wild-type cohesins will persist that might be enough to keep the sister chromatids together. Therefore, we are now trying to develop cell lines endogenously expressing cleavable cohesin. The generation of such a cell line would yield an efficient method to cleave all cohesin present on the chromosome and form an important step towards the in vitro segregation of chromosomes.

Upon attachment of microspheres to opposite kinetochores and efficient cleavage of cohesin, we foresee a variety of interesting research opportunities. First of all, we are extremely curious about what sort of structure the chromatid segregation would give rise to. How many DNA

entanglements can be observed? Can we observe ultrafine anaphase DNA bridges that are shown to connect sister chromatids after segregation [13] and can we relate their position on the chromosome for example to the location of fragile sites? Can these ultrafine anaphase DNA bridges be resolved by the addition of certain topoisomerases and helicases? On the other hand, this scheme also provides a means to study the set of proteins that are responsible for the mechanical load transfer from the microtubules to the chromosome. It would be interesting to estimate the forces that these proteins have to bear and whether they behave as "catch bonds" that strengthen upon tension as is proposed by some researchers in the field [14]. We foresee that the approach described here to micromanipulate centromeric-attached chromosomes and induce cohesin cleavage allowing for a combination of genetic, chemical and physical perturbations will provide a powerful tool to address questions regarding chromatid segregation.

6.4   Future perspectives

This thesis presents our efforts towards investigations of the mitotic chromosome including the mechanical characterization of normal chromosomes, the development of a model to describe chromosome mechanics and the role of a specific protein, Topoisomerase IIα, for the chromosomal architecture. In this Chapter, I have described a few recent developments that push the border of what is possible with our newly developed technique even further. Here, I would like to describe some of the outstanding questions in the field, that we now wish to address with the technique of chromosome micromanipulation.

Up till now, the mitotic chromosome architecture remains a topic of heavy investigations [5,15,16]. One of the challenges to study the mitotic structure is its small and densely crowded nature that hinders imaging with light microscopy. The methodology described in this thesis can provide an entirely novel approach to study this complex structure. By the expansion of the chromosome due to application of force or salt induced swelling (as described in Chapter 5) visualization of the structure can be facilitated. Especially the combination with super-resolution imaging approaches as described in Chapter 5 and in subheading 6.2 of this Chapter with dynamic

micromanipulation and chemical perturbations, is likely to unveil unprecedented details of the chromosome structure.

With such an approach we aim to investigate some outstanding questions in the field. For example, we would like to relate the model of successively stiffening elements that we propose in Chapter 5 to describe chromosome mechanics, to the model that describes the formation of mitotic chromosome structure by the extrusion of radially protruding loops from a central scaffold, as is currently accepted in the field [1,4,17,18]. It would be of great value to scrutinize what elements are mechanically load bearing and cross-link the chromatin fiber: are these the same proteins, Condensin I and II and Topoisomeras IIα, that play crucial roles for the formation and maintenance of the mitotic chromosome structure; is the chromosome's resistance to stress governed by abundant interactions between nucleosomes; or are there even other underlying principles yet undiscovered? These questions can be addressed by depletion or chemical perturbation of such proteins. On the other hand, one can also envision an experimental workflow that rescues such a perturbed system by the external reintroduction of these elements with the use of microfluidics.

In relation to this, we would like to examine what elements in the chromosome give rise to the proposed model of successive stiffening as described in Chapter 5. Do these elements form a serial arrangement along the chromosome's length? And if so, can we come to a detailed picture explaining what differences in molecular structure give rise to the observed distribution of mechanical properties? It would be of great interest to investigate the relationship of such serial arrangement to a distribution of proteins such as Condensin I and II and TOP2A, or to the G-banding patterns that are commonly used to characterize chromosomes and were previously related to variations in the stiffness [19]. Also fragile sites, which are thought to be correlated with uncondensed chromatin regions and relatively frequently give rise to DNA damage during cell division, might be related to a relatively soft local structure [20]. Localization of (G-)bands or heterogeneously distributed proteins, can be used to explore the local extension of different regions of the chromosome in relation to the total extension of the chromosome as induced by force application. This would provide valuable insight into the existence of chromosome segments with a distribution of mechanical properties. In combination with the induction of active fragile sites by different

6

fragility-causing conditions, this could at the same time aid the research on chromosome fragility. On the other hand, if it is rather a hierarchy of structures across different length scales that gives rise to the observed successive stiffening, then it would be interesting to find out what molecules and interactions are responsible for the formation of such structural levels, and whether we can unveil a relation between such hierarchical levels and the central scaffold with surrounding chromatin. Experiments regarding the mechanical unraveling of the chromosome (see subheading 6.1) can aid the investigation of the central scaffold and existence of chromatin loops.

Finally, I foresee that this methodology can be advanced even further in order to narrow down the observed variation among chromosomes. I envision that this could be achieved by two means. First, the observed variation is probably a result of the intrinsic variation among chromosomes. The possibility to micromanipulate specific chromosomes would improve the specificity and resolution of the experiments and thereby help to reveal even more details. Another origin of experimental variation might be the spread in timing of cells upon entrance of mitosis and thereby the prolonged exposure to compaction by proteins such as condensin[9] as well as the range in time between isolation and micromanipulation. Therefore, another technical advance to the described methodology, would be the direct isolation and manipulation of chromosomes inside the microfluidic flow cell. Next to improving specificity and resolution, these improvements would be highly advantageous for other reasons as well. For example, the in situ isolation of chromosomes would eliminate the need to stall the cell cycle with drugs such as nocodazole that might affect chromosome structure. At the same time, very small samples of cells would be required, which would in the long-term even enable to study samples of patients with chromosome abnormalities in a clinical setting. In situ chromosome isolation would also ensure protein preservation and prevent morphological changes that possibly happen after isolation. Finally, the ability to micromanipulate specific chromosomes would enable the comparison of mechanics between different specific chromosomes that for example differ in length, banding pattern and presence of fragile sites. These two advances on the established methodology will likely bring the chromosome manipulation to yet another level of control and precision.

The outstanding questions, the proposed research and the technical advances described in this Chapter, might make a daunting impression. It is without doubt that along the way, other unforeseen challenges will present themselves that have to be overcome. And with every step, new scientific questions will emerge that need to be solved. Nevertheless, during the research often accidental opportunities arise as well and may lead to entirely unpredicted research directions and insights. At the same time, progress may go faster than expected. Five years ago, I could not imagine that we would be able to optically manipulate chromosomes with such a degree of control at this moment in time. Today, I am in the luxurious position of wishing my successors all the best with the continuation of the exciting research on mitotic chromosomes with a currently operational method.

References

1. Gibcus, J. H. et al. A pathway for mitotic chromosome formation. Science (80-.). 359, (2018).
2. Meijering, A. E. C. et al. Imaging unlabeled proteins on DNA with super-resolution. Nucleic Acids Res. 48, e34 (2020).
3. Spakman, D., King, G. A., Peterman, E. J. G. & Wuite, G. J. L. Constructing arrays of nucleosome positioning sequences using Gibson Assembly for single-molecule studies. Sci. Rep. 10, 1–11 (2020).
4. Walther, N. et al. A quantitative map of human Condensins provides new insights into mitotic chromosome architecture. J. Cell Biol. 217, 2309–2328 (2018).
5. Batty, P. & Gerlich, D. W. Mitotic Chromosome Mechanics: How Cells Segregate Their Genome. Trends Cell Biol. 29, 717–726 (2019).
6. Waizenegger, I. C., Hauf, S., Meinke, A. & Peters, J. M. Two distinct pathways remove mammalian cohesin from chromosome arms in prophase and from centromeres in anaphase. Cell 103, 399–410 (2000).
7. Helmholtz, H. On the limits of optical capacity of the microscope. Mon. Microsc. J. 16, 15–39 (1876).
8. Ono, T. et al. Differential contributions of condensin I and condensin II to mitotic chromosome architecture in vertebrate cells. Cell 115, 109–121 (2003).
9. Sun, M., Biggs, R., Hornick, J. & Marko, J. F. Condensin controls mitotic chromosome stiffness and stability without forming a structurally contiguous scaffold. Chromosom. Res. 26, 277–295 (2018).
10. Stemmann, O., Zou, H., Gerber, S. A., Gygi, S. P. & Kirschner, M. W. Dual Inhibition of Sister Chromatid Separation at Metaphase the anaphase promoting complex (APC) (for review, see King et al., 1996a). This proteolysis pathway is under the control of the mitotic spindle checkpoint, which ties. Cell 107, 715–726 (2001).
11. Hellmuth, S., Gómez-H, L., Pendás, A. M. & Stemmann, O. Securin-independent regulation of separase by checkpoint-induced shugoshin–MAD2. Nature 580, 536–541 (2020).
12. Zuin, J. et al. Cohesin and CTCF differentially affect chromatin architecture and gene expression in human cells. Proc. Natl. Acad. Sci. U. S. A. 111, 996–1001 (2014).
13. Liu, Y., Nielsen, C. F., Yao, Q. & Hickson, I. D. The origins and processing of ultra fine anaphase DNA bridges. Curr. Opin. Genet. Dev. 26, 1–5 (2014).
14. Sarangapani, K. K. & Asbury, C. L. Catch and release: How do kinetochores hook the right microtubules during mitosis? Trends Genet. 30, 150–159 (2014).

15.   Piskadlo, E. & Oliveira, R. A. A topology-centric view on mitotic chromosome architecture. Int. J. Mol. Sci. 18, 1–21 (2017).

16.   Belmont, A. S. Mitotic chromosome scaffold structure: New approaches to an old controversy. Proc. Natl. Acad. Sci. U. S. A. 99, 15855–15857 (2002).

17.   Paulson, J. R. & Laemmli, U. K. The structure of histone-depleted metaphase chromosomes. Cell 12, 817–828 (1977).

18.   Maeshima, K. & Laemmli, U. K. A Two-step scaffolding model for mitotic chromosome assembly. Dev. Cell 4, 467–480 (2003).

19.   Hliscs, R., Mühlig, P. & Claussen, U. The nature of G-bands analyzed by chromosome stretching. Cytogenetic and Genome Research vol. 79 162–166 (1997).

20.   Schwartz, M., Zlotorynski, E. & Kerem, B. The molecular basis of common and rare fragile sites. Cancer Lett. 232, 13–26 (2006).

Appendices

Summary
Dankwoord
Publication list
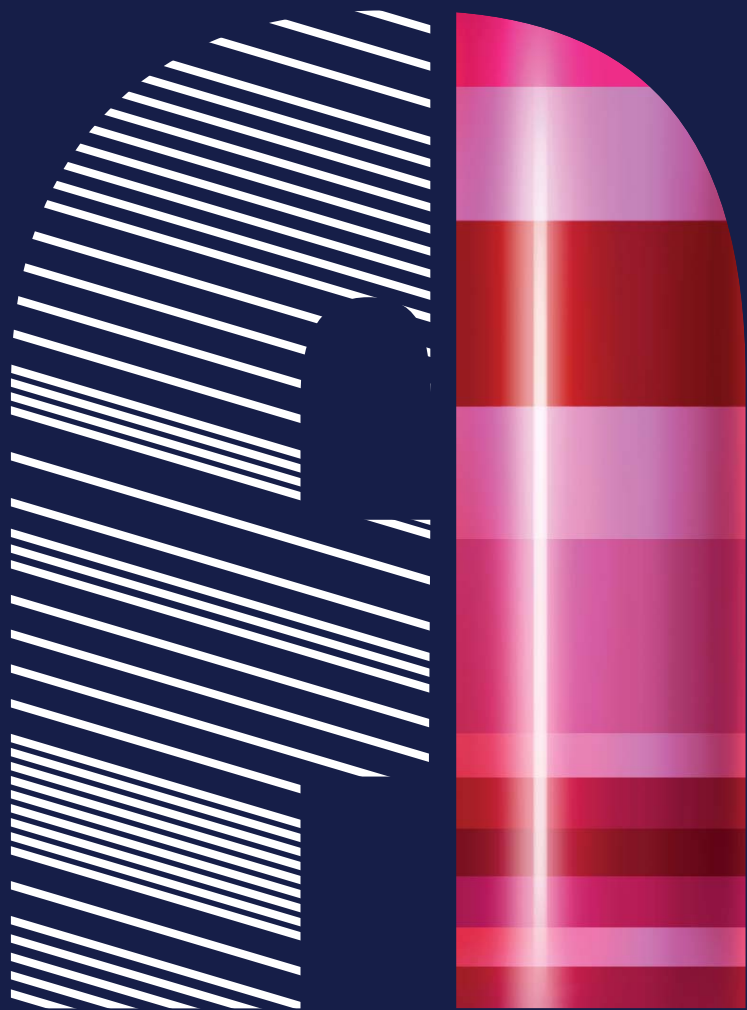
Summary

The genome of the human body is subdivided into 46 chromosomes, the smallest of which contains a total DNA length of 16 mm. During cell division, the chromosome adopts a compacted X-shaped structure with a length of only a few micrometers. As such, the DNA gets compacted around four orders of magnitude in length. How this extremely robust structure is achieved has been a topic of debate for a few decades. Several proteins have been shown to have key functions in the formation and maintenance of this structure (see **Chapter 1**). However, due to the relatively small and dense structure of the chromosome and the limited control over the conditions that experimentalists have when dealing with living cells, it is very challenging to study the chromosomal architecture. Therefore, we set out to develop a novel methodology with the aim to study the complex structure of mitotic chromosomes in an environment where we have full control over experimental conditions.

To this end, we decided to use the technique of optical tweezers, where highly focused laser beams can be used to grab micron-sized objects and apply forces to them (see **Chapter 1** and **Chapter 2** for an explanation of this technique and a review of current advances in the field of single-molecule studies with optical tweezers). In our lab, this technique is frequently employed to study DNA molecules, by tethering them in between two micron-sized spheres that can be trapped with the optical tweezers. Before, this technique has been used to obtain a detailed picture of the mechanics of bare DNA. Our aim was to use optical tweezers in a similar fashion to learn about the structure of chromosomes. Before arriving to that point, I set out to develop two tools that would aid the research on chromosomes.

First, we implemented a technique on the optical tweezers setup to visualize proteins (**Chapter 3**). Generally, individual proteins are not visible with a normal, transmitted-light, light microscope. However, when they are labeled with so-called fluorophores, they can be visualized by shining light of a specific wavelength. The fluorophores will absorb this light and emit light of a slightly longer wavelength that can then be collected and imaged onto a camera (see **Chapter 1** for an explanation of fluorescence). Ideally, one wants to be able to visualize several types of proteins at the same time. Therefore, we implemented a wide-field fluorescence module with the possi-

A

bility to excite with three different wavelengths at the same time. In order to detect the light of three different fluorophores, we designed a fluorescence detection module that splits the emission light based on wavelength and projects it onto different areas of a camera chip. Finally, we added an extra feature to the detection path that enables three-dimensional imaging, which is necessary for the imaging of chromosomes , which have a thickness of around 2 µm.

It is not always possible to label proteins with fluorophores. In a chromosome there are simply too many different proteins around to label them all of them with a fluorescent dye. Moreover, fluorophores sometimes interfere with the function of the protein and fluorescent labeling can be time-consuming. Therefore, in **Chapter 4**, a new technique is presented that can be used to visualize proteins without the need to fluorescently label them. This method is based on the mechanism that protein-bound regions of the DNA cannot be bound by other fluorescent dyes. As such, a fluorescent DNA-binding probe could be used to map out the regions of bare DNA and thereby reveal which regions of the DNA are occupied by proteins. We used this technique to visualize a protein complex (XLF) which diffused along the DNA. In the other limit, we showed that we can localize individual binding events of intercalators and thereby obtain a super-resolved image of the DNA that showed gaps where patches of the protein RAD51 are bound to the DNA. This technique might provide a powerful tool to visualize proteins on chromosomes without the need of labeling them.

In **Chapter 5** a method is presented that allows for the optical manipulation of mitotic chromosomes. We have developed human cell lines that incorporated a specific linker (biotin) at the end of the chromosome arms (telomeres, see **Chapter 1**). After isolating the chromosomes from mitotic cells, we could attach the telomeres via strong biotin-streptavidin interactions to our streptavidin-coated microspheres. This enabled us to perform experiments where we probed the mechanical response of the chromosome to applied extensions. From these experiments we learned that the chromosome is relatively soft for small extensions, but shows a dramatic increase in the force at higher extensions. The observed behavior is not consistent with any classical model that describes polymer (network) mechanics. Therefore, we proposed a new model to describe the chromosomes mechanical behavior. This model describes the chromosome as consisting of many elements

or modes that successively stiffen. Moreover, we were able to investigate the role of a specific protein, TopoisomeraseIIα (TOP2A), in the chromosome structure. We found that upon depletion of TOP2A the chromosome shows a softer stiffening behavior. Interestingly, when we perturbed the structure of the chromosome by swelling it with high salt concentrations and then let it come back to its original shape, the control chromosomes did not show significant changes in their stiffness, but the TOP2A degraded chromosomes did. This indicated that TOP2A plays a structural role in the chromosome architecture. Together, these results highlighted the capability of our novel method to determine mechanical properties of chromosomes under highly controlled conditions.

In **Chapter 6** of this thesis, preliminary data of some unfinished projects are presented in addition to future perspectives on the research of mitotic chromosomes with the novel approach presented in Chapter 5.

A

Dankwoord

Toen ik vijf jaar geleden op zoek was naar een positie voor mijn promotie onderzoek en met Gijs Wuite en Erwin Peterman sprak, vertelden zij me enthousiast over een nieuwe methode die ze wilden ontwikkelen waarbij ze aan chromosomen wilden gaan trekken met een optisch pincet. Het zou lastig worden, "high risk, high gain". Als ik het aan het werk zou krijgen, dan ging er een wereld voor ons open. Enthousiasmeren, dat kan je wel aan Gijs overlaten. Maar toen ik thuis kwam rees bij mij de vraag wat ik dan precies zou gaan onderzoeken. In een vervolg gesprek kwam het antwoord: "Ontzettend veel! Onontgonnen terrein!"

Dat was de eerste les van mijn promotie onderzoek. Als je iets nieuws doet, moet je er soms gewoon vertrouwen in hebben dat er iets interessants uit zal komen. Wetenschappelijk onderzoek wordt er bij uitstek door gekenmerkt onvoorspelbaar te zijn. Mijn PhD heeft in het teken gestaan van het ontwikkelen van de in deze thesis beschreven methode. Wat ik van tevoren niet had voorzien, was dat ik mezelf bekend moest maken met het kweken van cellen, het bouwen van optische opstellingen, het installeren van computers, het uitvoeren van complexe experimenten en het ontwikkelen van modellen. De weg was niet recht, sommige doorbraken berustten op toeval, enkele hindernissen leken onoverkomelijk en zonder de hulp van een groot aantal mensen was het nooit gelukt.

Gijs, ik wil je bedanken voor de begeleiding die je me hebt gegeven. Het was een genot dat je me vrij liet te doen wat ik goed achtte. Regelmatig hebben je positieve woorden over in mijn beleving, futiele vooruitgang me weer een duwtje in de rug gegeven. Het gevoel van jouw vertrouwen in mijn kunnen, was soms net wat ik nodig had om ook zelf te geloven dat ik iets voor elkaar kon krijgen.

Erwin, jij bent van alle markten thuis. Moet ik je inhoudelijke kennis van zo ongeveer alles roemen – optica theorie en onderdelen, de naam en het jaartal van dat ene artikel waar ik naar op zoek ben, de geschiedenis vanaf Luther tot onze universiteiten nu en hoe je het beste asperges kan bereiden? Zal ik je bedanken voor het feit dat jouw deur altijd letterlijk en figuurlijk open stond? Of zal ik warme herinneringen ophalen aan hilarische koffie- en lunchpauzes, overheerlijke kreeft en champagne in Monterey, enthousiaste berichten over de staartmeesjes in "onze" boom en een aanzienlijke hoe-

A

veelheid biertjes tijdens borrels, verdedigingen en conferenties? Ik kan niet kiezen. Bedankt voor dit alles!

Iddo, wat heb ik veel gehad aan al jouw hulp! Al met al heb je vele uurtjes geholpen met het bouwen van de JAN-trap, heb je me begeleid met het schrijven van mijn eerste artikel en kon ik altijd bij je aankloppen met vragen. Ook heb ik ontzettend veel geleerd van je scherpe vragen en kritische blik op data tijdens onze group- en OT meetings. En hebben we veel kunnen lachen tijdens lunches en koffiepauzes. Ik weet zeker dat je een fantastische professor wordt!

Without the fantastic collaboration with the people from the Centre for Chromosome Stability in Copenhagen, this project would never have worked out. **Kata,** although we were at quite a big distance most of the time, there are few people with whom I've talked so regularly throughout my PhD. In this project every single tiny step seemed to be like a canyon that had to be passed. Nothing just worked from the start. It is a miracle that we didn't give up and that we kept confidence that it would work. I admire your perseverance and directness. Thanks for this shared adventure! **Anna,** your enthusiasm about this project and science in general, has strongly inspired me. You were the one that showed me living and dividing cells for the first time. Something I will never forget. **Christian,** it was great to work with you during the later phase of the Chromavision project. You are definitely a cell magician. I keep my fingers crossed for the centromeric pulling experiments; I know you can do it! **Ian** and **Ying,** it was a great pleasure to work with you. You always made me feel welcome in your lab. Thanks for this wonderful collaboration.

Chase, in de laatste fase van mijn PhD had ik het geluk dat jij onze afdeling kwam versterken. Dankzij jouw originele blik, kritische vragen en heldere analyses, hebben we ons onderzoek naar een hoger niveau kunnen tillen. Hartelijk dank daarvoor!

Dankzij de gastvrijheid van de mensen van de ACTA en specifiek de hulp van **Cor** kon ik zelf cellen kweken en chromosomen isoleren. De mannen van de technische werkplaats leveren elke dag essentiële onderdelen zonder welke ons onderzoek niet zou kunnen plaatsvinden. Ik ben oneindig veel dank verschuldigd aan **Pierre,** die bijna altijd onze "kwikjes" voorrang gaf en bovendien altijd in was voor een gezellig praatje. Ik wil ook de mensen van

Lumicks, en **Mattijs** en **Onno** in het bijzonder, bedanken voor hun hulp bij zowel technische als software problemen en het geven van advies!

Emma, dankzij jou was ik plotseling niet meer alleen in het lab aan chromosomen aan het trekken. Ik kijk met enorm veel plezier terug op onze samenwerking die gedurende de tijd zich steeds verder uitbreidde van chromosomen trekken, naar celculturen en het opzetten van een lab! Ik wens je heel veel succes met het vervolg van je carrière. **Hannes,** it has been a delight to finally have someone to share ideas with about the chromosome research. Due to corona, you are the colleague that I have seen the least and worked together with the closest! Thanks for the enumerable chats about data, experiments, research ideas and other random topics. **Janni,** although our collaboration has been very brief, it has been extremely fruitful as well! Thanks for joining our research. The new chromosome team, **Tianlong, Guus, Stijn** and **Tinka,** I have a lot of confidence that you will continue and expand the project with even more exciting research.

Longfu, Giulia, Agata, Vadim and **Dian,** it was great fun sharing an office. I wish you all the best continuing your PhD. Don't forget: "Let that shit go"! **Andreas,** I don't know how to thank you for the countless times that I bothered you with urgent questions. Your knowledge and intuition for science is remarkable. In fact, maybe you are what I will always bear in mind as the prototype of a true scientist. **Joost,** je vrolijke aanwezigheid, onophoudelijke toestroom van studentenhaver en ons eindeloze geouwehoer over wielrennen hebben wellicht het onderzoek niet bespoedigd, maar zeker wel aangenamer gemaakt! Ik ben onder de indruk van jouw kunde en kennis: onderschat jezelf niet. **Kiki,** ik bewonder je om je directheid en je betrokkenheid. Je staat altijd voor anderen klaar als ze hulp nodig hebben. Zo ook voor mij. Dank daarvoor. **Bram,** je hebt me menig keer uit de brand geholpen als ik weer eens IT problemen had. Dankjewel voor je behulpzaamheid!

Jaap, we begonnen bijna tegelijkertijd aan ons promotie onderzoek, beide een beetje eenzaam met een project waar niemand anders aan werkte. Op dit moment zijn onze projecten uitgegroeid tot succesvolle onderzoeksrichtingen bestaande uit een aanzienlijk team; mede ook dankzij ons werk. We mogen trots zijn op deze prestatie! The worm group, **Christine, Noemie, Liza, Ani, Wouter,** you guys make up a great team.

Denise, I don't think I have laughed so much with anyone else ever before, than I did with you. **Jona,** thanks for the fun chats and your sincere

A

interest in life at the VU, even long after you left the group! **Seyda,** you have been of great value for the chromosome project. I don't know whether we would have isolated a single clean chromosome batch without you! **Daan, Douwe, Raya, Jordi, Maryam, Graeme, Vandana, Ning, Mariska, Aravindan, Sandrine, James,** from the start that I joined the lab, I have always felt welcome. Thanks for creating such a nice atmosphere.

Ik wil mijn geliefde **Toppers** groepje bedanken voor de jaarlijkse traditie om een avond lang te dansen en zingen op de beste Nederlandse hits verkleed als badgast, flamingo of Aladin-figuur. Wat hebben wij een plezier gehad! Ook het **V&V-team** kan ik niet ongenoemd laten: dankzij onze gezellige avondjes kon ik regelmatig tijdens de koffiepauze zeer kundig overkomen over een aantal uiteenlopende onderwerpen. Laten we onze traditie voortzetten! **Margot & Dirk,** avondjes lekkere biertjes drinken en ons jaarlijkse weekend weg bieden altijd weer genoeg vreugde om er weer een poos tegenaan te gaan. Hoewel we het nu nog maar twee weken van tevoren mogen vragen, hebben Tim en ik al een datum voor ons volgende uitje staan!

Theresa, I am so grateful for our friendship that already lasts for quite some time even though we cannot see each other on a regular basis. Your kindness and positive attitude are an inspiration for me.

Ineke, toen ik overwoog mijn PhD bij Gijs en Erwin te doen, was jij degene die me uitnodigde een keer bij een borrel van het lab aan te sluiten. Inmiddels is een hechte vriendschap ontstaan. Ik bewonder je als wetenschapper, je wordt zeker weten een fantastische professor.

Megghi, bellisima, donna Marchetti! Thank you so much for all the fun and laughs that we shared. I admire your optimistic attitude, your ability to say serious things in a nice and direct way and your sense of humour. It is an honour that you want to stand here next to me on the stage.

Julia, wat hebben wij eigenlijk niet gedeeld tijdens onze PhD? We hebben gelachen (veel en hard als ik omstanders mag geloven), hoogtepunten gevierd (een fles wijn leegdrinken midden op de dag omdat de computer eindelijk werkt), om dieptepunten getreurd (de C-flop spant toch wel de kroon), we gingen samen op road-trip, we bouwden een fantastisch werkende opstelling, we werden beide zwanger (en kregen onze kindjes twee weken na elkaar!) en nu sta jij naast me op het podium. Dankjewel voor het delen van lief en leed.

Tot slot wil ik mijn familie en schoonfamilie bedanken voor alle steun die ik door de jaren heen van hen heb mogen ontvangen. Een aantal van hen ben ik in het bijzonder veel dank verschuldigd.

Mama, van jou heb ik van jongs af aan liefde en bewondering voor de biologie meegekregen, een passie die mij ertoe heeft aangezet aan dit onderzoek te beginnen. Het PhD traject was niet altijd makkelijk, maar ik wist dat ik altijd op jou kon rekenen in woord en daad. Dankjewel voor je eindeloze steun en liefde.

Papa, ik denk dat jij een van de weinige personen bent die mijn iBALM artikel daadwerkelijk heeft gelezen. Dit boekje kan je wellicht weer een aantal extra nachten van leesvoer voorzien. Ik bewonder je passie voor wetenschap. Dankjewel voor jouw niet aflatende interesse in mij en mijn onderzoek.

Ilse, mijn lieve kleintje. Wat ben jij een mooi en bijzonder mensje. Jij tovert zonder moeite een lach op mijn gezicht. Je hebt me nu al zo veel geleerd. Je verwondering en blijdschap om kleine dingen, de kracht die je in je hebt, je onconventionele aanpak: jij bent de echte onderzoeker. Ik kijk ernaar uit te zien hoe jij je eigen weg zal bewandelen in het leven.

Tim, je had me nog zo gewaarschuwd, 'begin er niet aan'. Hoewel ik je woorden in de wind sloeg, bleef je me onophoudelijk steunen ook als het promotie onderzoek even wat minder leuk was. Dankzij jouw gevoel voor humor en je nuchtere adviezen werden die momenten minder zwaar. Wat hebben we daarnaast veel gekke, leuke en bijzondere dingen meegemaakt! Met jou is het leven zoveel leuker. Ik hou van je.

A

Publication list

1. D. Chavan, J. Mo, M. de Groot, <u>A.E.C. Meijering</u>, J.F. de Boer and D. Iannuzzi. Collecting optical coherence elastography depth profiles with a micromachined cantilever probe. *Optics Letters* **38** (9), pp.1476-1478, **2013**. *(Not in this thesis)*

2. K. Gopfrich, T. Zettl, <u>A.E.C. Meijering</u>, S. Hernandez-Ainsa, S. Kosabev, T. Liedl and U.F. Keyser. DNA-Tile structures induce ionic currents through lipid membranes. *Nano Letters* **15** (5), pp.3134-3138, **2015**. *(Not in this thesis)*

3. S. Deshpande, Y. Caspi, <u>A.E.C. Meijering</u> and C. Dekker. Octanol-assisted liposome assembly on chip. *Nature Communications* **7**, art.nr.10447, **2016**. *(Not in this thesis)*

4. M. Hashemi Shabestari[*], <u>A.E.C. Meijering</u>[*], W.H. Roos, G.J.L. Wuite and E.J.G. Peterman. Recent advances in biological single-molecule applications of optical tweezers and fluorescence microscopy. *Methods in Enzymology* **582**, pp.85-119, **2017**. *(Chapter 2)*

5. <u>A.E.C. Meijering</u>, A.S. Biebricher, G. Sitters, I. Brouwer, E.J.G. Peterman, G.J.L. Wuite and I. Heller. Imaging unlabeled proteins on DNA with super-resolution. *Nucleic Acids Research* **48** (6), pp. e34, **2020**. *(Chapter 4)*

6. <u>A.E.C. Meijering</u>[*], J.A.M. Bakx[*], T. Man, I. Heller, G.J.L. Wuite and E.J.G. Peterman. Implementation of 3D multi-color fluorescence microscopy in a quadruple trap optical tweezers system. *Submitted (Chapter 3)*

7. <u>A.E.C. Meijering</u>, K. Sarlos, C.F. Nielsen, H. Witt, J. Harju, E. Kerklingh, G.H. Haasnoot, A.H. Bizard, I. Heller, Y. Liu, C.P. Broedersz, E.J.G. Peterman, I.D. Hickson and G.J.L. Wuite. Exposing chromosome mechanics and architecture using optical manipulation and fluorescence microscopy. *In preparation (Chapter 5)*

[*]These authors contributed equally

A